January 2022

# Correlations And Dynamic Fluctuations In High Energy Collisions

Zoulfekar Mazloum
*Wayne State University*

## Recommended Citation

Mazloum, Zoulfekar, "Correlations And Dynamic Fluctuations In High Energy Collisions" (2022). *Wayne State University Dissertations*. 3641.
https://digitalcommons.wayne.edu/oa_dissertations/3641

# CORRELATIONS AND DYNAMIC FLUCTUATIONS IN HIGH ENERGY COLLISIONS

by

**ZOULFEKAR MAZLOUM**

**DISSERTATION**

Submitted to the Graduate School

of Wayne State University,

Detroit, Michigan

in partial fulfillment of the requirements

for the degree of

**DOCTOR OF PHILOSOPHY**

2022

MAJOR: PHYSICS

Approved By:

Advisor Date

# ACKNOWLEDGEMENTS

First and foremost, I would like to express my gratitude to my advisor, Prof. Sean Gavin, for his essential guidance, consistent support, and patience throughout my Ph.D study period. His vast expertise and wealth of experience have served as a source of inspiration for me throughout my academic study and everyday life. I would also want to express my gratitude to Prof. George Moschelli for his technical and invaluable assistance with my research, which was extremely helpful in developing my experiment procedures and critically evaluating my results. I also thank Prof. Joren Putschke and Prof. William Llope for their mentorship. It is because of their kind assistance and support that my studies and life in the United States have been such a joy.

Finally, I would want to convey my thanks to my parents, my wife (Fatemah), and my children (Adam & Hussein) for all the support and motivation they have given me throughout my journey. It would have been difficult for me to complete my studies if it hadn't been for their wonderful understanding and encouragement throughout the previous several years.

> “ Everybody is a genius. But if you judge a fish by its ability to climb a tree, it will live its whole life believing that it is stupid.”
>
> – Albert Einstein

## TABLE OF CONTENTS

# LIST OF FIGURES

# LIST OF TABLES

# CHAPTER 1 INTRODUCTION

## 1.1 What are the benefits of QGP study?

When Edwin Hubble found in 1929 that the distance between galaxies is directly proportionate to the speed at which they are moving away from us, he coined the term ″expanding universe″. It's clear to see how the universe gets smaller and smaller as we travel back in time (Figure 1.1). A time (now estimated to be 14 billion years ago) when the whole universe was confined in a single point in space may be reached by going backwards farther in our time travel. Big Bang must have been a single, cataclysmic event that established the universe as we know it today.

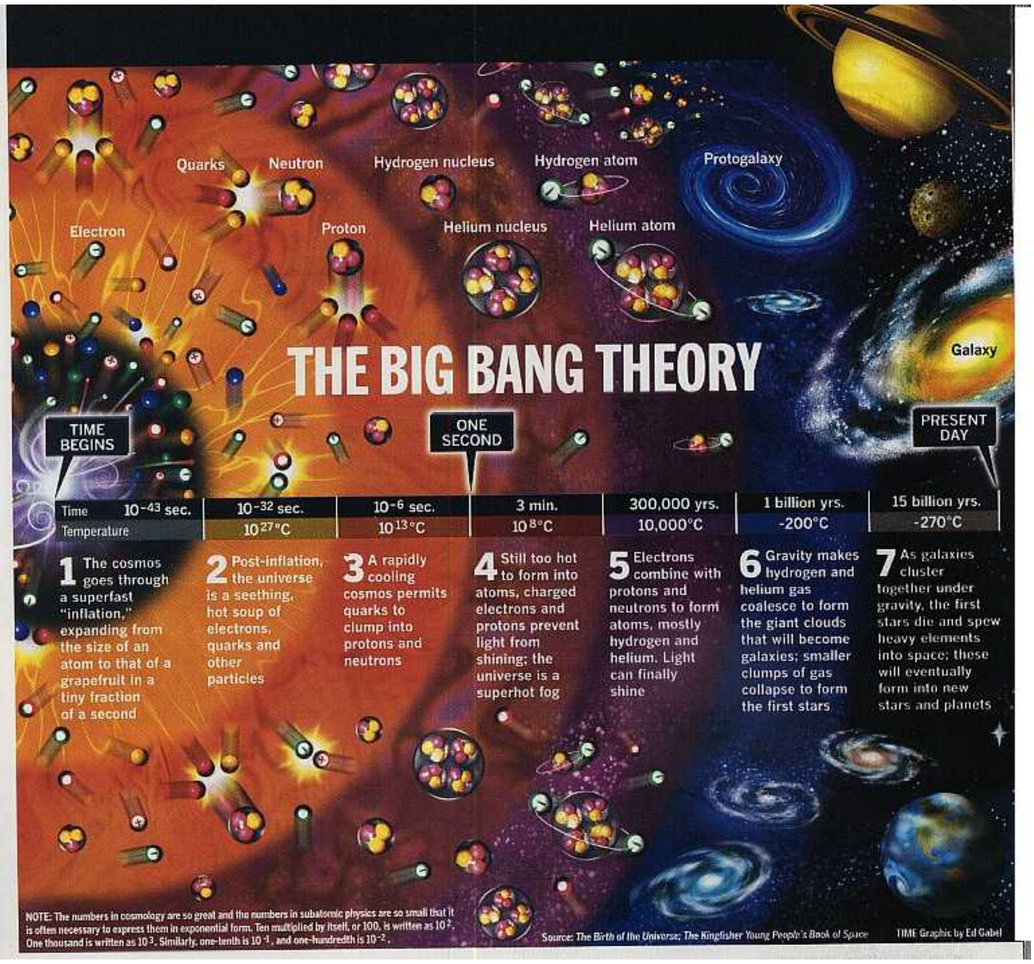

1 The cosmos goes through a superfast "inflation," expanding from the size of an atom to that of a grapefruit in a tiny fraction of a second

2 Post-inflation, the universe is a seething, hot soup of electrons, quarks and other particles

3 A rapidly cooling cosmos permits quarks to clump into protons and neutrons

4 Still too hot to form into atoms, charged electrons and protons prevent light from shining; the universe is a superhot fog

5 Electrons combine with protons and neutrons to form atoms, mostly hydrogen and helium. Light can finally shine

6 Gravity makes hydrogen and helium gas coalesce to form the giant clouds that will become galaxies; smaller clumps of gas collapse to form the first stars

7 As galaxies cluster together under gravity, the first stars die and spew heavy elements into space; these will eventually form into new stars and planets

NOTE: The numbers in cosmology are so great and the numbers in subatomic physics are so small that it is often necessary to express them in exponential form. Ten multiplied by itself, or 100, is written as $10^{2}$. One thousand is written as $10^{3}$. Similarly, one-tenth is $10^{-1}$, and one-hundredth is $10^{-2}$.

Source: *The Birth of the Universe; The Kingfisher Young People's Book of Space*

TIME Graphic by Ed Gabel

Figure 1.1: The Evolution of the Big Bang Theory.

QGP [1] has to have existed at some point in the very early history of the universe.

---

[1] Quark-gluon plasma (QGP) is a soup of Quarks and gluons that scientists have been trying to recreate for the past decade by smashing atom nuclei together with enough energy to generate trillion-degree temperatures.

According to the Big Bang theory, the universe has gone through numerous stages of evolution because it was created 14 billion years ago.

When it comes to studying nuclear matter the nucleus–nucleus collision technique is widely established. When a nucleus collides with another nucleus with relativistic energy, it goes through many phases. Figure 1.2 depicts a schematic representation of the various stages of the collision as it occurs.

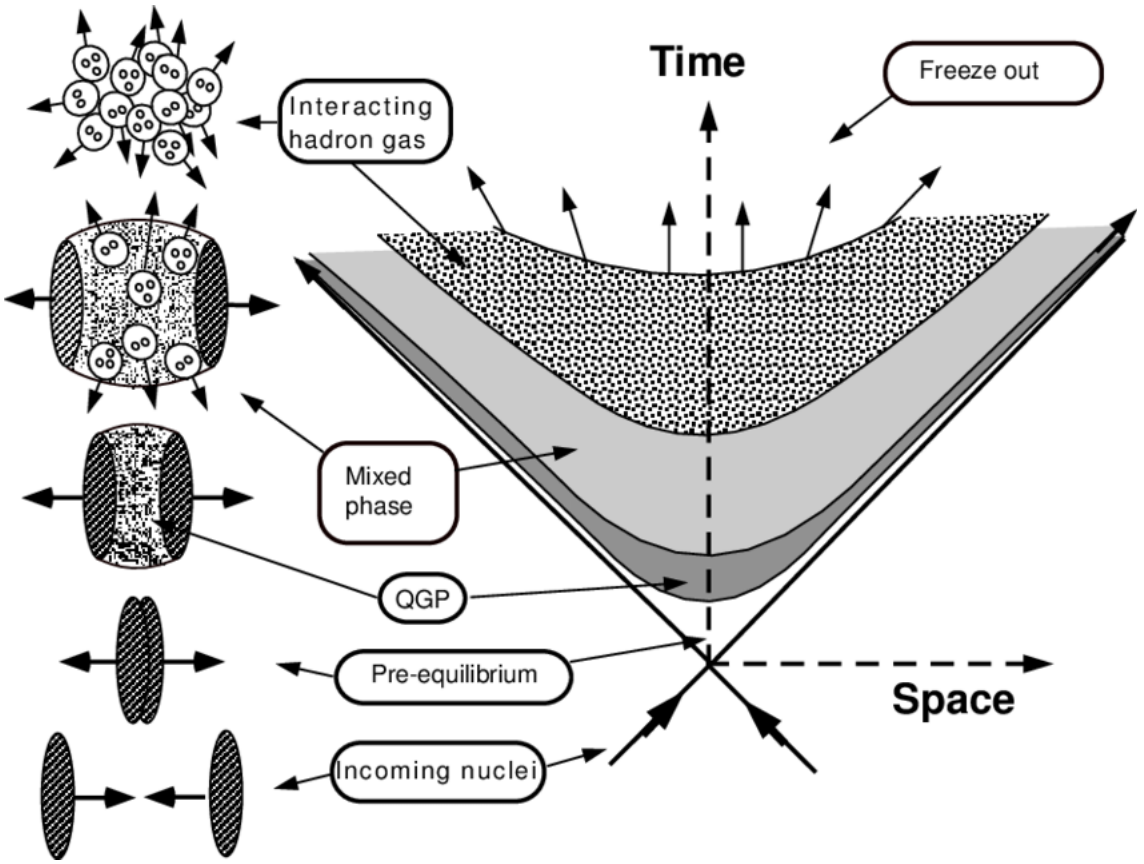

Figure 1.2: Space-time diagram of a nucleus-nucleus collision, illustrating the many stages of the expanding matter[1]

At the pre-equilbrium stage, the collisions are at the partonic level. The collisions between the initial partonic result in the formation of a fireball in an extremely excited state. The fireball is most likely not in equilibrium. Fireball constituents frequently collide, establishing a local equilibrium condition. The period of time required to achieve local equilibrium is referred to as the thermalization time. While in the QGP stage, thermal pressure exists in the system, acting in opposition to the surrounding vacuum. The fireball then expands collectively (hydrodynamically).The energy density of the system reduces as it expands, and the system cools. During the hadronization stage (Mixed phase-Interacting hadron gas), the entropy density will fall quite quickly over a short temperature interval.Because total entropy cannot be reduced, the fireball will grow fast while the temperature remains essentially constant.

Relativistic heavy ion collisions can be modeled in a variety of ways. They fall into two categories: a static model and a dynamic model. Modeling the freeze-out situation is the goal of the static models, which are used to explain experimental results. However, they make no attempt to provide an explanation for how the freeze-out situation is achieved. Dynamical models make an attempt to solve this question. At the moment, two types of dynamical models are popular: those that take a transport approach and those that take a hydrodynamic approach. Within certain approximations, the development of the system from pre-equilibrium through freeze-out may be represented using the transport approach. On the other hand, hydrodynamic models are limited to expanding until the freeze-out stage. We used in the thesis kinetic theory in order to study the evolution of the system, since the goal of kinetic theory is to comprehend the process of approaching equilibrium.

## 1.2 Motivation

For the study of relativistic nuclear collisions, two-particle correlations are an often used tool. Multiplicity fluctuations between charge and particle species have been investigated as a possible signal for QGP and the QCD critical point[2]. All of these fluctuation investigations involve particle variances that can be traced back to a two-particle correlation function. The shear relaxation time, the shear viscosity per entropy density and temperature fluctuations have all been extracted using momentum correlations and momentum covariance fluctuations, which are all derived from the same correlation function. In this thesis we will study two major things

The first major study is, these correlation observables are also used to conduct searches

---

[2] Quantum Chromodynamics is a basic quantum field theory that describes the strong interaction between quarks and gluons. It has been successfully used to a broad variety of phenomena, ranging from hadron spectra to inelastic collisions.

Lately, there has been a great deal of theoretical and experimental interest in the search for QCD critical point. The possibility of this point existence has been discussed for a long time [2, 3].

for critical fluctuations. Several number as well as momentum density correlation observables are linked mathematically, and we discuss the various physical mechanisms that have been attributed to each of these observables. In addition, a new multiplicity-momentum correlation is included in this set of observables. Our mathematical relationship may be used to validate observations, to understand the relative contributions of various physical mechanisms to correlation observables, and to evaluate the ability of theoretical and experimental models to concurrently explain all observables. With respect to all of the observables in the collection, we compared the independent source model against simulations from PYTHIA.

The other major objective of this thesis is to establish theoretical and phenomenological techniques for examining the nonequilibrium characteristics of correlation measurements. Our study in this case is based on a relaxation time approximation of the Boltzmann-Langevin equation.

# CHAPTER 2 BACKGROUND

The purpose of this chapter is to provide you with some background information that will be useful as you progress through the text. We'll start with a straightforward description of an ion collision to establish some terms. The two ions are approaching each other along the z-axis, which is specified by the direction of the beam. As a result, the x- and y-axes are the transverse directions in relation to the beam. One of the ions is labeled as the projectile, while the other is designated as the target ion (with non-fixed target colliders, the choice is random). With the help of the Glauber model, we were able to determine two important centrality variables: the number of binary collisions ($N_{coll}$) and the number of participants ($N_{part}$), which were calculated in relation to the impact parameter ($b$) of a collision.

One of the most remarkable characteristics of relativistic heavy-ion collisions is the rapid transverse expansion that occurs. According to the transverse momentum spectrum calculated from RHIC, the hadronic average final state transverse velocity is greater than the transverse velocity of a freely expanding heat source on average. A scenario using a blast wave can be used to simulate the situation at RHIC which we will obtain its features in this chapter.

We'll use natural units for the rest of this thesis, thus ( speed of light $'c'$ = Planks constant $'\hbar'$ = Boltzmann constant $'k_B' = 1$). Furthermore, Greek letters represent both space and time ($\mu = \nu = 0, 1, 2, 3$), whereas Latin letters represent just spatial components ($i, j = 1, 2, 3$). Three-vectors have a Latin index or are stated in bold font, whereas four-vectors always have a Greek index. Einstein summation notation is also used.

## 2.1 Kinematic variables and four-vectors

Kinematics is the branch of dynamics concerned with the motion of objects without taking into account the forces acting on the objects. To describe particle interactions in heavy-ion collisions we introduce some of the important kinematic variables that are useful to describe a particle's position and momentum. In case of the position, we can write the contravariant four-vector as $\mathbf{x}^\mu = (x^0, x^1, x^2, x^3)$ where $\mu = 0, 1, 2, 3$ and

$$\mathbf{x}^\mu = (t, x, y, z) \tag{2.1}$$

Where $x^1 = x, x^2 = y$ and $x^3 = z$ are the spatial coordinates and $x^0 = t$ is the time coordinate.

By using the metric space $g^{\mu\nu} = \text{diag}(1, -1, -1, -1)$ we can define a covariant four vector as,

$$\mathbf{x}_\mu \equiv g_{\mu\nu} = (x^0, -x^1, -x^2, -x^3) = (t, -x, -y, -z). \tag{2.2}$$

The distance between $\mathbf{x}^\mu_a = (t_a, x_a, y_a, z_a)$ and $\mathbf{x}^\mu_b = (t_b, x_b, y_b, z_b)$ is calculated as

$$\begin{aligned} d\tau^2 &= (t_a - t_b)^2 - (x_a - x_b)^2 - (y_a - y_b)^2 - (z_a - z_b)^2 \\ &= dt^2 - dx^2 - dy^2 - dz^2 \end{aligned} \tag{2.3}$$

Where $\tau = \sqrt{t^2 - x^2 - y^2 - z^2}$ is called proper time and invariant under Lorentz transformation.

In Figure 2.1, the space–time continuum has been portrayed in two dimensions, $t$ and $z$. The region of space–time for which $\tau^2 > 0$ is referred to as the time-like zone, whereas $\tau^2 < 0$ is referred to the space-like region. The $t = z$ line is referred to be light-like (only particles with neglected masses can travel along this line). A physical particle cannot enter the space-like area because it must travel faster than light. Figure 2.1 shows how the light-like surfaces will form a cone. Only the forward/future light-cone region is openable to physical particles.

In relativity, a particle with four-momentum is expressed as $p^\mu = (E, \mathbf{p}) = (E, p_x, p_y, p_z)$. However, variables, transverse mass $m_t$ and rapidity $y$, are more convenient to use. A particle's transverse mass $m_t$ and rapidity $y$ are defined as,

$$m_t = \sqrt{m^2 + p_t^2} \tag{2.4}$$

$$\begin{aligned} y &= \frac{1}{2}\ln\frac{E + p_z}{E - p_z} = \frac{1}{2}\ln\frac{1 + p_z/E}{1 - p_z/E} \\ &= \tanh^{-1}\frac{p_z}{E} = \tanh^{-1}(\beta). \end{aligned} \tag{2.5}$$

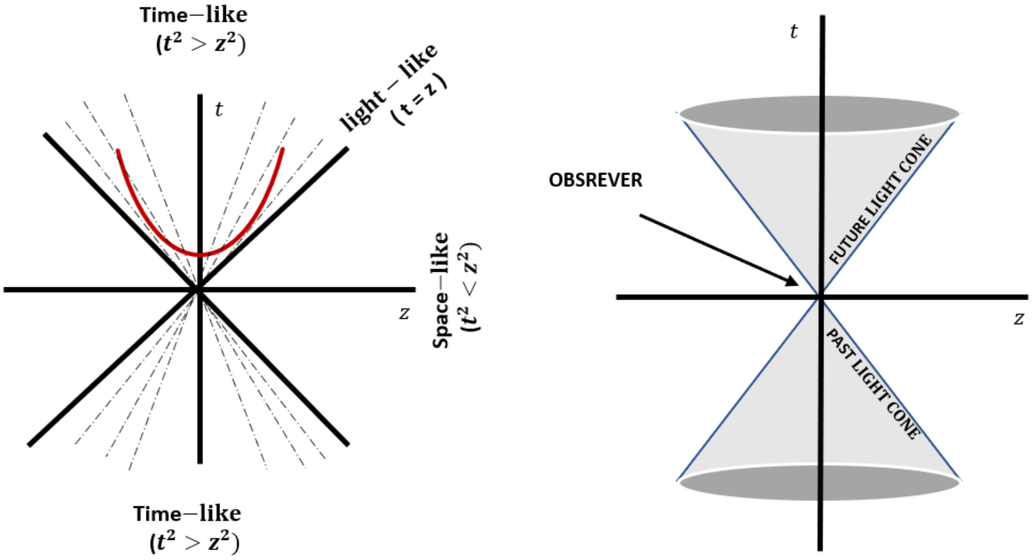

Figure 2.1: Left side is the space-time diagram in $(z, t)$ dimensions. The time-like region refers to $t$-axes and the space-like region refers to $z$-axes. The red curve is a proper time curve. The right side includes the picture of a past light cone and future light cone. At the origin, in relativistic heavy ion collisions the nuclei will collide (observable).

Where $p_t = \sqrt{p_x^2 + p_y^2}$ from equation (2.4) is the transverse momentum. From the first equality in Equation (2.5) the inverse transformation for $E = m_t \cosh y$ and $p_z = m_t \sinh y$. Rapidity may be viewed as another way of expressing a particle's longitudinal velocity. In some aspects, it acts more naturally than the velocity at relativistic speeds. To begin, the domain of definition of rapidity is from $-\infty$ to $+\infty$ , as one would anticipate of velocity in a non-relativistic situation. Second, as with non-relativistic speeds, rapidity is additive when the coordinate system is boosted.

From Equation (2.5) we can study two explicit limits. Firstly the non-relativistic limit when $\mathbf{p} \ll m$ and secondly at very high energy when $m \ll \mathbf{p}$ where in the second case the mass can be neglected.

When $\mathbf{p} \ll m$, equation (2.5) can be written as

$$\begin{aligned} y &= \frac{1}{2} \ln \frac{m + m v_z}{m - m v_z} = \frac{1}{2} \ln\left(1 + v_z\right) - \frac{1}{2} \ln\left(1 - v_z\right) \\ y &\approx v_z \end{aligned} \tag{2.6}$$

It is important to note that rapidity describes a particle's velocity, but spatial rapidity specifies the particle's position. As a result, we can observe that there is a substantial connection between velocity and position in this specific example.

In high-energy nuclear scattering, the collision axis is taken along the $z$-axis, which is also known as the beam axis. $\theta$ is the emitted angle for a particle as a function of the beam axis, $z$, the rapidity variable can be written as

$$y = \frac{1}{2} \ln \frac{\sqrt{m^2 + \mathbf{p}^2} + |\mathbf{p}| \cos\theta}{\sqrt{m^2 + \mathbf{p}^2} - |\mathbf{p}| \cos\theta}. \tag{2.7}$$

Now in case when $m \ll \mathbf{p}$ we can neglect the mass,

$$\begin{aligned} y = & \ \frac{1}{2} \ln \frac{|\mathbf{p}| + |\mathbf{p}| \cos\theta}{|\mathbf{p}| - |\mathbf{p}| \cos\theta} \\ y = & -\ln \tan(\theta/2) \equiv \eta, \end{aligned} \tag{2.8}$$

where $\eta$ is the pseudo-rapidity. From equation (2.8) we noticed that the pseudo-rapidity only depends on $\theta$. It is a useful parameter for experimentalists when information about the particle, such as mass, momentum, and so on, are unknown and just the angle of emission is known. Let us focus on one-dimensional Bjorken scaling flow reference [4] for illustration purposes. Bjorken proposed that physics is rapidity independent, i.e. boost-invariant, based on the fact that the rapidity density $dN/dy$ is flat in high-energy collisions. If transverse expansion is ignored, hydrodynamic four-velocity for a boost-invariant system may be stated as

$$u^\mu = \left( \frac{t}{\tau}, 0, 0, \frac{z}{\tau} \right) \tag{2.9}$$

Where $t/\tau = \cosh\eta$ and $z/\tau = \sinh\eta$.

Because the system is boost-invariant, the hydrodynamic equations may be solved at rapidity $\eta = 0$ and then boosted to any finite rapidity. At $\eta = 0$, the hydrodynamic four-velocity is represented as $u^\mu = (1, 0, 0, 0)$. The model's simplicity is demonstrated by using it to quickly obtain a few equations that describe the evolution of a few thermodynamic variables in an expanding Bjorken system. To accomplish so, we employ two useful identities.

$$\partial_\mu u^\mu = \frac{1}{\tau} \tag{2.10}$$

$$u^{\mu}\partial_{\mu} = \frac{\partial}{\partial \tau}. \tag{2.11}$$

The appropriate stress–energy for an ideal gas are written as,

$$T^{\mu\nu} = (\varepsilon + p)\, u^{\mu} u^{\nu} - p g^{\mu\nu} \tag{2.12}$$

then, using energy-momentum conservation for equation (2.12),

$$\begin{aligned} u_{\nu}\partial_{\mu}T^{\mu\nu} &= 0 \\ \frac{\partial \varepsilon}{\partial \tau} + \frac{\varepsilon + p}{\tau} &= 0 \end{aligned} \tag{2.13}$$

If the fluid is considered to be free of baryons, The entropy density is defined as $s = (\varepsilon + p)/T$, and equation (2.13) may be rewritten as

$$\frac{d\tau s}{d\tau} = 0. \tag{2.14}$$

$s\tau =$ constant can be used to solve equation (2.14). Isentropic flow is one-dimensional flow. $s$ is proportion to $T^3$ in an ideal gas gives us the well-known $T^3$ rule for Bjorken scaling expansion.

$$T_0^3 \tau_0 = T_f^3 \tau_f, \tag{2.15}$$

The subscripts 0 and $f$ correspond to the fluid's initial and final states, respectively. Similarly, the number conservation equation may be solved. For fluid velocity $u^{\mu} = (1, 0, 0, 0)$, $n^{\mu} = (n, 0, 0, 0)$.

$$\begin{aligned} u_{\nu}\partial_{\mu}n^{\mu\nu} &= 0 \\ \partial_{\tau} n + \frac{n}{\tau} &= 0 \end{aligned} \tag{2.16}$$

.

The problem may be solved to produce the following result:

$$n_f = n_0 \frac{\tau_0}{\tau_f} \tag{2.17}$$

As a result, both entropy and particle density in the Bjorken model decrease as the inverse of proper time via $s_f = s_0 \frac{\tau_0}{\tau_f}$ and $n_f = n_0 \frac{\tau_0}{\tau_f}$. While these equations are only valid for an ideal fluid undergoing Bjorken expansion, they will suffice for approximations later on.

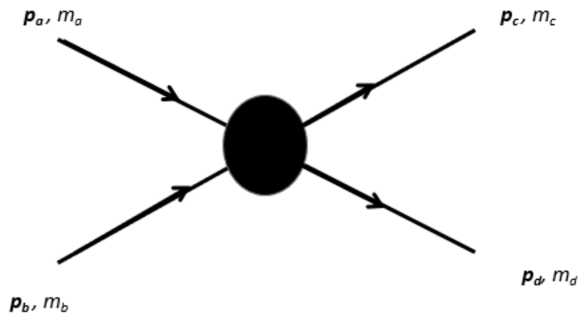

Figure 2.2: Two-particle scattering diagram of the $a + b \to c + d$ process.

Finally, in figure (2.2), given a two particles collision process with incoming and outgoing momenta and masses. The incoming momenta and masses are $\mathbf{p}_a$, $\mathbf{p}_b$, $m_a$ and $m_b$. The outgoing momenta and masses are $\mathbf{p}_c$, $\mathbf{p}_d$, $m_c$ and $m_d$. The Mandelstam variables $s, u$ and $t$ are defined as,

$$s = (\mathbf{p}_a + \mathbf{p}_b)^2 = (\mathbf{p}_c + \mathbf{p}_d)^2 \tag{2.18}$$

$$u = (\mathbf{p}_a - \mathbf{p}_d)^2 = (\mathbf{p}_b - \mathbf{p}_c)^2 \tag{2.19}$$

$$t = (\mathbf{p}_a - \mathbf{p}_c)^2 = (\mathbf{p}_b - \mathbf{p}_d)^2. \tag{2.20}$$

Where $s, u$ and $t$ are also called Lorentz-invariant Mandelstam variables. They are dependent and constrained by the following relation:

$$s + u + t = m_a^2 + m_b^2 + m_c^2 + m_d^2 = constant. \tag{2.21}$$

$\sqrt{s}$ is used to describe the entire collision energy, and this number represents the strength of a collision for example see Table 2.1 for different energies.

## 2.2 Glauber model

Only a few model inputs are needed to see the difference between the geometric results of this model with real experimental data. The most important things are the energy dependence of the nucleon-nucleon inelastic cross-section and the profile nuclear density of the colliding nuclei.

In this work, we used the Glauber model [5] to calculate two relevant centrality variables: The first one is the number of participants, $N_{part}$, and the second one is the number of binary collisions, $N_{coll}$, based on a collision's impact parameter, $b$. It is important to find the probability that a pair of nucleus will overlap, in order to calculate the collisions between participant nucleons in a heavy-ion collision. Assuming a two-dimensional projection of the nuclei $A$ and $B$ as two colliding circles with some overlap in between as shown in figure 2.3, the overlap function defined as:

$$T_{AB}(\vec{b}) = \int d^2\vec{s}T_A(\vec{s})T_B(\vec{b}-\vec{s}) \tag{2.22}$$

The nuclear thickness functions for target $A$ and projectile $B$ are:

$$T_{A/B}(\vec{b}) = \int \rho_{A/B}(\vec{b}, z_{A/B})dz_{A/B}. \tag{2.23}$$

Where $\rho_{A/B}(\vec{b}, z_{A/B})$ is the probability to find a nucleon in a projectile $B$ or target $A$ at a point $(\vec{b}, z_{A/B})$ per unit volume normalized to unity, and $\rho_{A/B}$ is the nuclear density for target $A$ or projectile $B$.

In most cases, the Glauber model assumes that the nucleon density inside the nucleus is of the Woods Saxon [6] form.

$$\rho(r) = \frac{\rho_0}{1+e^{\frac{r-R}{a}}} \tag{2.24}$$

where $R$ is the nuclear radius and $a$ corresponds to diffusioness parameter. $\rho_0$ is the normalized density. We can take spherical shape as an example to find,

$$\int \rho dV = \int_0^\infty 4\pi r^2\rho(r)dr = A \tag{2.25}$$

where $A$ is the atomic mass in the nucleus.

For example, hard-sphere shape.

$$\begin{aligned} \rho &= \rho_0, r < R \\ &= 0, r \geq R \end{aligned}$$

From this example, the normalization density can be expressed as,

$$\rho_0 = \frac{A}{\frac{4}{3}\pi R^3} \tag{2.26}$$

For a gold nucleus($A - 197$), the normalization density in the order of 0.16 $nucleon/fm^3$. Where $R$ is assumed to be $\sim R_0 A^{1/3}$ in case of $R_0$ approximately $1.12 fm$ and $a \sim 0.545 fm$ [6].

The real value of the radius, $R$, in terms of $A$ is given by the empirical relationship described below [7]:

$$R = 1.12 A^{1/3} - \frac{0.86}{A^{1/3}} \tag{2.27}$$

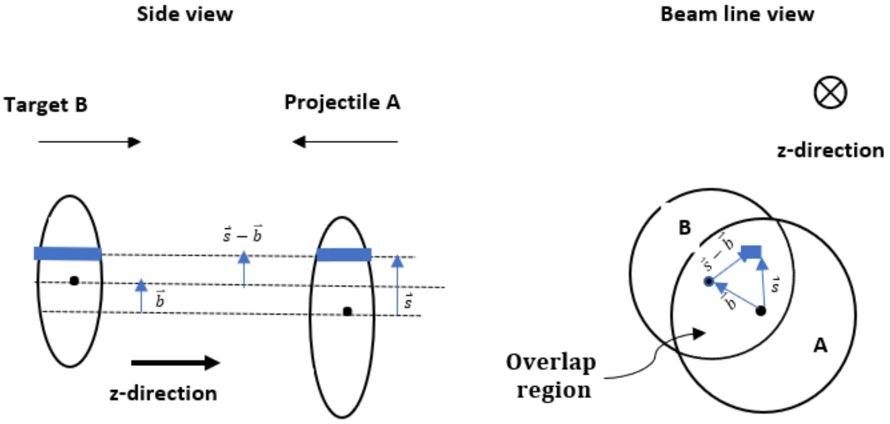

Figure 2.3: Schematic diagram of optical Glauber model includes two views: side view and beam-line view.

By using a binomial probability the inclusive inelastic cross-section can be derived from:

$$\sigma_{AB}(\vec{b}) = \int d\vec{b}[1 - e^{-\sigma_{inel}^{NN} T_{AB}(\vec{b})}] \tag{2.28}$$

where $\sigma_{inel}^{NN}$ is the nucleon-nucleon cross section, taken from proton-proton colisions with different values for different energies given in the Table 2.1.

Now, the binary collisions, $N_{coll}$, is [6]

$$N_{coll} = \sigma_{inel}^{NN} \int ds dz_A dz_B \rho_A(z_A, s) \rho_B(z_B, s - b) = \sigma_{inel}^{NN} T_{AB}(b) \tag{2.29}$$

The number of participants, $N_{part}$, is [6]

$$N_{part} = \int ds^2 [T_A(s)(1 - e^{\sigma_{inel}^{NN} T_B(|\vec{b} - \vec{s}|)}] + T_B(|\vec{b} - \vec{s}|)(1 - e^{\sigma_{inel}^{NN} T_A(s)}) \tag{2.30}$$

| $\sqrt{s}$ $(GeV)$ | $\sigma_{inel}^{NN}$ $(fm^2)$ | **Reference** |
|---|---|---|
| 11.5 | 3.08 | [8] |
| 19.6 | 2.973 | [8] |
| 27 | 3.194 | [8] |
| 39 | 3.098 | [8] |
| 62.4 | 3.155 | [8] |
| 200 | 4.2 | [9] |
| 2760 | 6.4 | [9] |

Table 2.1: For a given beam energy, experimental values of $\sigma_{inel}^{NN}$ are given.

We applied this model to the Lead ($^{208}Pb$) nuclei ($Pb - Pb$ collision) and Gold ($^{197}Au$) nuclei ($Au - Au$ collisions) in order to get the binary nucleon-nucleon collisions by using equation (2.29) and the number of participants by using equation (2.30) as a function of impact parameter. We used those parameters in our blast wave to find all the observables and compare the correlation transverse-momentum fluctuation to experimental data from STAR and ALICE .

### 2.3 Features of the blast wave model

One of the most well-studied elements of heavy ion collisions is the transverse expansion of the collision volume. Experimental studies of azimuthal anisotropy have provided compelling proof that the thermalized system's expansion may be represented hydrodynamically [10]. To get the data required to solve the problems addressed in this thesis, hydrodynamical simulations must run millions of events. As a result, we resort to the blast wave [1] model, a simplified model of transverse expansion.

Several researchers have utilized the blast wave model to evaluate experimental data from relativistic energy in heavy-ion collisions [11, 12, 13, 14]. The blast wave model predicts that a fireball will be created during a collision, which grows rapidly to the freeze-out state. As a result, the model implies that all particles freeze out at the same moment, measured in a frame that travels longitudinally with the expanding fireball's fluid element. Most crucially in this model is that the final fluid parameters are independent of the development details and may be treated as parameters. The blast wave model will

---

[1] A blast wave is formed when a tremendous quantity of energy $E$ is released in an infinitesimally small volume surrounded by a medium of density $\rho$.

describe the transverse expansion, surface velocity $\beta$ and the freeze-out temperature $T$. Due to its simple structure, it describes elliptic flow and transverse momentum spectra adequately [12, 14]. On the other hand, the blast wave model suffers from its simplicity, this means no information concerning the particle production, hadronization, perturbative processes of QCD, and so on. Nevertheless, it's a useful model in our studies and the version of the blast wave model that is used in this work was used in reference [14]. The model attempts to characterize the particle momentum distribution on the freeze-out surface $\sigma$, which is defined by the proper final time $\tau_f$. To do so, we apply the Cooper-Frye formula [15], by considering a three-dimensional hypersurface $\sigma(\mathbf{x})$ in a Minkowski space-time with four dimensions and then count how many particles that will cross the hypersurface. The total number of particles that cross the hypersurface $\sigma$ can be written as,

$$N = \int_\sigma d\sigma_\mu j^\mu = \int_\sigma d^3\sigma_\mu \int \frac{d^3p}{E} p^\mu f(\mathbf{x}, \mathbf{p}) \tag{2.31}$$

where $j^\mu$ is the particle current and $f(\mathbf{x}, \mathbf{p})$ is chosen to be the Boltzmann distribution function [12]:

$$f(\mathbf{x}, \mathbf{p}) = Ae^{-\frac{u^\mu p_\mu}{T}} \tag{2.32}$$

where $A$ is the normalization factor of the distribution function and $u^\mu$ is the fluid velocity. The differential version of equation (2.31) can be written as

$$E\frac{dN}{d^3p} = \int_\sigma f(\mathbf{x}, \mathbf{p}) p^\mu d\sigma_\mu = \frac{dN}{dyd^2p_t}. \tag{2.33}$$

We can use this distribution function to find the rapidity, elliptic flow and the average transverse momentum

$$\frac{dN}{dy} = \int E\frac{dN}{d^3p} d^2p_t. \tag{2.34}$$

$$v_2 = \frac{\int \cos{(2\phi)} E\frac{dN}{d^3p} d^3p}{\langle N \rangle}. \tag{2.35}$$

$$\langle p_t \rangle = \frac{\int p_t E\frac{dN}{d^3p} d^3p}{\langle N \rangle}. \tag{2.36}$$

The value of observables in local equilibrium is the major reason for our interest in the blast wave model. We utilize it instead of more complex models because of it's accessibility, and we find it to be quite appropriate for our requirements. Reference [16] contains all of the model's information and characteristics.

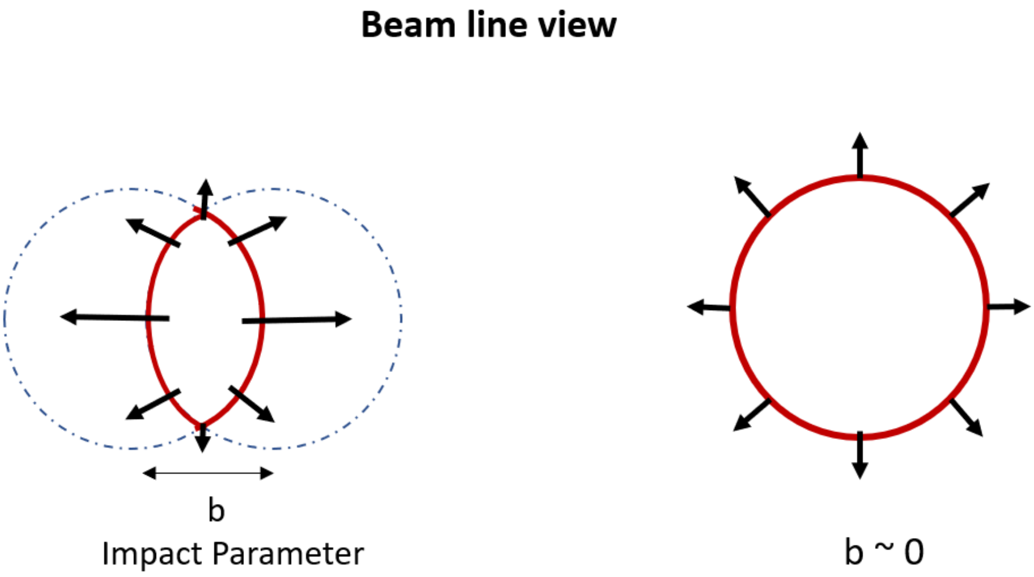

Figure 2.4: A graphic showing (on the left) an off-center collision resulting in anisotropic flow, and (on the right) a centered collision resulting in small elliptic flow.

One of the most important observables in heavy-ion collisions is the azimuthal distribution. The shape of a collision with a non-zero impact parameter ($b \neq 0$) collision is seen in Figure 2.4. The overlap zone between the two nuclei is known as the participant region, and at this region, the majority of collisions occur. On the periphery, the target and projectile fragments serve as spectators. Figure 2.4 shows that in collisions with non-zero impact parameters, the participant in coordinate space do not have azimuthal symmetry. As a result of many collisions between the constituent particles, this spatial anisotropy is transformed into momentum anisotropy of the created particles. Collective flow is the term used to describe the observed momentum anisotropy [17, 18], which has explanation in a hydrodynamic model [19].

In a Fourier analysis of distribution, values (the Fourier coefficients) that have physical significance are described mathematically.

$$\frac{2\pi}{N}\frac{dN}{d\phi} = 1 + 2\sum_{n=1,2,3..} v_n \cos\left[n(\phi - \Psi_{RP})\right] \tag{2.37}$$

Where $\phi$ is the azimuthal angle and $\Psi_{RP}$ is the reaction plane. The flow coefficients $v_n$ may be simply calculated.

$$v_n = \langle \cos\left[n(\phi - \Psi_{RP})\right] \rangle \tag{2.38}$$

The Fourier coefficients, $v_1, v_2, v_3$ and $v_4$ are called directed, elliptic, triangular and hexadecapole flow respectively.

The elliptic flow $v_2$ is a subject that has received significant attention in $\sqrt{s} = 200$ GeV gold-gold collisions at RHIC [20, 21] and in $\sqrt{s} = 2.76$ TeV lead-lead collisions at LHC [22, 23]. At the RHIC and LHC, a large elliptic flow has provided persuasive evidence that almost perfect fluid is created. The ratio of shear viscosity by entropy density, $(\eta/s)$, is the factor that determines how much a fluid deviates from its ideal behavior. Elliptic flow is highly sensitive to the value of $\eta/s$. The sensitivity of $v_2$ has been used to get phenomenological estimates of $\eta/s$ [24, 25].

In order to determine the correctness of our blast wave model, we use this code to calculate $\langle p_t \rangle$, $v_{2\{4\}}$ [2] and $dN/dy$. The figures below that show $\langle p_t \rangle$ and $v_{2\{4\}}$ as a function of $N_{part}$. The output data from our blast wave model (BW) denoted by the black solid curves compared to experimental data for energies $11.5, 19.6, 27, 39, 62.4$ and $200$ $GeV$ from RHIC and $2760$ $GeV$ from LHC.

---

[2] Without taking into account the non-flow terms, the cumulants have the following formulations[26],

$$v_{2\{4\}} = \sqrt{\langle v_2^2 \rangle}$$
$$v_{2\{4\}} =^4 \sqrt{2\left\langle v_2^2 \right\rangle^2 - \left\langle v_2^4 \right\rangle}$$

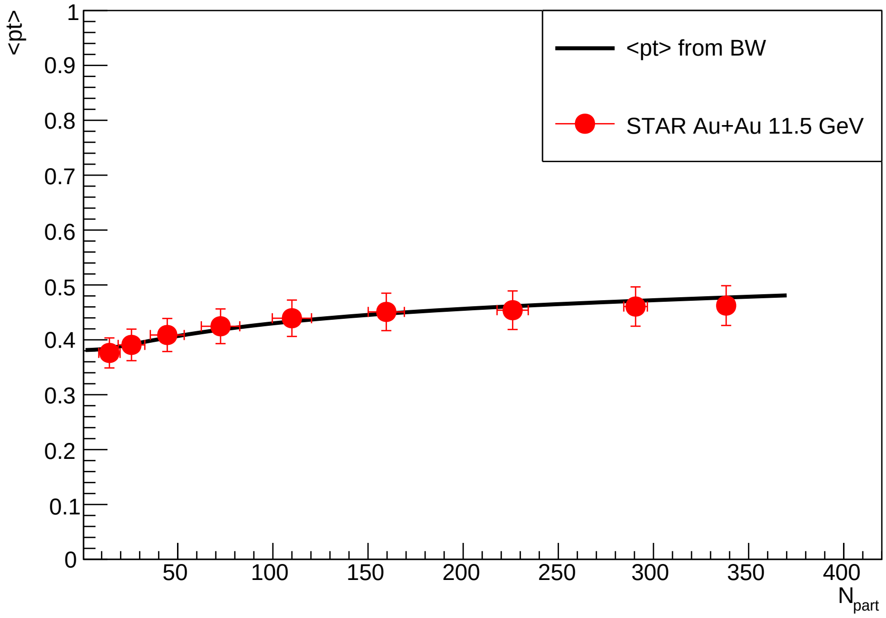

Figure 2.5: $\langle p_t \rangle$ for $Au - Au$ at $\sqrt{s} = 11.5\ GeV$ fits to experimental data for all charged particles with a constant temperature with centrality at 118 $MeV$. The solid line is the blast wave calculation, and the circles represent STAR data [27, 28].

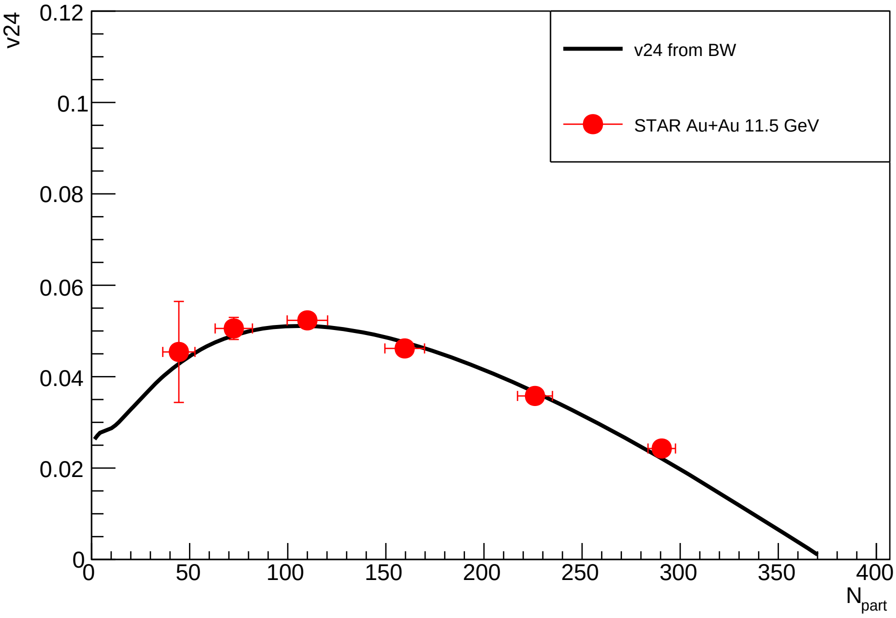

Figure 2.6: $v_{2\{4\}}$ for $Au - Au$ at $\sqrt{s} = 11.5\ GeV$ fits to experimental data for all charged particles with a constant temperature with centrality at 118 $MeV$. The solid line is the blast wave calculation, and the circles represent STAR data [27, 28].

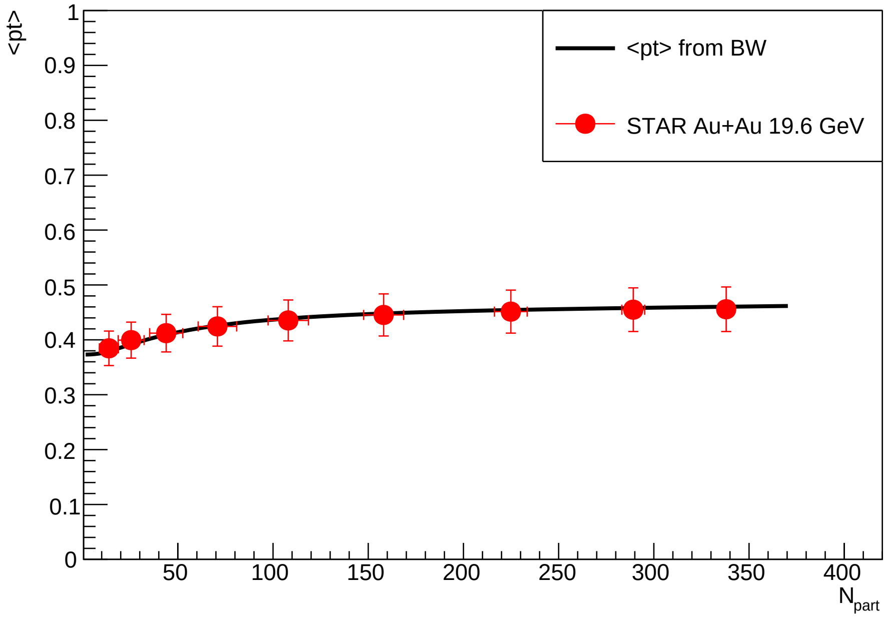

Figure 2.7: $\langle p_t \rangle$ for $Au - Au$ at $\sqrt{s} = 19.6\ GeV$ fits to experimental data for all charged particles with a constant temperature with centrality at 116 $MeV$. The solid line is the blast wave calculation, and the circles represent STAR data [27, 28].

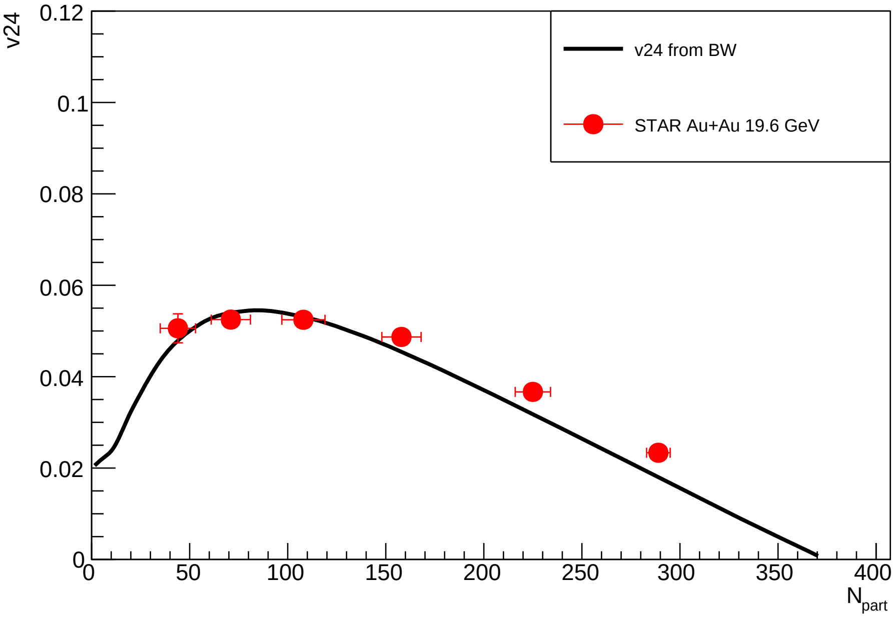

Figure 2.8: $v_{2\{4\}}$ for $Au - Au$ at $\sqrt{s} = 19.6\ GeV$ fits to experimental data for all charged particles with a constant temperature with centrality at 116 $MeV$. The solid line is the blast wave calculation, and the circles represent STAR data [27, 28].

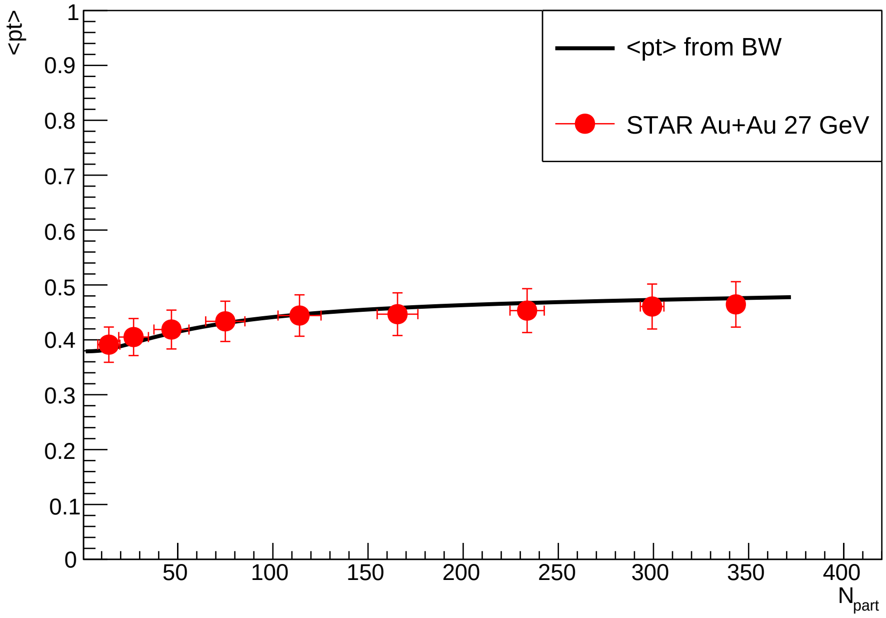

Figure 2.9: $\langle p_t \rangle$ for $Au-Au$ at 27 $GeV$ fits to experimental data for all charged particles with a constant temperature with centrality at 119 $MeV$. The solid line is the blast wave calculation, and the circles represent STAR data [27, 28].

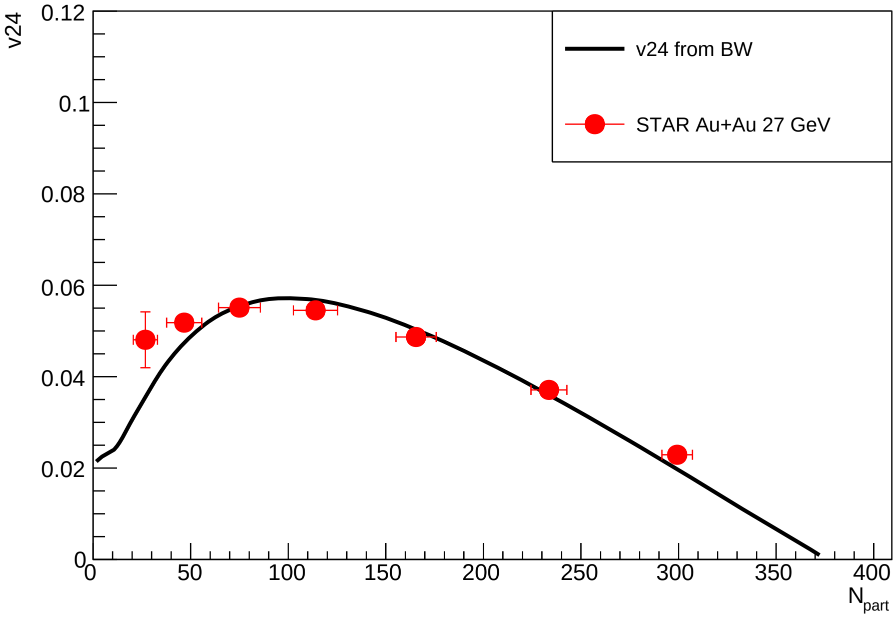

Figure 2.10: $v_{2\{4\}}$ for $Au-Au$ at 27 $GeV$ fits to experimental data for all charged particles with a constant temperature with centrality at 119 $MeV$. The solid line is the blast wave calculation, and the circles represent STAR data [27, 28].

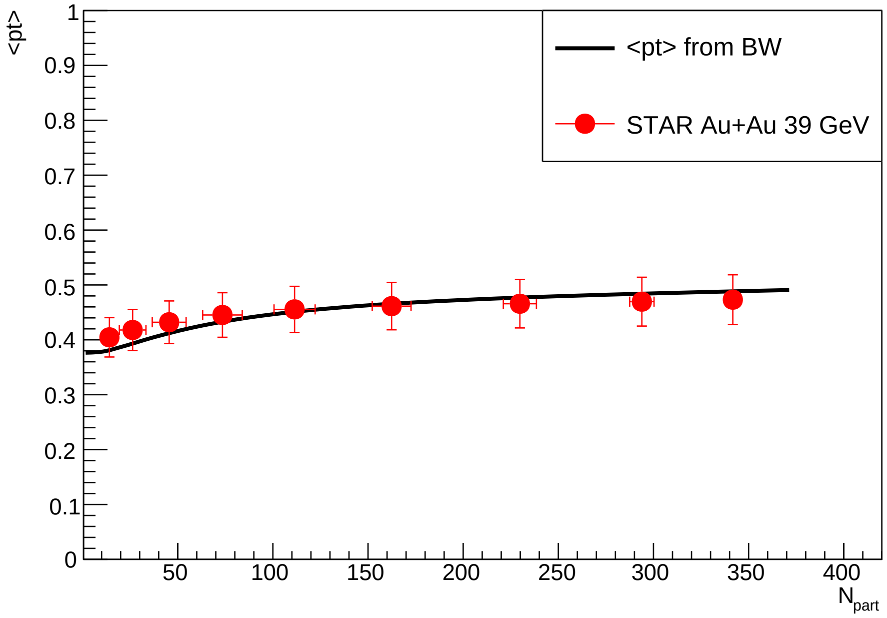

Figure 2.11: $\langle p_t \rangle$ for $Au-Au$ at 39 $GeV$ fits to experimental data for all charged particles with a constant temperature with centrality at 117 $MeV$. The solid line is the blast wave calculation, and the circles represent STAR data [27, 28].

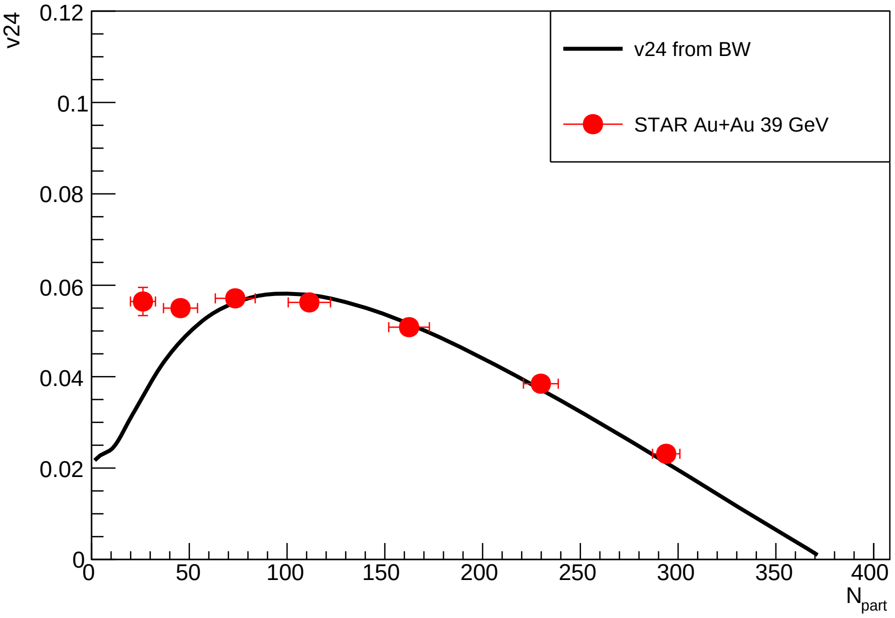

Figure 2.12: $v_{2\{4\}}$ for $Au-Au$ at 39 $GeV$ fits to experimental data for all charged particles with a constant temperature with centrality at 117 $MeV$. The solid line is the blast wave calculation, and the circles represent STAR data [27, 28].

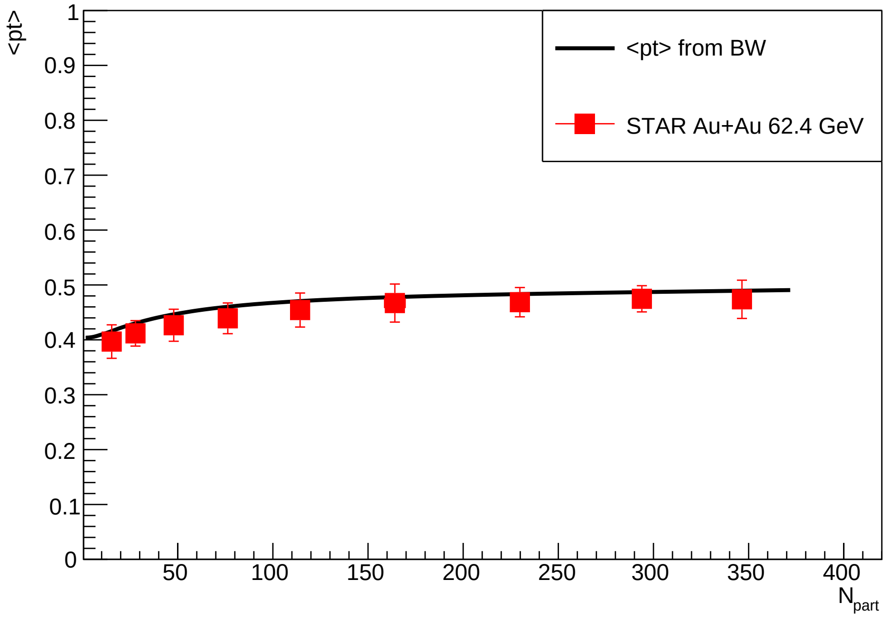

Figure 2.13: $\langle p_t \rangle$ for $Au - Au$ at 62.4 $GeV$ fits to experimental data for all charged particles with a constant temperature with centrality at 129.42 $MeV$. The solid line is the blast wave calculation, and the squares represent STAR data [29, 30].

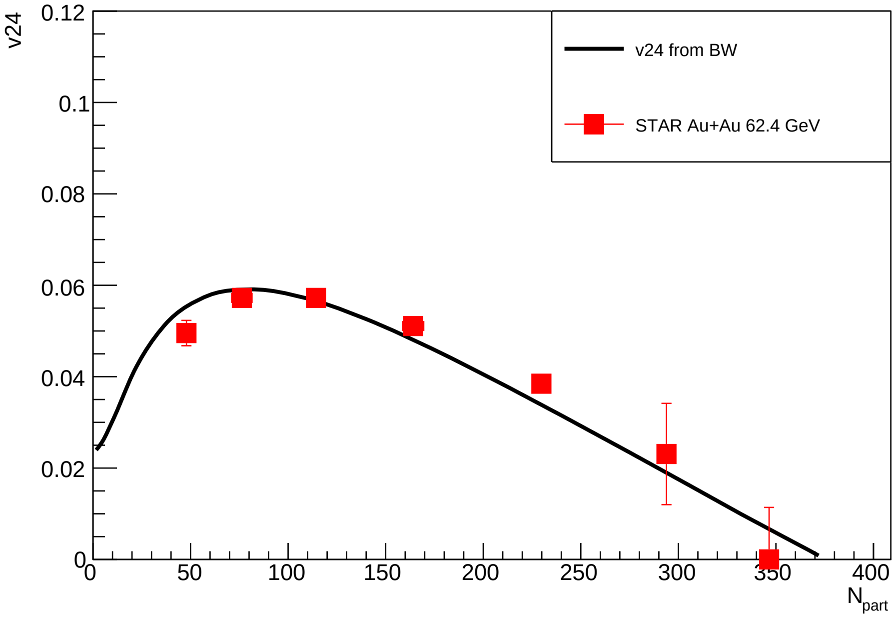

Figure 2.14: $v_{2\{4\}}$ for $Au - Au$ at 62.4 $GeV$ fits to experimental data for all charged particles with a constant temperature with centrality at 129.42 $MeV$. The solid line is the blast wave calculation, and the squares represent STAR data [29, 30].

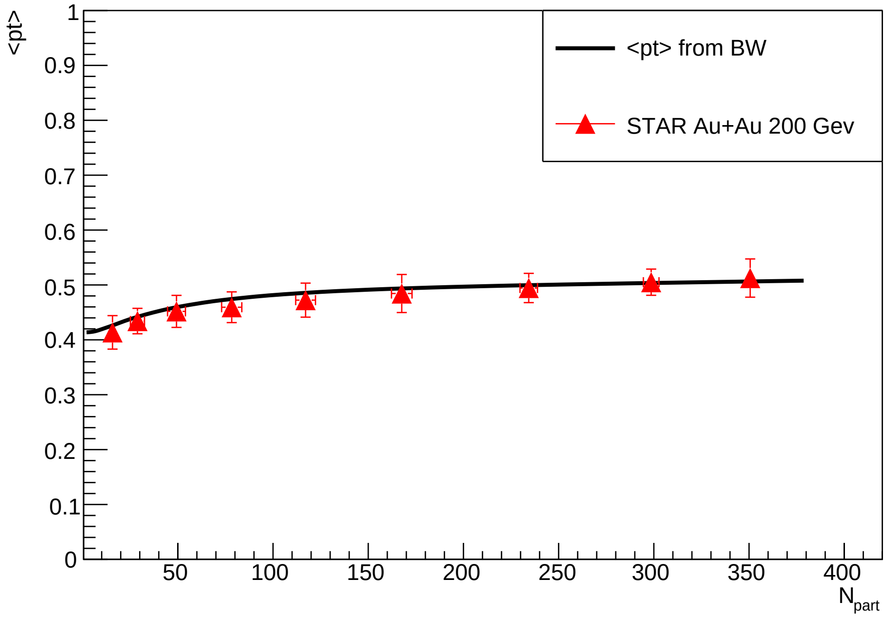

Figure 2.15: $\langle p_t \rangle$ for $Au-Au$ at 200 $GeV$ fits to experimental data for all charged particles with a constant temperature with centrality at 130 $MeV$. The solid line is the blast wave calculation, and the triangles represent STAR data [29, 30].

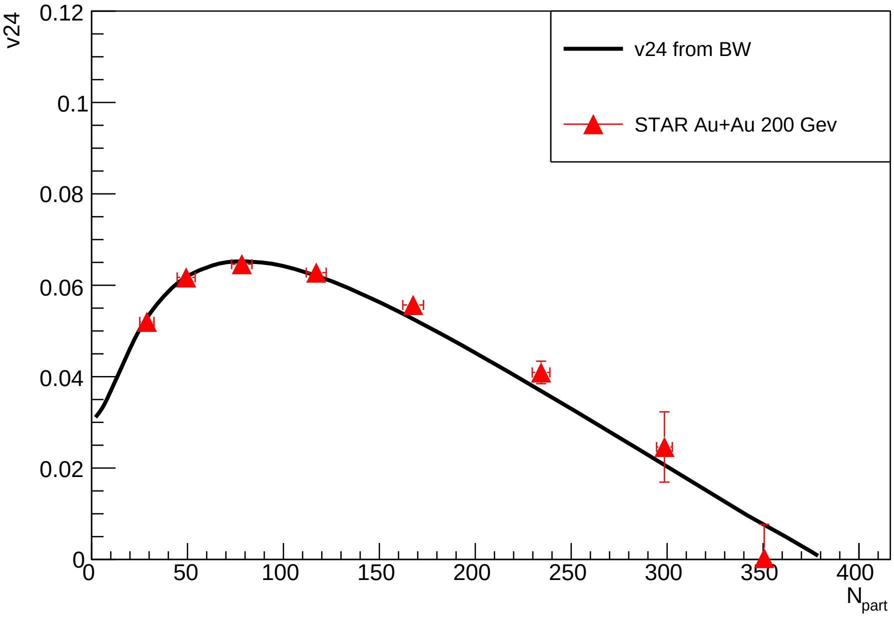

Figure 2.16: $v_{2\{4\}}$ for $Au - Au$ at 200 $GeV$ fits to experimental data for all charged particles with a constant temperature with centrality at 130 $MeV$. The solid line is the blast wave calculation, and the triangles represent STAR data [29, 30].

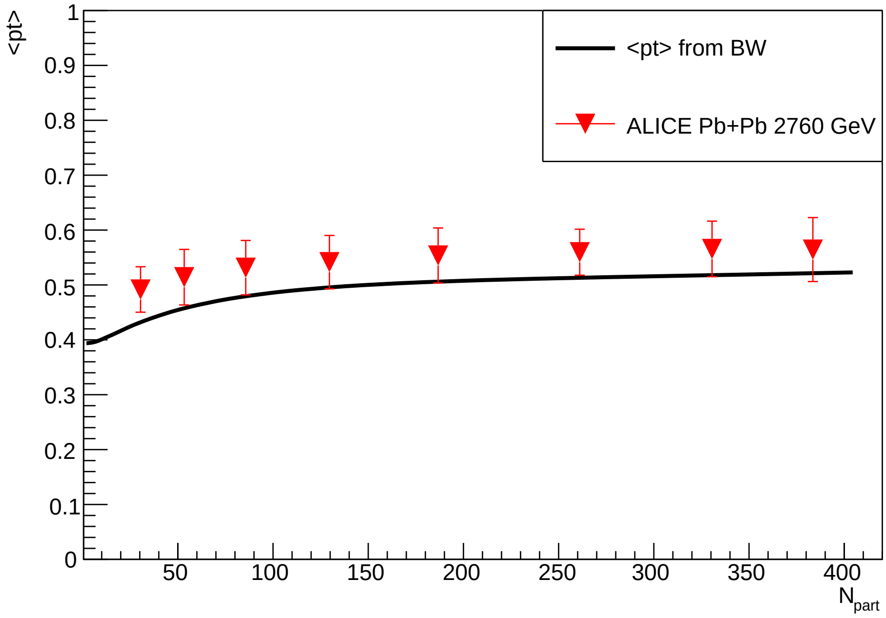

Figure 2.17: $\langle p_t \rangle$ for $Pb - Pb$ at 2760 $GeV$ fits to experimental data for all charged particles with a constant temperature with centrality at 117.7 $MeV$. The solid line is the blast wave calculation, and the triangles represent STAR data [31, 32].

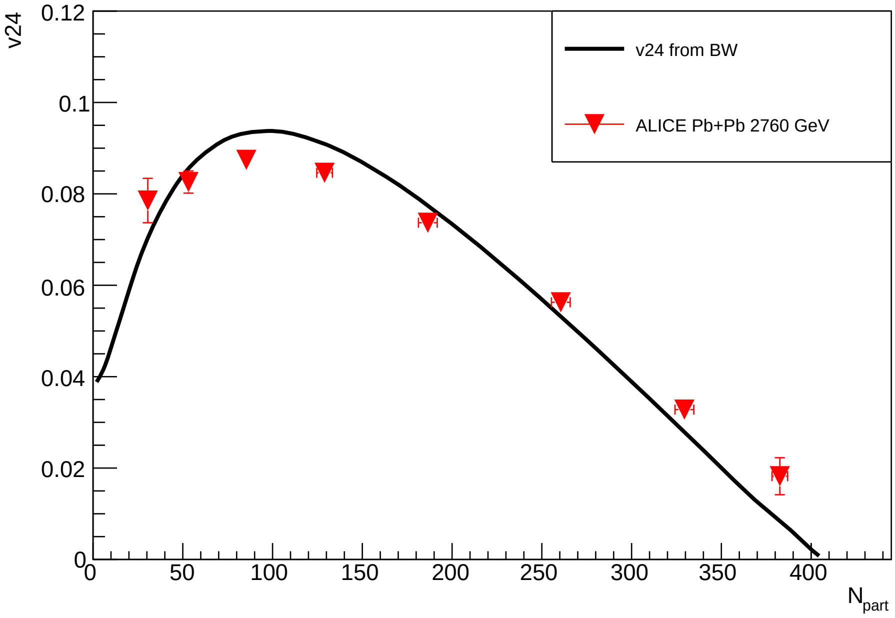

Figure 2.18: $v_{2\{4\}}$ for $Pb - Pb$ at 2760 $GeV$ fits to experimental data for all charged particles with a constant temperature with centrality at 117.7 $MeV$. The solid line is the blast wave calculation, and the triangles represent STAR data [31, 32].

Starting with energy $\sqrt{s} = 11.5\ GeV$, we can observe that both $\langle p_t \rangle$ (Figure 2.5) and $v_2\{4\}$ (Figure 2.6) from the blast wave match extremely well to the data from STAR at this energy; on the other hand, for $\sqrt{s} = 19.6\ GeV$, the output from our blast wave $\langle p_t \rangle$ (Figure 2.7) fits very well and $v_2\{4\}$ (Figure 2.8) likewise except for the most central point, $N_{part} \approx 290$. For energy $\sqrt{s} = 27\ GeV$, $\langle p_t \rangle$ (Figure(2.9)) fits perfect with the experimental data from STAR and $v_2\{4\}$ (Figure 2.10) fits rather well as well, except for the most periphery point, $N_{part} \approx 23$. For $\sqrt{s} = 39\ GeV$, we can also observe that the black solid line from the blast wave model fits the STAR data exceptionally well for both $\langle p_t \rangle$ (Figure 2.11) and $v_2\{4\}$ (Figure 2.12), except for the most peripheral point on $v_2\{4\}$ plot. With energy $\sqrt{s} = 62.4\ GeV$, $\langle p_t \rangle$ (Figure 2.13) from blast wave matches well with the experimental data from STAR, and $v_2\{4\}$ (Figure 2.14) fits relatively well with the experimental data from STAR, except for the most peripheral point. When we look at the data from STAR at $\sqrt{s} = 200\ GeV$, we can see that both $\langle p_t \rangle$ (Figure 2.15) and $v_2\{4\}$ (Figure 2.16) from the blast wave fit exceptionally well with the experimental data. Alternatively, with some variance between the output from the blast wave and the experimental data, the energy of $\sqrt{s} = 2760\ GeV$ from ALICE matches pretty well for both $\langle p_t \rangle$ (Figure 2.17) and $v_2\{4\}$ (Figure 2.18).

As we can see, the blast wave performs admirably for the seven various energies tested, and it is sufficiently accurate to be used for the calculation of the values of the four observables in Chapter 7 at the point of local equilibrium.

# CHAPTER 3 ONE-PARTICLE DISTRIBUTION

Several factors influence the properties of many-body systems, including particle interaction and constraints. Both the system's macroscopic state variables, such as particle density and temperature, as well as the system's particular microscopic features, are discussed in this section. The next step is to make an attempt to comprehend some of the equilibrium and non-equilibrium characteristics of the macroscopic system. In kinetic theory, this is accomplished by the use of a statistical description based on the 'one-particle distribution function' and the corresponding transport equation. Using the transport equation and conservation laws, it is possible to construct a hydrodynamic theory of an ideal fluid.

With kinetic equation, often known as relativistic Boltzmann, we may describe the progression of a thermodynamic system toward equilibrium. Which is caused by a mix of diffusion and scattering mechanisms, as well as any external forces acting on the system. There are several applications in a wide range of disciplines, including particle transport in plasmas and superfluids, as well as radiative transfer in planetary atmospheres. Because no assumption is made about the initial state being in local equilibrium, this is also one of the few methodologies available for investigating the non-equilibrium features of ion collisions.[19, 33, 34, 35, 36, 37, 38].

The entire Boltzmann equation, which is a nonlinear integro-differential equation, may be extremely difficult to solve, even numerically, because of its nonlinear nature. The assumptions we make about the sorts of solutions that are available, as well as the effect collisions have on the system, allow us to overcome this problem. When developing these assumptions, care must be given to ensure that they do not violate desired system features, particularly the conservation laws. Even though many of the assumptions we make are conventional when working with the Boltzmann equation, we present a unique method of enforcing the conservation rules. Furthermore, while these approximation approaches may not represent a developing system with as much information as is necessary as the full equation, it is permitted for the discovery of accurate solutions as well as the provision of physical insight into the processes that are taking place.

## 3.1 Relativistic kinetic equation

A macroscopic system is characterized in kinetic theory by the one-body distribution function $f(\mathbf{x}, \mathbf{p}, t)$. The distribution function's space–time evolution is given by the kinetic or transport equation. The Boltzmann equation was the first to be developed by Boltzmann [1]. The relativistic version of the Boltzmann equation without and with collisions respectively can be written as,

$$\partial_t f(\mathbf{x}, \mathbf{p}, t) + \mathbf{v_p} \cdot \nabla f(\mathbf{x}, \mathbf{p}, t) = 0 \tag{3.1}$$

$$\partial_t f(\mathbf{x}, \mathbf{p}, t) + \mathbf{v_p} \cdot \nabla f(\mathbf{x}, \mathbf{p}, t) = I\left\{f\right\} \tag{3.2}$$

Where $\mathbf{v_p} = \frac{\mathbf{p}}{\mathbf{p^0}} = \frac{\mathbf{p}}{E}$ is the three-velocity of a single particle. The system's free streaming (collision-free) development is described by equation (3.1) and the systems with streaming (collisions) development is described by equation (3.2).

If the particles collide, the net flow will not be zero. In a tiny volume element $\delta^4\mathbf{x}$, the change in the number of particles for given momentum range between $\mathbf{p}$ and $\mathbf{p} + \delta\mathbf{p}$ is represented as

$$\delta^4 x \frac{\delta^3 p}{E} I\left\{f\right\} \tag{3.3}$$

$I\left\{f\right\}$ is an invariant function in the momentum-position space whose form must be solved. To compute $I\left\{f\right\}$, Boltzmann assumes the following assumptions.

- Only two-particle collisions need to be examined since the system is dilute enough.
- Instantaneous collisions occur.
- In space–time, the distribution function $f(\mathbf{x}, \mathbf{p}, t)$ fluctuates slowly.
- The colliding particles momenta are uncorrelated and position-independent. The ″Stosszahlansatz″ (collision number hypothesis) or the ″molecular chaos″ hypothesis is a major Boltzmann assumption.

From the assumptions above, collisions between two particles are the only ones that matter. Consider a collision Figure 3.1, where two particles with starting momenta $p_1^\mu$

---

[1] Ludwig Eduard Boltzmann was an Austrian scientist who lived from 1844 to 1906. In statistical thermodynamics, he made significant contributions. He was an early supporter of atomic theory, long before it became popular. His works were not well received throughout his lifetime. Boltzmann became devastated as a result of the rejection of his ideas, and he committed suicide in 1906.

and $p_2^\mu$ collide to produce a final state $p_3^\mu$ and $p_4^\mu$. In four-volume $\delta^4\mathbf{x}$, this form of collision reduces the number of particles in the momentum range $p^\mu + \delta p^\mu$. The average number of particle loss, $\Delta N_L$, of such collisions, according to the molecular chaos hypothesis, is proportional to:

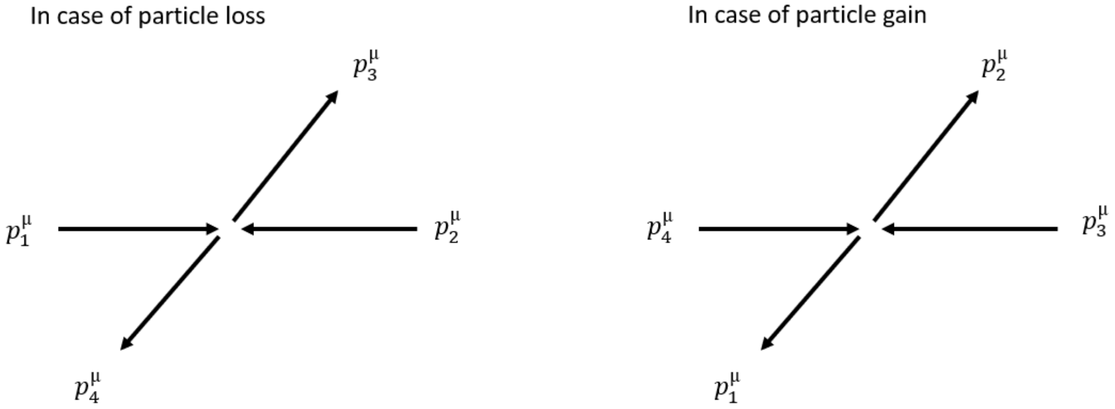

Figure 3.1: Schematic diagram includes two phases of the two-particle collision. Left phase in case of particle lost, $\Delta N_L$, caused by collision; the right phase in case of particle gained, $\Delta N_G$, caused by collision.

$$\begin{aligned}\Delta N_L &\propto \delta^3\mathbf{p_2}\delta^3\mathbf{p_3}\delta^3\mathbf{p_4}\delta^4\mathbf{x}f(\mathbf{x},\mathbf{p_1},t)\delta^3\mathbf{p_1}f(\mathbf{x},\mathbf{p_2},t)\\ &= \delta^3\mathbf{p_2}\delta^3\mathbf{p_3}\delta^3\mathbf{p_4}\delta^4\mathbf{x}W_{12\to34}f(\mathbf{x},\mathbf{p_1},t)\delta^3\mathbf{p_1}f(\mathbf{x},\mathbf{p_2},t). \qquad (3.4)\end{aligned}$$

Where $W_{12\to34}$ is the scattering rate and $f(\mathbf{x},\mathbf{p_i},t)\delta^3\mathbf{p_i}$ is the average number of particles per unit volume between $\mathbf{p_i}$ and $\mathbf{p_i}+\delta\mathbf{p_i}$ with three-momentum.

The average number of particles lost via collisions in the range $\delta^4\mathbf{x}$ of Minkowski-space and with momentum in the range of $\mathbf{p}$ and $\mathbf{p}+\mathrm{d}\mathbf{p}$ is then derived by integrating the above stated number of collisions,

$$N_L = \delta^4 x\frac{\delta^3 p_1}{E_1}\int \mathrm{d}\mathbf{p_2}\mathrm{d}\mathbf{p_3}\mathrm{d}\mathbf{p_4}f(\mathbf{x},\mathbf{p_1},t)f(\mathbf{x},\mathbf{p_2},t)\times W_{12\to34} \qquad (3.5)$$

Similarly, the gain term can be computed,

$$N_G = \delta^4 x\frac{\delta^3 p_1}{E_1}\int \mathrm{d}\mathbf{p_2}\mathrm{d}\mathbf{p_3}\mathrm{d}\mathbf{p_4}f(\mathbf{x},\mathbf{p_3},t)f(\mathbf{x},\mathbf{p_4},t)\times W_{34\to12} \qquad (3.6)$$

Equation (3.3) is equated to the difference between $N_G$ and $N_L$ in the interval $\delta^4\mathbf{x}$ and $\delta^3\mathbf{p}$. Then $I\{f\}$ has the following form,

$$I\{f\} = \int \mathrm{d}\mathbf{p_2}\mathrm{d}\mathbf{p_3}\mathrm{d}\mathbf{p_4}\left[f(\mathbf{x},\mathbf{p_3},t)f(\mathbf{x},\mathbf{p_4},t)\times W_{34\to12} - f(\mathbf{x},\mathbf{p_1},t)f(\mathbf{x},\mathbf{p_2},t)\times W_{12\to34}\right] \tag{3.7}$$

Thus the collision transport equation may be written as,

$$I\{f\} = \int \mathrm{d}\mathbf{p_2}\mathrm{d}\mathbf{p_3}\mathrm{d}\mathbf{p_4}\left[f_3 f_4 \times W_{34\to12} - f_1 f_2 \times W_{12\to34}\right]. \tag{3.8}$$

Where $f_i = f(\mathbf{x},\mathbf{p_i},t)$ and $\mathrm{d}\mathbf{p} = \frac{\mathrm{d}^3p}{(2\pi)^3}$. The scattering rate in the above equation is a scalar and its detailed balance to each other ($W_{12\to34} = W_{34\to12}$) that may be written in terms of any two of the three Mandelstam variables specified in chapter 2. The collision term can be written as,

$$I\{f\} = \int \mathrm{d}\mathbf{p_2}\mathrm{d}\mathbf{p_3}\mathrm{d}\mathbf{p_4}\left[f_3 f_4' - f_1 f_2\right] W_{12\to34}. \tag{3.9}$$

Where the scattering rate is proportion to $\delta(p_1^\mu + p_2^\mu - p_3^\mu - p_4^\mu)$. To more precisely express correlations, the products $f_i f_j$ might be replaced by two-particle distributions. Later on, we will use Langevin noise to introduce correlations.

### 3.2 Distribution function at equilibrium

The Boltzmann equation defines the space–time development of a macroscopic system's distribution function. One of the main assumptions for a macroscopic system is that it will approach equilibrium if left without any disturbance or any external forces applied to the system. Where the instantaneous variation of the distribution function with respect to time is equal to zero. It's important to know the difference between global and local equilibrium. The entire system may be split into multiple small macroscopic subsystems as shown in Figure 3.2. All cells in global equilibrium may be described by the same thermodynamic variables, such that thermodynamic variables are independent of positions. While, in local equilibrium, thermodynamic variables are a function of the cell's spatial location. Assuming the cell is in local thermal equilibrium, we can provide a temperature of $T$ and a chemical potential of $\mu(\mathbf{x})$ for each particle species at each space–time point, $\mathbf{x}$, in addition to the velocity, $\mathbf{v}(\mathbf{x})$. The equilibrium distribution function may be calculated using kinetic theory if and only if the variation in the entropy four-flow is equal to zero $''\partial_\mu S^\mu = 0''$.

The Boltzmann entropy four-flow can be written as,

$$S^\mu = -\int \frac{\mathrm{d}^3p}{E} p^\mu f \left[\ln f - 1\right], \tag{3.10}$$

so the variation in the entropy four-flow can be written as,

$$\partial_\mu S^\mu = -\int \frac{\mathrm{d}^3p}{E} p^\mu \left[\ln f\right] I\left\{f\right\}, \tag{3.11}$$

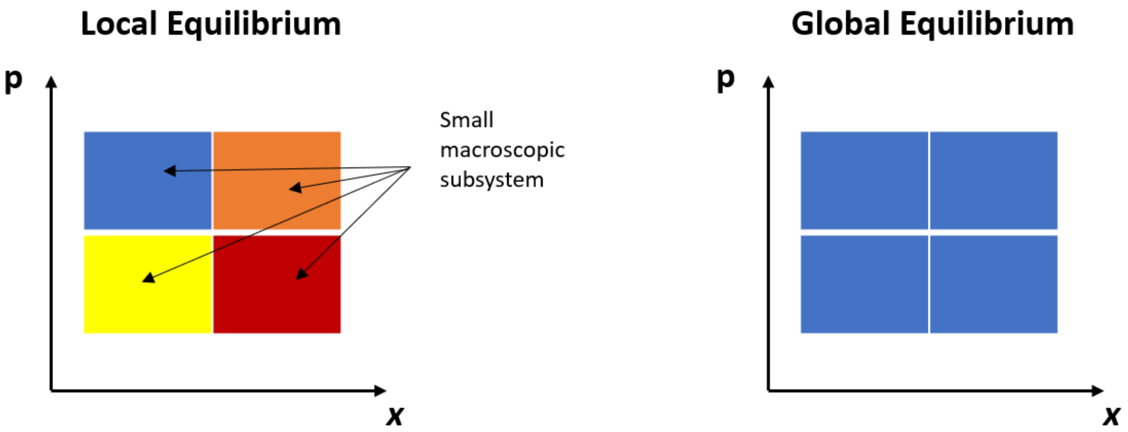

Figure 3.2: This schematic figure shows a simple explanation of the difference between local and global equilibrium. For local equilibrium, only the macroscopic subsystem ″cells with different colors″ reaches the equilibrium, while for global equilibrium all the cells have the same color and independent of space.

where $I\left\{f\right\} = p^\mu \partial_\mu f$. The collision term is identically zero when,

$$f_1 f_2 - f_3 f_4 = 0 \tag{3.12}$$

The requirement for maximizing entropy four-flow is thus in the above equation. The equilibrium distribution function denoted by $f^e$, the above equation can be written as,

$$\ln f_1^e + \ln f_2^e = \ln f_3^e + \ln f_4^e \tag{3.13}$$

During collision, energy and momentum are conserved

$$E_1 + E_2 = E_3 + E_4 \tag{3.14}$$

$$\mathbf{p_1} + \mathbf{p_2} = \mathbf{p_3} + \mathbf{p_4} \tag{3.15}$$

$\ln f_i^e(\mathbf{x}, \mathbf{p})$ is known as the summational invariant. The most general form of a $\ln f_i^e(\mathbf{x}, \mathbf{p})$ is a linear combination between a constant and $p^\mu$,

$$\ln f^e(\mathbf{x}, \mathbf{p}) = A(\mathbf{x}) + B_\mu(\mathbf{x}) p^\mu \tag{3.16}$$

The local equilibrium distribution function can be expressed as follows:

$$f^e(\mathbf{x}, \mathbf{p}) = e^{A(\mathbf{x}) + B_\mu(\mathbf{x}) p^\mu} \tag{3.17}$$

Both the parameters $A$ and $B$ remain constant when rigid rotation is ignored, and the equilibrium distribution function may be expressed as,

$$f^e = e^{A + B_\mu p^\mu} \tag{3.18}$$

where $A = \gamma(\mu/T)$ and $B_\mu = -\gamma(u_\mu/T)$. The local equilibrium distribution, which takes the form (assuming Boltzmann statistics):

$$f^e = e^{-\gamma(E - \mathbf{p}.\mathbf{v} - \mu)/T}. \tag{3.19}$$

Where $\gamma = \frac{1}{\sqrt{1-v^2}}$ is the corresponding Lorentz factor. Fluid velocity $\mathbf{v}$, chemical potential $\mu$ and temperature $T$ vary in space and time.

### 3.3 Conservation Laws

If we multiply equation (3.16) by the collision term, $I\{f\}$, and then integrate all over the momentum space, we will get an important equations.

$$\int \frac{d\mathbf{p}}{E} A(\mathbf{x}) I\{f\} + \int \frac{d\mathbf{p}}{E} B_\mu(\mathbf{x}) p^\mu I\{f\} = 0 \tag{3.20}$$

The preceding equation can be expressed as follows:

$$\int \frac{d\mathbf{p}}{E} A(\mathbf{x}) p^\mu \partial_\mu f + \int \frac{d\mathbf{p}}{E} B_\mu(\mathbf{x}) p^\mu p^\nu \partial_\nu f = 0 \tag{3.21}$$

The first part of the above equation gives the total particle number's macroscopic conservation law and the second part gives the momentum-energy conservation. The five equations, for a system with a single conserved charge, are

$$\partial_\mu N^\mu = 0 \quad \& \quad \partial_\mu T^{\mu\nu} = 0. \tag{3.22}$$

Where $T^{\mu\nu}$ is a momentum-energy tensor. We notice that from the above five equations the scattering rate $W_{12\to34}$ enforces conservation laws. But in this thesis, we will use the relaxation time approximation to simplify our calculations. In this approach, the collision term is estimated as,

$$I\{f\} \approx -\nu(f - f^e), \tag{3.23}$$

Where, in a frame when the fluid is locally at rest, the relaxation time $\nu^{-1}$ indicates how long it takes for a pair of particles to collide or we can define it as the mean free time collisions between parton. The Boltzmann equation (3.2) is written in its covariant form as,

$$p^\mu \partial_\mu f = -\nu p.u(f - f^e), \tag{3.24}$$

We'll utilize the method of characteristics to solve equation (3.24), which is often employed to solve the non-relativistic Boltzmann equation [39]. To begin, we simplify the equation by inserting a proper time parameter $\tau$, which is defined as follows:

$$\frac{dx^\mu}{d\tau} = \frac{p^\mu}{p\ .\ u} \tag{3.25}$$

Because $p\ .\ u = E$ in the rest frame of the fluid, the time component of equation (3.25) is simply written as $dt/d\tau = E/p\ .\ u = 1$ in this frame. This means that $\tau$ is the proper time in this rest frame. The Boltzmann equation can be written as,

$$\frac{df}{d\tau} = -\nu(f - f^e) \tag{3.26}$$

We can discover solutions for $f$ when the Boltzmann equation is reduced to a first-order equation ODE [39]. In order to solve equation (3.26), we first analyze the free streaming situation with no collisions, by means we set the right side of (3.26) to zero. According to equation (3.25), matter in a cell that starts at $\mathbf{x_0}$ floats along the trajectory $\mathbf{x} = \mathbf{x_0} + \mathbf{v_p}t$ unaffected. From equation ( 3.26) the free streaming relation can be written as,

$$f(\mathbf{p}, \mathbf{x}, \tau) = f_0(\mathbf{p}, \mathbf{x} - \mathbf{v_p}t). \tag{3.27}$$

Where $f_0(\mathbf{p}, \mathbf{x})$ is the initial distribution function. As we can see equation (3.27) is the solution of equation (3.1).

We write (3.26) as the integral equation in the presence of both collisions and drift.

$$f = f_0(\mathbf{p}, \mathbf{x} - \mathbf{v_p}t)S(\tau, \tau_0) + \int_{\tau_0}^{\tau} d\tau' \nu(\tau')S(\tau, \tau')f^e(\mathbf{p}, \mathbf{x} - \mathbf{v_p}t'). \tag{3.28}$$

The survival probability is defined as,

$$S(\tau, \tau_0) = \exp\{-\int_{\tau_0}^{\tau} \nu(\tau')d\tau'\} \tag{3.29}$$

This means the probability that partons will not collide while traveling along their typical path [40]. $t = t(\tau)$ and $t' = t(\tau')$ are calculated using equation (3.25). In reality, computing (3.28) can be challenging because we must determine temperature, velocity, and chemical potential as a function of time by applying nonlinear restrictions. It's worth noting that Baym used a different approach to this single-particle distribution problem yet came up with similar conclusions [19]. Equation (3.28), in particular, corresponds to Baym's equation (17).

### 3.4 Linearization of Boltzmann equation

If the problem cannot be solved exactly, but can be described by adding a "very small" term, $h << 1$, to the mathematical description of the perfectly solvable problem, perturbation theory is applicable in this situation. Although the formulas generated by perturbation theory can lead to correct findings if the expansion parameter is very small. Typically, in this case the distribution function due to very small perturbation can be written as

$$f_i \approx f_i^e(1 + h_i) \tag{3.30}$$

$$f_j \approx f_j^e(1 + h_j) \tag{3.31}$$

Where index $i = 1, 2$ and $j = 3, 4$. We will write the collision term equation (3.9) interms of the small perturbation $h$,

$$\begin{aligned} f_i f_j &\approx f_i^e f_j^e(1 + h_i)(1 + h_j) \\ &= f_i^e f_j^e(1 + h_i + h_j + h_i h_j). \end{aligned}$$

We can neglect the terms $h_i h_j$ and use the equilibrium distribution expression from Equation (3.12) to rewrite Equation (3.9) in the form of

$$I\left\{f\right\} = \int d\mathbf{p_2} d\mathbf{p_3} d\mathbf{p_4} W_{12\to 34} f_1^e f_2^e (h_3 + h_4 - h_1, -h_2) \equiv Lh, \tag{3.32}$$

Where $L$ is a linear operator on $h$. Take a look at the eigenvectors of this operator that satisfy $L\phi_\alpha = -\nu_\alpha \phi_\alpha$. The eigenvalues of the first five eigenvectors are zero and they are linear in the conserved variables $1, \mathbf{p}$, and $E$. Combinations that are linear,

$$\phi_1 = 1 \tag{3.33}$$

$$\phi_2 = \sqrt{\frac{n}{\omega T}} p_x; \qquad \phi_3 = \sqrt{\frac{n}{\omega T}} p_y; \qquad \phi_4 = \sqrt{\frac{n}{\omega T}} p_z \tag{3.34}$$

$$\phi_5 = \sqrt{\frac{n}{c_v T}} \left(E - \frac{e}{n}\right). \tag{3.35}$$

Where $n$ represents particle density, $\omega$ represents enthalpy density, $e$ represents energy density, and $c_v$ represents specific heat. Because of the conservation principles, these eigenvectors have eigenvalue zero and are linear. On the other hand, each eigenvector is orthogonal to the other and the orthonormal sense can be written as,

$$\langle \phi_\alpha | \, f^e \, | \phi_\beta \rangle = \int d\mathbf{p} f^e \phi_\alpha \phi_\beta = n\delta_{\alpha\beta} \tag{3.36}$$

We will use the above relation to check the orthogonality between $\phi_1$ and $\phi_3$ for example

$$\begin{aligned}
\langle \phi_1 | \, f^e \, | \phi_1 \rangle &= \int d\mathbf{p} f^e \, (1.1) \\
&= n \\
\langle \phi_1 | \, f^e \, | \phi_3 \rangle &= \int d\mathbf{p} f^e \left(1 . \sqrt{\frac{n}{\omega T}} p_y\right) \\
&= \sqrt{\frac{n}{\omega T}} \, \langle p_y \rangle = 0 \\
\langle \phi_3 | \, f^e \, | \phi_3 \rangle &= \int d\mathbf{p} f^e \left(\sqrt{\frac{n}{\omega T}} p_y . \sqrt{\frac{n}{\omega T}} p_y\right) \\
&= \frac{n}{\omega T} \langle p_y^2 \rangle = n.
\end{aligned}$$

Where the first projection follows from the conservation of the number of particles, while the second projection follows from the conservation of momentum, and the third projection can be calculated from equation (3.25) in the same way in [41].

The conservation conditions of the five equations for relaxation time approximation can be written as,

$$\int d\mathbf{p}\phi_\alpha f^e h = 0 \tag{3.37}$$

Where $\alpha$ varies between 0 and 5. As we can see from the above equation $\phi_\alpha$ is orthogonal to the perturbation $h$.

We assume that all the values relevant to the distribution function $f$ relax at the same time rate $\nu^{-1}$ in the relaxation time approximation. The relaxation of the modes is described by the eigenvalues of $L$. Generally, we may write $h$ as,

$$h(\mathbf{x}, \mathbf{p}, \tau) = \sum_{\beta>5} c_\beta(\mathbf{x})\phi_\beta(\mathbf{p}) \exp\left(-\nu_\beta \tau\right) \tag{3.38}$$

Because there is no assurance, a prior, that $f$ and $f^e$ will generate the same values – for example, particle number and energy density. Linearized Boltzmann's equation does not explicitly impose conservation constraints as well as the relaxation time approximation. To formally enforce these criteria, we express the collision term as,

$$I\left\{f\right\} \approx \frac{df}{d\tau} = -\nu(1-P)f. \tag{3.39}$$

Where $P$ is the projection operator that can be applied to a specific quantum state to project it into another state. The useful relations of the projection operator are shown in Table 3.1.

| Projection Operator Properties | |
|---|---|
| (1): Idempotent | $P^2 = P$ |
| (2): Hermitian | $P^\dagger = P$ |
| (3): Orthogonal | $P(1-P) = 0$ |
| (4): Idempotent | $(1-P)^2 = 1-P$ |
| (5): Enforce $f$ to $f^e$ | $Pf = f^e$ |
| (6): Commute | $P\frac{d}{d\tau} = \frac{d}{d\tau}P$ |

Table 3.1: Useful properties for projection operator to find the solution of the Boltzmann equation

Many situations in quantum mechanics that tells us where the usage of the projection operator is important. Example: when we measure the property of a quantum particle, quantum mechanics tells us that the state of the particle will collapse onto a different state. The projection operator allows us mathematically to describe this collapse. This means that we will prove the properties in Table 3.1 and how they involve across the linearization of the Boltzmann equation. We define the projection operator as,

$$P_\phi(\mathbf{p}) \equiv P = \frac{f^e(\mathbf{p})}{n} \sum_{\alpha=1}^{5} \phi_\alpha(\mathbf{p}) \int d\mathbf{p}' \phi_\alpha(\mathbf{p}') \equiv |\phi\rangle \langle\phi| \tag{3.40}$$

We consider the action of the operator on an arbitrary eigenfunction $|\psi\rangle$, where

$$P_\phi(\mathbf{p}) |\psi\rangle = |\phi\rangle \langle\phi| |\psi\rangle = c |\phi\rangle . \tag{3.41}$$

Where the bracket between $\langle\phi|$ and $|\psi\rangle$ is a scalar $c$,(if $\langle\phi|$ and $|\psi\rangle$ are not orthogonal to each other) we can move it to the front and we obtain $c|\phi\rangle$. As we can see from the above equation how the projection operator change the state from one to another, which is a good sense to show how the projection operator enforces the distribution function from $f$ to $f^e$.

We will prove the properties for the projection operator in Table 3.1.

Property (1):

$$\begin{aligned}
P^2 |\psi(\mathbf{p})\rangle &= P.P |\psi(\mathbf{p})\rangle \\
&= (|\phi\rangle \langle\phi|)(|\phi\rangle \langle\phi|) |\psi(\mathbf{p})\rangle \\
&= |\phi\rangle \langle\phi| |\phi\rangle \langle\phi| |\psi(\mathbf{p})\rangle \\
&= |\phi\rangle \langle\phi| |\psi(\mathbf{p})\rangle \\
&= P |\psi(\mathbf{p})\rangle \\
\therefore P^2 = P.
\end{aligned}$$

In the third line we used the orthonormality condition, $\langle\phi| |\phi\rangle = 1$. We will use below another way to prove the condition for property (1)

$$\begin{aligned}
P^2\psi(\mathbf{p}) &= \frac{f^e(\mathbf{p})}{n} \sum_{\alpha=1}^{5} \phi_\alpha(\mathbf{p}) \int d\mathbf{p}' \phi_\alpha(\mathbf{p}') \left( \frac{f^e(\mathbf{p}')}{n} \sum_{\beta=1}^{5} \phi_\beta(\mathbf{p}') \int d\mathbf{p}'' \phi_\beta(\mathbf{p}'') \psi(\mathbf{p}'') \right) \\
&= \frac{f^e(\mathbf{p})}{n} \sum_{\alpha=1}^{5} \phi_\alpha(\mathbf{p}) \left( \sum_{\beta=1}^{5} \int d\mathbf{p}' \phi_\alpha(\mathbf{p}') \frac{f^e(\mathbf{p}')}{n} \phi_\beta(\mathbf{p}') \right) \int d\mathbf{p}'' \phi_\beta(\mathbf{p}'') \psi(\mathbf{p}'')
\end{aligned}$$

$$\begin{aligned}
P^2\psi(\mathbf{p}) &= \frac{f^e(\mathbf{p})}{n}\sum_{\alpha=1}^{5}\phi_\alpha(\mathbf{p})\left(\sum_{\beta=1}^{5}\delta_{\alpha\beta}\right)\int d\mathbf{p}''\phi_\beta(\mathbf{p}'')\psi(\mathbf{p}'') \\
&= \frac{f^e(\mathbf{p})}{n}\sum_{\alpha=1}^{5}\phi_\alpha(\mathbf{p})\int d\mathbf{p}''\phi_\beta(\mathbf{p}'')\psi(\mathbf{p}'') \\
&= P\psi(\mathbf{p})
\end{aligned}$$

From the above result, we conclude that $P$ is a projection operator and we can use either way to prove any property from table 3.1.

Property (2):

$$\begin{aligned}
P^\dagger\psi(\mathbf{p}) &= \left(|\phi\rangle\langle\phi|\right)^\dagger\psi(\mathbf{p}) \\
&= |\phi\rangle\langle\phi|\,\psi(\mathbf{p}) \\
&= P\psi(\mathbf{p}) \\
\therefore P^\dagger &= P
\end{aligned}$$

We will use a very useful property of the projection operator, which allows us to write any eigenstate as the sum of two other eigenstates. One is parallel to the initial eigenstate and the other is perpendicular to it.

Property (3): Consider a

$$\begin{aligned}
|\psi\rangle &= \mathbb{1}\,|\psi\rangle \\
&= \mathbb{1}\,|\psi\rangle + P\,|\psi\rangle - P\,|\psi\rangle \\
&= P\,|\psi\rangle + (\mathbb{1} - P)\,|\psi\rangle
\end{aligned}$$

If the projection operator acts on the above eigenstate, then the above relation can be written as,

$$\begin{aligned}
P\,|\psi\rangle &= P^2\,|\psi\rangle + P\,(\mathbb{1} - P)\,|\psi\rangle \\
&= P\,|\psi\rangle + P\,(\mathbb{1} - P)\,|\psi\rangle \\
\therefore P\,(\mathbb{1} - P) &= 0
\end{aligned}$$

We used property (1) to move from the first to the second line, and we can notice from the second line the relation is true if and only if $P\,(\mathbb{1} - P) = 0$. On the other hand, for property (4) we can do same steps as property (3) but instead of applying $P$ on the eigenstate we can apply $(1-P)$ and we will end with $(1-P)^2 = (1-P)$.

Property (5): we will apply the projection operator on the linearization equation, $f - f^e \approx f^e h$, on a state $|\phi\rangle$. The equation can be written as,

$$
\begin{aligned}
P(f - f^e)\,|\phi\rangle &\approx Phf^e\,|\phi\rangle \\
Pf\,|\phi\rangle - Pf^e\,|\phi\rangle &\approx |\phi\rangle\,\langle\phi|\,hf^e\,|\phi\rangle\,.
\end{aligned}
$$

We can see the right side of the above equation compared to equation (3.37) is equal to zero, thus the above equation can be written as,

$$
\begin{aligned}
Pf\,|\phi\rangle &= |\phi\rangle\,\langle\phi|\,f^e\,|\phi\rangle \\
&= f^e\,|\phi\rangle\,\langle\phi|\,|\phi\rangle \\
&= f^e\,|\phi\rangle \\
\therefore Pf &= f^e.
\end{aligned}
$$

Where in the second line we used the orthonormal condition, $\langle\phi|\,|\phi\rangle = 1$, to get the final relation.

Property (6):

$$
P\frac{d}{d\tau}\psi(\mathbf{p}) = \frac{f^e(\mathbf{p})}{n}\sum_{\alpha=1}^{5}\phi_\alpha(\mathbf{p})\int d\mathbf{p}'\phi_\alpha(\mathbf{p}')\frac{d}{d\tau}\psi(\mathbf{p})
$$

As a result, there is no dependency on $\tau$ outside of $\psi(\mathbf{p})$ and we have

$$
\begin{aligned}
P\frac{d}{d\tau}\psi(\mathbf{p}) &= \frac{d}{d\tau}\frac{f^e(\mathbf{p})}{n}\sum_{\alpha=1}^{5}\phi_\alpha(\mathbf{p})\int d\mathbf{p}'\phi_\alpha(\mathbf{p}')\psi(\mathbf{p}) \\
&= \frac{d}{d\tau}P\psi(\mathbf{p}) \\
\therefore P\frac{d}{d\tau} &= \frac{d}{d\tau}P.
\end{aligned}
$$

Now the linearized Boltzmann equation is approximated as

$$
I\{t\} \approx \frac{df}{d\tau} = -\nu(1-P)f, \tag{3.42}
$$

Multiply equation (3.42) by $(1-P)$. On the left side, we use $d/d\tau$ to commute with $(1-P)$, whereas on the right side, we will use property (4) from table 3.1. We have discovered

$$f = f_0(\mathbf{x} - \mathbf{v_p}t, \mathbf{p})S(\tau, \tau_0) + f^e(\mathbf{x} - \mathbf{v_p}t, \mathbf{p})(1 - S(\tau, \tau_0)), \tag{3.43}$$

In the next chapter, we employ the linearized relaxation time approximation because it gives a straightforward explanation of transport that successfully integrates conservation laws. While it may not be as good at describing the early stages of pre-equilibrium development as the entire relaxation time method or the full equation of Boltzmann, none of these techniques is completely dependable at that point.

# CHAPTER 4 TWO-PARTICLE CORRELATION

The usual form of the Boltzmann equation does not provide a method for explaining correlations in the data. The molecular chaos ansatz, also known as the Stosszahlansatz, is based on the assumption that particles are uncorrelated before colliding. The fact that our entire ultimate objective is to characterize two-particle correlations, which are partially due to collisions, forces us to include a method to do this. Our approach is to incorporate Langevin noise into the Boltzmann equation, which is compatible with the conservation principles that are seen in microscopic scattering processes [42, 43, 44].

The background noise that we used in this thesis is based on the fact that we are looking at the level of the fluid cells Figure 3.2 (thus the relaxation time approximation), we assume that each fluid cell is out of equilibrium, resulting in a non-zero value for $f-f^e$. Viscosity is responsible for driving fluid cells toward equilibrium and also influences the behavior of nearby fluid cells, causing them to move toward a more global equilibrium. A large number of particles exist in each fluid cell and they interact collectively through viscous forces, but they also interact microscopically through collisions with one another. The microscopic interactions might cause a particle to be pushed toward or away from the equilibrium distribution of the fluid cell depending on the current density and temperature of the fluid cell. This is true for all of the particles in the system. This means that even if the fluid cell was in its equilibrium distribution, the microscopic interactions might cause the distribution to deviate from its equilibrium distribution. Noise can cause correlations between distinct cells and viscosity is always in a fight with noise, causing the cell to return to equilibrium.

As an introduction to this chapter, we will look at example an of Langevin noise applied to Brownian motion and particle number distribution problem. We will utilize this to illustrate the characteristics of stochastic noise that we will be discussing in this chapter, namely how we will use noise to build correlations into a system.

## 4.1 General product rule

We can no longer use the product rule of regular calculus since we now have new differentials in our toolbox which will be useful for small perturbation. We'll need a universal product rule that can handle two half-order differentials being multiplied together.

Given two functions $A_t$ and $B_t$, where both of them depend on $t$. We can write the product between $A_t$ and $B_t$ as,

$$A_tB_t = \frac{1}{2}((A_t + B_t)^2 - A_t^2 - B_t^2) \tag{4.1}$$

The above relation is true if and only if $A_t$ is commute with $B_t$.

In case of small perturbation when $(\Delta t \to 0)$, we can use Itô formula [1] to differentiate $A_t^2$ and $B_t^2$,

$$\Delta A_t^2 = 2A_t\Delta A_t + (\Delta A_t)^2 \tag{4.2}$$

$$\Delta B_t^2 = 2B_t\Delta B_t + (\Delta B_t)^2 \tag{4.3}$$

Equation (4.1) can be written in the differentiation form as,

$$\Delta A_tB_t = \frac{1}{2}(\Delta(A_t + B_t)^2 - \Delta A_t^2 - \Delta B_t^2) \tag{4.4}$$

From the above relation the first term on the right side can be written as,

$$\begin{aligned}\Delta(A_t + B_t)^2 &= 2(A_t + B_t)\Delta(A_t + B_t) + (\Delta(A_t + B_t))^2\\ \Delta(A_t + B_t)^2 &= 2(A_t\Delta A_t + A_t\Delta B_t + B_t\Delta B_t + B_t\Delta A_t)\\ &\quad + (\Delta A_t)^2 + 2\Delta A_t\Delta B_t + (\Delta B_t)^2.\end{aligned} \tag{4.5}$$

Now substitute equation (4.2), (4.3) and (4.5) in equation (4.1). Final equation can be written as,

$$\Delta(A_tB_t) = A_t\Delta B_t + B_t\Delta A_t + \Delta A_t\Delta B_t \tag{4.6}$$

In stochastic calculus, this equation is referred to as the Itô product rule. We will use this rule to find the product of the linearized Boltzmann equation at two phase space points in the correlation section.

---

[1] Its formula is equivalent to the Newton-Leibnitz formula in (classical) calculus for stochastic calculus. It not only connects differentiation and integration, but it also offers a way for computing stochastic integrals.The differentiation of $f(X_t)$ can be written as: $\Delta f(X_t) = f'(X_t)\Delta X_t + \frac{1}{2}f''(X_t)(\Delta X^2) + o(\Delta t)$

### 4.2 Langevin's Theory

For systems that aren't in equilibrium, Brownian motion is probably the easiest way to deal with their dynamics. The Langevin equation is the most important. Frictional and random forces are included in this category. The fluctuation-dissipation theorem shows that these two forces of nature are linked together. There are a lot of important and far-reaching generalizations in this theorem. If we want to start out, we'll look at a very simple version of the theorem for now.

Brownian motion is the random movement of a very small particle submerged in a fluid. Early examinations of this phenomenon were conducted on pollen grains, particles from dust, and a variety of other materials with a colloidal size of less than one micron. As time progressed, it became obvious that the idea of Brownian motion could be successfully applied to a wide range of other phenomena.

The idea of Brownian motion, in particular, has been extended to scenarios in which the ′Brownian particle′ would not be a real particle, but rather some collective attribute of a macroscopic system. This might be the concentration of any component in a chemically reacting system at thermal equilibrium for example. In this case, the uneven temporal fluctuation of this concentration correlates to the erratic motion of the dust particle.

Although the motion of a particle executing Brownian motion appears to be completely random, it must still be described by the same equations of motion as any other dynamical system. Newton's equations is the one that is used in classical mechanics or we can use Hamiltonian's equations

Newtons law for a spherical particle in one dimension can be written as,

$$m\dot{v} = F_{tot}(t), \tag{4.7}$$

It is typically not practical to try to get a precise formula for $F_{tot}$, unless it is absolutely necessary. Experience has shown us that in most circumstances the frictional force $-\alpha v$, which is proportional to the velocity of the particle (Brownian particle), dominates this force. Stokes' law, which states that friction coefficient $\alpha = 6\pi\eta r$, is used to calculate friction force. According to this scenario, the Brownian particle's equation of motion is as follows.

$$m\frac{dv}{dt} \approx -\alpha v, \tag{4.8}$$

the solution of the above linear first order equation is

$$v(t) = v(0)e^{-\alpha t/m}, \tag{4.9}$$

If this is the case, it is expected that the Brownian particle's speed will slow down to reach zero over a long time. At thermal equilibrium $\langle v^2 \rangle_{eq} = T/m$, which means that the particle's real speed must be greater than zero. In this case, we can notice that the assumption $F_{tot}$ is dominated by the friction must be changed.

In order to account for inertia, the model of Brownian motion is based on the following expression of Newton's law:

$$m\dot{v} = F_{external} - \alpha v + F, \tag{4.10}$$

Where the drag force term is represented by the function $\alpha v$ , and $F$ is the stochastic force generated by collisions between microscopic atoms [45], which accounts for random collisions with molecules. In the case of $F_{external} = 0$ the above equation can be written as,

$$\dot{v} = -\gamma v + \frac{F}{m}, \tag{4.11}$$

From the above equation,$\gamma = \alpha/m$ this may be used as a measure of time needed for drag to completely eliminate acceleration.

When a function is plotted against a variable, the definition of derivative is the rate at which the function changes. Differential equations issues are solved by the use of derivatives, which are fundamental concepts in mathematics. For the most part, we observe changing systems (dynamical systems) to determine the rate at which a particular variable changes. Equation (4.11) will be written as a difference equation when $\Delta t \to 0$

$$\Delta v \equiv v(t + \Delta t) - v(t) = -\gamma v \Delta t + \frac{F}{m}\Delta t, \tag{4.12}$$

From now on we will use $\Delta W$ instead of $\frac{F}{m}\Delta t$, where $\Delta W$ denotes the net change in velocity caused by collisions in the time between $t$ and $t + \Delta t$.

According to the more usually given viewpoint, the fluctuating force is thought to be caused by the Brownian particle colliding with molecules in the surrounding medium on an irregular basis. When a collision occurs, the force is expected to change rapidly throughout the course of any observation, and indeed over the course of any microscopic time period. This is not true in any real-world system, and it cannot be. The consequences of the fluctuating force may be described that the impact of a collision does not depend on the previous collisions in terms of its direction or magnitude, because of this

$$\langle \Delta W \rangle = 0 \tag{4.13}$$

$$\left\langle \Delta W^2 \right\rangle = \Gamma \Delta t \tag{4.14}$$

In equation (4.14), $\Gamma$ is defined as the strength of the fluctuating force.

In homogeneous linear first-order differential equations such as the Langevin equation (4.12) can be solved as,

$$v(t) = v_0 e^{-\gamma t} + \frac{1}{m} \int dt_1 F(t_1) e^{-\gamma(t_0 - t_1)}, \tag{4.15}$$

In case of finding the average of the above equation, the second term will vanish according to relation (4.13). Then $\langle v(t) \rangle = v_0 e^{-\gamma t}$. It is necessary to compute the average velocity square to determine the strength of the fluctuating force.

$$\begin{aligned} \left\langle v^2(t) \right\rangle &= v_0^2 e^{-2\gamma t} + \frac{2v_0 e^{-\gamma t}}{m} \int dt_1 F(t_1) e^{-\gamma(t_0 - t_1)} + \frac{1}{m^2} \int dt_1 F^2(t_1) e^{-2\gamma(t_0 - t_1)} \\ &= v_0^2 e^{-2\gamma t} + 0 + \Gamma \int dt e^{-2\gamma t} \end{aligned}$$

$$\therefore \left\langle v^2(t) \right\rangle = (v_0^2 - \frac{\Gamma}{2\gamma}) e^{-2\gamma t} + \frac{\Gamma}{2\gamma}. \tag{4.16}$$

The above equation approaches $\Gamma/2\gamma$ in the long-term limit when the exponential term is vanished. Mean squared velocity must reach equilibrium at $(T/m)$ in the long term. As a result, we discover

$$\Gamma = \frac{2\gamma T}{m}, \tag{4.17}$$

The above result is the Fluctuation-dissipation theorem. It connects the quantity of friction or dissipation to the strength $\Gamma$. It describes the equilibrium between friction and noise. Friction always tries to drive any system to a $''$ *dead* $''$ state while noise tends to keep the system ″ *alive* ″. This equilibrium is essential in order to maintain a thermal equilibrium condition for a long period of time.

Finally, the idea of Brownian motion serves as the foundation for our approach to kinetic theory, which allows us to include fluctuations [46, 47]. A model of Brownian motion (sometimes referred to as ″Physical″ Brownian motion) was published by Langevin after Einstein's theory was discovered. Because of its inertia, Langevin's model highlights that a particle traveling as a result of random collisions with other particles, such as gas molecules, does not truly experience separate steps, but rather continues in the same path as it did before.

### 4.3 New relativistic transport equation

Scattering creates random fluctuations in the phase space distribution in conjunction with the relaxation process outlined in Equation (3.9) and Equation (3.23). Correlations emerge in addition to those that existed in the original conditions as a result of these oscillations. It is inadequate to characterize these correlations using the Boltzmann equation since the premise of molecular chaos requires that particles uncorrelated before colliding with each other, which is not the case in reality. We will use a Langevin model to characterize these new correlations in this part, similar to how we described them in the previous section. We use these relationships to describe them as,

$$C(\mathbf{x_1}, \mathbf{p_1}, \mathbf{x_2}, \mathbf{p_2}, t) = \langle f(\mathbf{x_1}, \mathbf{p_1}, t) f(\mathbf{x_2}, \mathbf{p_2}, t) \rangle - \langle f(\mathbf{x_1}, \mathbf{p_1}, t) \rangle \langle f(\mathbf{x_2}, \mathbf{p_2}, t) \rangle \tag{4.18}$$

We shall rephrase the preceding equation in the simplest possible manner.

$$C_{1\leftrightarrow 2} = \langle f_1 f_2 \rangle - \langle f_1 \rangle \langle f_2 \rangle \tag{4.19}$$

Where $C_{1\leftrightarrow 2} \equiv C(\mathbf{x_1}, \mathbf{p_1}, \mathbf{x_2}, \mathbf{p_2}, t)$ and $f_i = f(\mathbf{x_i}, \mathbf{p_i}, t)$.

For the Boltzmann equation, we break phase-space into very small cells so that Langevin noise can be added to the equation. When particles in these cells collide, they randomly give each other momentum. This causes the phase space distribution to change. To better understand this process, we will introduce noise into equation (3.42) for each distribution function

$$\frac{df_1}{d\tau} = -\nu(1 - P_1)f_1 + \zeta_1 \tag{4.20}$$

$$\frac{df_2}{d\tau} = -\nu(1 - P_2)f_2 + \zeta_2 \tag{4.21}$$

Where $\zeta_{i=1,2}$ is the stochastic noise, $P_1$ and $P_2$ are the projection operators acts on particle 1 and particle 2 respectively. The above equations can be written as a difference equation when $\tau \to 0$,

$$\Delta f_1 \equiv f_1(\tau + \Delta\tau) - f_1(\tau) = -\nu(1 - P_1)f_1\Delta\tau + \Delta W_1 \tag{4.22}$$

$$\Delta f_2 \equiv f_2(\tau + \Delta\tau) - f_2(\tau) = -\nu(1 - P_2)f_2\Delta\tau + \Delta W_2 \tag{4.23}$$

Where $\Delta W_i \equiv \Delta W(\mathbf{x}_i, \mathbf{p}_i)$ is the stochastic increment to $f_i$ at point $(\mathbf{x}_i, \mathbf{p}_i)$ in the time between $\tau$ and $\tau + \Delta\tau$. As in Langevin's theory section, we can write the averaging increments as,

$$0 = \langle \Delta W_1 \rangle = \langle \Delta W_2 \rangle \tag{4.24}$$

$$\langle \Delta W_1 \Delta W_2 \rangle = \Gamma_{1\leftrightarrow 2}\Delta\tau \tag{4.25}$$

In case to find the differential equation for a two body system, $C_{1\leftrightarrow 2}$, we will take the average for equations (4.22) and (4.23)

$$\Delta \langle f_1 \rangle = -\nu(1 - P_1) \langle f_1 \rangle \Delta\tau \tag{4.26}$$

$$\Delta \langle f_2 \rangle = -\nu(1 - P_2) \langle f_2 \rangle \Delta\tau \tag{4.27}$$

We will find the average between $f_1\Delta f_2$, $f_2\Delta f_1$ and $\Delta f_1\Delta f_2$.

For $\langle f_1\Delta f_2 \rangle$:

$$\begin{aligned} \langle f_1\Delta f_2 \rangle &= \langle -f_1 \left[\nu(1 - P_2)f_2\Delta\tau + \Delta W_2\right] \rangle \\ &= -\nu(1 - P_2) \langle f_1 f_2 \rangle \Delta\tau \end{aligned}$$

For $\langle f_2\Delta f_1 \rangle$:

$$\langle f_2\Delta f_1 \rangle = -\nu(1 - P_1) \langle f_1 f_2 \rangle \Delta\tau$$

For $\langle \Delta f_2 \Delta f_1 \rangle$:

$$\begin{aligned}\langle \Delta f_1 \Delta f_2 \rangle &= \langle [-\nu(1-P_1) f_1 \Delta\tau + \Delta W_1]\,[-\nu(1-P_2) f_2 \Delta\tau + \Delta W_2] \rangle \\ &= \langle \Delta W_1 \Delta W_2 \rangle \\ &= \Gamma_{1\leftrightarrow 2} \Delta\tau\end{aligned}$$

We can observe from the previous equations that $\langle \Delta W_i \rangle = 0$. Moreover, we neglect the term that proportion to $\Delta\tau^2$, since its very small compared to $\Delta\tau$.

Differentiate $C_{1\leftrightarrow 2}$ with respect to $\tau$, then write it in a difference form when $\tau \to 0$

$$\begin{aligned}\frac{\Delta C_{1\leftrightarrow 2}}{\Delta\tau} &= \frac{\Delta \langle f_1 f_2 \rangle}{\Delta\tau} - \frac{\Delta(\langle f_1 \rangle \langle f_2 \rangle)}{\Delta\tau} \\ &= \frac{\langle f_1 \Delta f_2 \rangle + \langle f_2 \Delta f_1 \rangle + \langle \Delta f_2 \Delta f_1 \rangle}{\Delta\tau} - \frac{\langle f_1 \rangle \langle \Delta f_2 \rangle + \langle f_2 \rangle \langle \Delta f_1 \rangle + \langle \Delta f_2 \rangle \langle \Delta f_1 \rangle}{\Delta\tau} \\ &= \frac{[-\nu(1-P_2) - \nu(1-P_1)][\langle f_1 f_2 \rangle - \langle f_1 \rangle \langle f_2 \rangle]\Delta\tau + \Gamma_{1\leftrightarrow 2}\Delta\tau}{\Delta\tau}\end{aligned}$$

Rearrange and write the above equation in differential form to get,

$$\left(\frac{d}{d\tau} + \nu(1-P_2) + \nu(1-P_1)\right) C_{1\leftrightarrow 2} = \Gamma_{1\leftrightarrow 2} \tag{4.28}$$

It's possible that the particles described by $f_1$ and $f_2$ are the same, which would be a misinterpretation. We don't use this option since we want to describe distinct particle pairs. We will write the new form as,

$$G(\mathbf{x}_1, \mathbf{p}_1, \mathbf{x}_2, \mathbf{p}_2, t) \equiv G_{1\leftrightarrow 2} = C_{1\leftrightarrow 2} - \langle f_1 \rangle \delta(\mathbf{p}_1 - \mathbf{p}_2)\delta(\mathbf{x}_1 - \mathbf{x}_2) \tag{4.29}$$

Assuming there are no correlations between pairings, $G_{1\leftrightarrow 2}$ compares $< f_1 f_2 > - < f_1 >$ $\delta(1-2)^2$ phase-space density to the Poisson expectation in the absence of correlations. Theoretically, counting pairs of particles can be used to determine $G_{1\leftrightarrow 2}$. To find $G_{1\leftrightarrow 2}$, we just subtract the same particle contribution from $G_{1\leftrightarrow 2}$ as we did in the previous equation.

$$\left(\frac{d}{d\tau} + \nu(1-P_2) + \nu(1-P_1)\right) G_{1\leftrightarrow 2} = \Gamma_{1\leftrightarrow 2} - \left(\frac{d}{d\tau} + 2\nu(1-P_1)\right) \langle f_1 \rangle \delta(1-2) \tag{4.30}$$

or we can write the above equation as,

$$\left(\frac{d}{d\tau} + \nu(1-P_2) + \nu(1-P_1)\right) G_{1\leftrightarrow 2} = \Gamma'_{1\leftrightarrow 2} \tag{4.31}$$

---

[2] $\delta(1-2)$ is an abbreviated form of $\delta(\mathbf{p}_1 - \mathbf{p}_2)\delta(\mathbf{x}_1 - \mathbf{x}_2)$

Where

$$\Gamma'_{1\leftrightarrow 2} = -\left(\frac{d}{d\tau} + 2\nu(1-P_1)\right)\langle f_1\rangle\,\delta(1-2) + \Gamma_{1\leftrightarrow 2} \tag{4.32}$$

According to reference [48], the equations for correlation functions of two-particle in the hydrodynamic regime were constructed. They are equivalent to the equations in this study. Up to this moment, the derivations have been quite similar to one another. When a sufficiently big system is brought into local equilibrium, the pair correlation function $G_{1\leftrightarrow 2}$ disappears. If the grand canonical ensemble is used, particle number variations in equilibrium meet Poisson statistics on a small scale. The number fluctuations fulfill $\langle N\rangle = \langle N^2\rangle - \langle N\rangle^2$ in the same way as the equilibrium phase-space correlations satisfy $\langle f_1\rangle\,\delta(1-2) = (\langle f_1 f_2\rangle - \langle f_1\rangle\langle f_2\rangle)^{eq}$ in the opposite direction.

We will now proceed to calculate the coefficient $\Gamma_{1\leftrightarrow 2}$. From fundamental principles, we may deduce a great deal about the coefficient $\Gamma_{1\leftrightarrow 2}$. First, because fluctuations are stochastic in nature, $\Delta W_{i=1,2}$ is uncorrelated for distinct cell $(\mathbf{p}_i, \mathbf{x}_i)$, also for different cells $(\mathbf{p}_2, \mathbf{x}_2)$ and $(\mathbf{p}_1, \mathbf{x}_1)$. Therefore, we anticipate that $\Gamma_{1\leftrightarrow 2}$ will be singular at $(\mathbf{p}_2, \mathbf{x}_2) = (\mathbf{p}_1, \mathbf{x}_1)$ and as the cell size approaches zero, and that $\Gamma_{1\leftrightarrow 2}$ will be zero elsewhere [47]. As for the second point, we anticipate that $\Gamma_{1\leftrightarrow 2}$ will vanish in local equilibrium since correlations are caused by scattering and detailed balancing requires that $(\frac{df}{dt})_{col} = 0$. As a result, we anticipate

$$\Gamma_{1\leftrightarrow 2} = (1-P_2)(1-P_1)b_1\delta(1-2) \tag{4.33}$$

The fluctuation-dissipation theorem is used to compute the coefficient $\Gamma_{1\leftrightarrow 2}$ when the system is close to equilibrium. We can rewrite equation (4.28), taking into account $\frac{dC^e_{1\leftrightarrow 2}}{d\tau} = 0$, as

$$[\nu(1-P_2) + \nu(1-P_1)]\,C^e_{1\leftrightarrow 2} = \Gamma_{1\leftrightarrow 2} \tag{4.34}$$

Now substitute $\langle f_1\rangle\,\delta(1-2)$ in equation (4.34) instead of $C^e_{1\leftrightarrow 2}$

$$\Gamma_{1\leftrightarrow 2} = 2\nu(1-P_1)\langle f_1\rangle \tag{4.35}$$

Compare the above equation to (4.33), we can see $b_1 = 2\nu\langle f_1\rangle$. After that, we write

$$\Gamma^e_{1\leftrightarrow 2} = 2\nu(1-P_2)(1-P_1)\langle f_1\rangle\,\delta(1-2) \tag{4.36}$$

Where we used some useful properties for $P_1$ and $P_2$ from table (4.1) to reach the final answer for $\Gamma^e_{1\leftrightarrow 2}$ A system's steady-state behavior has been prevented from equilibrium by significant gradients that are maintained, for example by fixed boundary conditions is now being considered. Since the contributions from $d/d\tau = \partial/\partial t + v_1.\nabla_1 + v_2.\nabla_2$ are not zero anymore, the derivatives do not disappear under these conditions. For example, in this scenario, $Pf \neq f^{eq}$ The operation is performed on (4.31) using $P_1P_2$ is used to produce

| Projection Operator Properties | |
|---|---|
| $P_1^2 = P_1$ | $P_2^2 = P_2$ |
| $P_1^\dagger = P_1$ | $P_2^\dagger = P_2$ |
| $P_1(1 - P_1) = 0$ | $P_2(1 - P_2) = 0$ |
| $(1 - P_1)^2 = 1 - P_1$ | $(1 - P_2)^2 = 1 - P_2$ |
| $P_1(1 - P_2) \neq 0$ | $P_2(1 - P_1) \neq 0$ |
| $P_1P_2\frac{d}{d\tau} = \frac{d}{d\tau}P_1P_2$ | $P_2P_1\frac{d}{d\tau} = \frac{d}{d\tau}P_2P_1$ |

Table 4.1: Useful properties for projection operators $P_1$ and $P_2$

$$P_1P_2\Gamma'_{1\leftrightarrow 2} = -P_1P_2\left(\frac{d}{d\tau} + 2\nu(1 - P_1)\right)\langle f_1\rangle\,\delta(1-2) + P_1P_2\Gamma_{1\leftrightarrow 2}.$$

The second and the third term from the above equation will vanish due to orthogonality Table 4.1. We will substitute $-\nu(\langle f\rangle - f^{eq})$ instead of $d\langle f\rangle/d\tau$, the above equation can be written as,

$$P_1P_2\Gamma'_{1\leftrightarrow 2} = \nu P_1P_2(\langle f_1\rangle - f_1^{eq})\delta(1-2) \tag{4.37}$$

In the moment when the boundary limitations are no longer present. In our investigation, we discover

$$\Gamma'_{1\leftrightarrow 2} = \nu P_1P_2(\langle f_1\rangle - f_1^{eq})\delta(1-2) \tag{4.38}$$

To find $\Gamma_{1\leftrightarrow 2}$, multiply equation (4.32) by $(1 - P_2)(1 - P_1)$

$$\begin{aligned}(1 - P_2)(1 - P_1)\Gamma'_{1\leftrightarrow 2} &= -\left(\frac{d}{d\tau} + 2\nu(1 - P_1)\right)\langle f_1\rangle\,\delta(1-2) + \Gamma_{1\leftrightarrow 2}\\ 0 &= -(1 - P_2)(1 - P_1)\left(\frac{d}{d\tau} + 2\nu(1 - P_1)\right)\langle f_1\rangle\,\delta(1-2) + \Gamma_{1\leftrightarrow 2}\\ \Rightarrow \Gamma_{1\leftrightarrow 2} &= (1 - P_2)(1 - P_1)\frac{d\langle f_1\rangle}{d\tau}\delta(1-2)\\ &\quad + 2\nu(1 - P_2)(1 - P_1)\langle f_1\rangle\,\delta(1-2)\end{aligned}$$

substitute $-\nu(\langle f\rangle - f^{eq})$ instead of $d\langle f\rangle/d\tau$. The last equation can be written as,

$$\Gamma_{1\leftrightarrow 2} = \nu(1-P_2)(1-P_1)(\langle f_1\rangle + f_1^{eq})\delta(1-2) \tag{4.39}$$

We will now develop the general evolution equation in the case of two-body correlation function.

$$\left(\frac{d}{d\tau} + \nu(1-P_2) + \nu(1-P_1)\right) G_{1\leftrightarrow 2} = \nu P_1 P_2(\langle f_1\rangle - f_1^{eq})\delta(1-2) \tag{4.40}$$

In this case, projection operators make sure that energy, momentum, and numbers stay the same. There's a lot of information to cover, so we show the drift terms in a rest frame and write them down as,

$$\left(\frac{\partial}{\partial t} + \nu(2-P_2-P_1) + \mathbf{v_1}.\nabla_\mathbf{1} + \mathbf{v_2}.\nabla_\mathbf{2}\right) G_{1\leftrightarrow 2} = \nu P_1 P_2(\langle f_1\rangle - f_1^{eq})\delta(1-2). \tag{4.41}$$

In which the relaxation rate $\nu$ and the projection operators $P_{i=1,2}$ are determined by $\langle f\rangle \equiv \langle f(\mathbf{p},\mathbf{x},t)\rangle$, the average one-body distribution, as well as the local equilibrium distribution $f^{eq}$. A broad examination of the BBGKY hierarchy was used to develop equation (4.41) for non-relativistic fluids, which was published in reference [49] by Dufty, Lee, and Brey.

### 4.4 Ion collisions connected to relativistic transport equation

Can we apply these equations in phenomenological contexts in some way? The beginning condition for solving equation (4.40) corresponds to a single collision occurrence, thus we begin with that initial condition. In this case, we may use (3.28) to solve the one-body equation for $f(\mathbf{p},\mathbf{x},t)$ in conjunction with the conservation constraints to obtain the solution. For the correlation function, we solve (4.40) for a while. Averaging across an ensemble of initial circumstances are then required. Physically, there is no restriction on the size of the difference between $\langle f\rangle$ and $f^{eq}$; the only restriction is that the fluctuations $f-\langle f\rangle$ must be small. According to reference [34] for example, such generic solutions do not necessarily have to attain equilibrium.

In order to show how this method can be used for collisions between heavy ions, we will use these results as an example. It's a good assumption for this thesis that the phase space distribution's deviation from its equilibrium value is always small enough that the linearized solution for $\langle f\rangle$ is right for this case. Use the conservation conditions, or solve the dissipation-free Euler equations, to figure out the effective $T$, $\mu$ and $\mathbf{v}$ parameters for the start of each event in this scenario. We won't need to do this for our goals. There is no longer a source phrase in (4.40) that is used in this work.

Observable effects of pre-equilibrium correlations that are dependent on the correlation function $G_{12}$ are of particular interest to us.

$$G_{12} = \langle f_1 f_2\rangle - \langle f_1\rangle \langle f_2\rangle - \langle f_1\rangle \delta(1-2) \tag{4.42}$$

In this section, we will design formal solutions based on the formal solutions used in the creation of $G_{12}$. We will start with the identity operator relation,

$$1 = P_1P_2 + P_2(1-P_1) + P_1(1-P_2) + (1-P_1)(1-P_2) \tag{4.43}$$

Multiply the identity equation by $G_{12}$

$$G_{12} = P_1P_2G_{12} + P_2(1-P_1)G_{12} + P_1(1-P_2)G_{12} + (1-P_1)(1-P_2)G_{12}. \tag{4.44}$$

Let

$$\begin{aligned} G^e_{12} &= P_1P_2G_{12} \\ X_{21} &= P_2(1-P_1)G_{12} \\ X_{12} &= P_1(1-P_2)G_{12} \\ \Delta G_{12} &= (1-P_1)(1-P_2)G_{12} \end{aligned}$$

As a result, we have

$$G_{12} = G^e_{12} + X_{21} + X_{12} + \Delta G_{12} \tag{4.45}$$

Where the equilibrium function $G^e_{12}$ is defined in the same way as the correlation function $C^e_{12}$, and as a result, we obtain $G^e_{12} = C^e_{12} - P\langle f_1\rangle \delta(1-2)$.In case of $P_1\langle f_1\rangle = f^e$ and $df/d\tau = 0$, we can find the completely linearized solution (3.43). Apply $P_1P_2$ on the equation (4.40)

$$\left(P_1P_2\frac{d}{d\tau} + \nu P_1P_2(1-P_2) + \nu P_1P_2(1-P_1)\right) G_{12} = \nu P_1^2P_2^2(\langle f_1\rangle - f_1^{eq})\delta(1-2)$$

The second and third terms from the left side equality will vanish due to orthogonality, while the first term will commute with $\frac{d}{d\tau}P_1P_2$. The above equation can be written as,

$$\frac{d}{d\tau}G^e_{12} = -\nu P_1P_2(f^{eq}_1 - \langle f_1\rangle)\delta(1-2)$$

$$\therefore \frac{d}{d\tau}G^e_{12} = -P_1P_2\frac{d}{d\tau}\left\langle f_1\right\rangle \delta(1-2) \tag{4.46}$$

Apply $P_2(1-P_1)$ on equation (4.42),

$$\begin{aligned} P_2(1-P_1)G_{12} &= P_2(1-P_1)\left\langle f_1f_2\right\rangle - P_2(1-P_1)\left\langle f_1\right\rangle\left\langle f_2\right\rangle - P_2(1-P_1)\left\langle f_1\right\rangle\delta(1-2) \\ X_{21} &= \left\langle f_1f^e_2\right\rangle - \left\langle f^e_1f^e_2\right\rangle - \left\langle f_1\right\rangle\left\langle f^e_2\right\rangle + \left\langle f^e_1\right\rangle\left\langle f^e_2\right\rangle \\ &= \left\langle (f_1-f^e_1)f^e_2\right\rangle - (\left\langle f_1-f^e_1\right\rangle)\left\langle f^e_2\right\rangle \end{aligned}$$

The phase-space distribution's variation from local equilibrium is denoted by the symbol $\delta f = f - f^e$. The above equation can be written as

$$X_{21} = \left\langle \delta f_1f^e_2\right\rangle - \left\langle \delta f_1\right\rangle\left\langle f^e_2\right\rangle \tag{4.47}$$

The above-mixed correlation function $X_{21}$ is the covariance relation. Apply $P_2(1-P_1)$ on equation (4.40) we find

$$\left(\frac{d}{d\tau}P_2(1-P_1) + 0 + \nu P_2(1-P_1)\right)G_{1\leftrightarrow 2} = 0$$

$$\frac{dX_{21}}{d\tau} = -\nu X_{21} \tag{4.48}$$

$$\therefore X_{21} = X^0_{21}S \tag{4.49}$$

Where $S$ is the survival probability and $X^0_{21}$is the initial function and its value can be determined from the initial distribution of nucleon participants, as well as their first few interactions, influence its value. We will do the same steps to find the solution of $X_{12}$ but instead of applying $P_2(1-P_1)$ we will apply $P_1(1-P_2)$

$$X_{21} = \left\langle \delta f_2f^e_1\right\rangle - \left\langle \delta f_2\right\rangle\left\langle f^e_1\right\rangle \tag{4.50}$$

$$\frac{dX_{12}}{d\tau} = -\nu X_{12} \tag{4.51}$$

$$X_{12} = X^0_{12}S \tag{4.52}$$

Where $S$ is the survival probability and $X_{12}^0$ is the initial function and its value can be determined from the initial distribution of nucleon participants, as well as their first few interactions, influence its value.

Apply $(1-P_1)(1-P_2)$ on equation (4.42)

$$\begin{aligned}\Delta G_{12} = (1-P_1)(1-P_2)\langle f_1 f_2\rangle - (1-P_1)(1-P_2)\langle f_1\rangle\langle f_2\rangle \\ - (1-P_1)(1-P_2)\langle f_1\rangle\delta(1-2)\\ \Delta G_{12} = -\langle f_2 f_1^e\rangle - \langle f_1 f_2^e\rangle + \langle f_1^e f_2^e\rangle + \langle f_1 f_2\rangle + \langle f_1\rangle\langle f_2^e\rangle + \langle f_2\rangle\langle f_1^e\rangle \\ - \langle f_1^e\rangle\langle f_2^e\rangle - \langle f_1\rangle\langle f_2\rangle + \langle f_1\rangle\delta(1-2) - \langle f_1^e\rangle\delta(1-2)\end{aligned}$$

$$\therefore \Delta G_{12} = \langle \delta f_1 \delta f_2\rangle - \langle \delta f_1\rangle\langle \delta f_2\rangle - \langle \delta f_1\rangle\delta(1-2) \tag{4.53}$$

The above equation is the contribution of non-equilibrium to correlations. Apply $(1-P_1)(1-P_2)$ on equation (4.40)

$$\left(\frac{d}{d\tau}(1-P_2)(1-P_1) + \nu(1-P_2)(1-P_1)^2 + \nu(1-P_2)^2(1-P_1)\right) G_{1\leftrightarrow 2} = 0$$

$$\frac{d\Delta G_{12}}{d\tau} = -2\nu\Delta G_{12} \tag{4.54}$$

$$\therefore \Delta G_{12} = \Delta G_{12}^0 S^2 \tag{4.55}$$

$\Delta G_{12}^0$ is the initial function and its value can be determined from the initial distribution of nucleon participants, as well as their first few interactions, influence its value. The solution of the new relativistic transport equation can be written as,

$$G_{12} = G_{12}^e + X_{21}^0 S + X_{12}^0 S + \Delta G_{12}^0 S^2 \tag{4.56}$$

The local equilibrium correlation function for two particles is defined as,

$$G_{12}^e = G_{12}^e(\mathbf{x_1} - \mathbf{v_1}t, \mathbf{p_1}, \mathbf{x_2} - \mathbf{v_2}t, \mathbf{p_2}) \tag{4.57}$$

In chapter 7, we will demonstrate a way of integrating the solution (4.56) to examine the approach to thermalization by employing $p_t$ fluctuations to investigate the solution integration method.

# CHAPTER 5 NEW OBSERVABLE $'\mathcal{D}'$

The main goal of this chapter is to characterize as precisely as possible the likely observables of a heavy-ion collision. There are a variety of observables, ranging from the most basic, such as particle multiplicity, which just counts the number of particles formed in a collision, to more complex ones, such as various correlation functions, which are described in detail below.

In this dissertation, we demonstrate that the observables $\mathcal{R}$, $\mathcal{C}$, $\mathcal{D}$, and $\langle \delta p_{t1} \delta p_{t2} \rangle$, which are all two-particle correlation observables, are mathematically connected by equation (5.12). When these observables are observed or calculated at the same time using the same method, (5.12) can be used as a validation tool for theoretical models, depending on the circumstances. Importantly, because each observable corresponds to a separate component of the collision system, (5.12) may be used to estimate the relative impacts of different physics on a single observable.

In fluctuations and correlations section, We will explore briefly how to design a generic two-particle momentum density correlation function, equation (5.18). The four related two-particle correlation observables (5.8), (5.9), (5.10), and (5.11) all originate from this common source.

$\mathcal{R}$ stands for the multiplicity fluctuations described in Section 5.6, test particle production mechanisms. They are strongly impacted by centrality or volume fluctuations, demonstrating a link between the collision region's overlap and the quantity of created particles. $\mathcal{R}$ is created in such a way that it equals zero if the event multiplicity is totally independent between events that are, if the resulting particle distribution is Poissonian, by means the particle variance equals the mean. In the case of a non-zero $\mathcal{R}$, it shows that events within the same ensemble produce particles using a shared underlying particle production physics, resulting in an event-by-event correlation. While it is tempting to explain this association to the geometrical initial state distribution in nuclear collisions, $\mathcal{R}$ is not zero in *pp* collisions as well. This may imply that sub-nucleon scale physics more correctly describes the initial state.

Momentum correlations, $\mathcal{C}$, are the weighted transverse momentum equivalent of $\mathcal{R}$, as described by (5.47) in Section 5.7. Due to the momentum weighting, these correlations are sensitive in case of dynamical forces acting on the collision system during its evolution, such as viscosity, with the initial state factors that produce $\mathcal{R}$.

Transverse momentum fluctuations, described by (5.19) in Section 5.4, have been widely investigated as a measure of collision dynamic systems, temperature fluctuations, and the critical point phase change phenomena. We demonstrate in this study, for the first time, how the multiplicity fluctuations, momentum correlations, and momentum-multiplicity correlations together contribute to $\langle \delta p_{t1} \delta p_{t2} \rangle$. Additionally, Equation (5.55) demonstrates how, in comparison to other correlation observables, $\langle \delta p_{t1} \delta p_{t2} \rangle$ is robust to changes in centrality definition. Since $\mathcal{C}$ and $\mathcal{R}$ both contain the same number density fluctuations, the difference $- \langle p_t \rangle \mathcal{R} + \mathcal{C}$ in (5.55) effectively eliminates the number density fluctuations associated with their shared centrality definition.

Additionally, this thesis introduces the concept of a multiplicity-momentum correlation measure, $\mathcal{D}$, defined by (5.28). In momentum-multiplicity section, we estimate that $\mathcal{D}$ equals zero in the Grand Canonical Ensemble. In contrast, in chapter 6, we get a positive result equivalent in size to $\langle \delta p_{t1} \delta p_{t2} \rangle$ from PYTHIA simulations. PYTHIA simulations do not include bulk correlation dynamics, and we suggest that the growing value of the average transverse momentum of a particle with increasing multiplicity supports a positive multiplicity-momentum correlation in both $pp$ and $AA$ collision systems.

## 5.1 The grand canonical ensemble's parameters

As part of the comparison, the density matrix in quantum statistics is used in similar ways to the density function $\rho(p, x)$. When we use classical statistics, we can show from $\rho(p, x)$ how likely it is that the coordinates and momenta of the particles of the body will be different. The diagonal matrix of the density matrix $\rho_{mm} = \rho_m$ in quantum statistics shows how likely it is that the body will be in a certain state $m$. In quantum statistics, the most important thing to do is figure out the density matrix. To do this, we'll figure out the density matrix for all three types of ensembles.

- *Microcanonical ensemble* Let us consider a microcanonical ensemble with an energy range ranging between the values $E$ and $E + \delta E$, Where $E$ is much smaller than $\delta E$. It can be found in a huge number of microstates at the same time. Due to our lack of knowledge regarding microstates, we assign an equal possibility to each potential microstate scenario.

In the case of $E_m$ between $E$ and $E + \delta E$

$$\rho_m = \frac{1}{\sum_{E_m} 1}$$

Otherwise

$$\rho_m = 0$$

- *Canonical ensemble.* During the course of a canonical ensemble, the system under investigation is capable of exchanging energy with the surrounding environment at the temperature $T$, which is equal to $\frac{1}{\beta}$. It is possible to apply a weight factor $e^{-\beta E_m}$ to the likelihood of finding the system in the energy state $E_m$. It is then represented as the density matrix of the canonical ensemble of elements which can be written as,

$$\rho_m = \frac{e^{-\beta E_m}}{\sum_m e^{-\beta E_m}}$$

The $\sum_m e^{-\beta E_m}$ is known as the partition function and is represented by the symbol $Z$. In fact, it is essentially a trace of the operator $e^{-\beta \hat{H}}$, with $\hat{H}$ denoting the system's Hamiltonian.

$$Z = \sum_m e^{-\beta E_m} = Tr e^{-\beta \hat{H}}$$

- *Grand canonical ensemble.* Both the number of particles and the energy of the grand canonical ensemble are subject to change. One can apply a weight factor $e^{-\beta(E_m - \mu N_m)}$ to the probability of discovering the system of $N_m$ particles in the energy state $E_m$ by using a probability distribution. It is then stated as the density matrix for this ensemble, which can be written as

$$\rho_m = \frac{e^{-\beta(E_m - \mu N_m)}}{\sum_m e^{-\beta(E_m - \mu N_m)}}$$

The partition function of the grand canonical ensemble is defined as,

$$Z = \sum_m e^{-\beta(E_m - \mu N_m)} \tag{5.1}$$

The observable or expected value of any operator may be calculated using the partition function, which looks like this:

$$\langle A \rangle = \frac{TrAe^{-\beta(\hat{H}-\mu\hat{N})}}{Tre^{-\beta(\hat{H}-\mu\hat{N})}} \tag{5.2}$$

The explicit relations for determining the particle number and energy of a system are derived from the grand canonical partition function in the next step.

If we differentiate $\ln Z$ with respect to $\alpha = \mu\beta$ ($\alpha$ is a variable has a condition $\frac{d\alpha}{d\beta} = 0$) we are able to obtain

$$\frac{\partial \ln Z}{\partial \alpha} = \frac{Tre^{-\beta(\hat{H}-\mu\hat{N})}(\hat{N})}{Z} = \langle N \rangle \tag{5.3}$$

Differentiate $\ln Z$ with respect to $\beta$ to obtain

$$\frac{\partial \ln Z}{\partial \beta} = -\frac{Tre^{-\beta(\hat{H}-\mu\hat{N})}\hat{H}}{Z} = -\langle E \rangle\,. \tag{5.4}$$

The average energy can be written as

$$\langle E \rangle = -\frac{1}{Z}\frac{\partial Z}{\partial \beta}. \tag{5.5}$$

The partition function may also be used to compute fluctuations in particle counts or in the energy-particle count, which are both useful functions. For example, by twice differentiating equation (5.3), we get the following result:

$$\frac{\partial^2 \ln Z}{\partial \alpha^2} = \frac{Tre^{-\beta(\hat{H}-\mu\hat{N})}(\hat{N}^2)}{Z} - \frac{\left[Tre^{-\beta(\hat{H}-\mu\hat{N})}\hat{N}\right]^2}{Z^2} = \langle N^2 \rangle - \langle N \rangle^2$$

$$\therefore \frac{\partial \langle N \rangle}{\partial \alpha} = \langle N^2 \rangle - \langle N \rangle^2 \tag{5.6}$$

In order to obtain energy particle fluctuation, differentiate equation (5.4) as a function of $\alpha$

$$\frac{\partial^2 \ln Z}{\partial \alpha \partial \beta} = \frac{Tre^{-\beta(\hat{H}-\mu\hat{N})}\hat{N}\hat{H}}{Z} - \frac{\left(Tre^{-\beta(\hat{H}-\mu\hat{N})}\hat{N}\right)\left(Tre^{-\beta(\hat{H}-\mu\hat{N})}\hat{H}\right)}{Z^2}$$

$$\therefore \frac{\partial \langle E \rangle}{\partial \alpha} = \langle NE \rangle - \langle N \rangle \langle E \rangle \tag{5.7}$$

We will use later the grand canonical ensemble to study the multiplicity-momentum correlations.

## 5.2 Defining observables

Observables are defined in this section, and we will go over them in further detail in the next sections. We shall begin with a new observable defined as multiplicity-momentum correlations, which can be written as,

$$\mathcal{D} = \frac{\int\int d^3\mathbf{p_1} d^3\mathbf{p_2}\ r(\mathbf{p_1}, \mathbf{p_2})\ (p_{t1} - \langle p_t \rangle)}{\langle N \rangle^2} \tag{5.8}$$

where $r(\mathbf{p_1}, \mathbf{p_2})$ is the correlation momentum density for two particles with momenta $\mathbf{p_1}$ and $\mathbf{p_2}$, $(p_{t1} - \langle p_t \rangle)$ represents the fluctuation of a particle's transverse momentum relative to the global event ensemble average and $\langle N \rangle$ signifies the event averaged multiplicity of a particle. We will discus that $\mathcal{D}$ vanishes entirely if the only source of momentum-multiplicity correlations is the presence of multiplicity fluctuations. Additionally, we establish that $\mathcal{D}$ is 0 when the Grand Canonical Ensemble is in equilibrium. A non-zero value for $\mathcal{D}$ may suggest insufficient thermalization and correspond to correlations arising from the particle creation mechanism that persisted until the particle production process freeze-out.

We will show in the chapter 6 that PYTHIA and Angantyr simulations of proton-proton and nucleus-nucleus collisions reveal that $\mathcal{D}$ does not equal zero in these cases. Furthermore, we discover that $\mathcal{D}$ has a value that is equivalent to correlations of transverse momentum fluctuations, $\langle \delta p_{t1} \delta p_{t2} \rangle$, which have been well quantified at both the LHC and RHIC. In prior work, we considered $\mathcal{D}$ to be zero, and this is also assumed in reference [50], where ALICE analyzes two-particle transverse momentum correlations differently in relative azimuthal angle and relative pseudorapidity.

We will define another observable which is Transverse momentum fluctuations correlations. Therefore it is possible to express this as

$$\langle \delta p_{t1} \delta p_{t2} \rangle = \frac{\int\int d^3\mathbf{p_1} d^3\mathbf{p_2}\ r(\mathbf{p_1}, \mathbf{p_2})\ \delta p_{t1} \delta p_{t2}}{\langle N(N-1) \rangle} \tag{5.9}$$

Where $\delta p_t = p_t - \langle p_t \rangle$ represents the fluctuation of a particle's transverse momentum relative to the global event ensemble average and $r(\mathbf{p_1}, \mathbf{p_2})$ is the correlation momentum density for two particles. This observable was measured by STAR in reference [51], for the first time and now in this work we will show how the analytic form of this observable is linked to the one that can be measured.

Unlike other definitions, the similarities between multiplicity-momentum correlations and correlations of transverse momentum fluctuations are not only coincidental; they are both part of a larger set of observed variables that are mathematically related by the correlation function $r(\mathbf{p_1}, \mathbf{p_2})$, which is itself an observable in the form.

Multiplicity fluctuation observables defined as

$$\mathcal{R} = \frac{\int\int d^3\mathbf{p_1} d^3\mathbf{p_2}\ r(\mathbf{p_1}, \mathbf{p_2})}{\langle N\rangle^2} \tag{5.10}$$

$\mathcal{R}$ has been extensively explored as a metric for volume or centrality fluctuations, as well as a possible indicator of the commencement of QGP and QCD critical point fluctuations. In multiplicity fluctuation section, we go through these details as well as the experimental measurement of $\mathcal{R}$. The depiction of $\mathcal{R}$ in an independent source model, which is explained in chapter 6, also informs $\mathcal{R}$'s dependency on volume variations. Particle sources fluctuate from event to event, causing volume fluctuations.

Transverse momentum correlations

$$\mathcal{C} = \frac{\int\int d^3\mathbf{p_1} d^3\mathbf{p_2}\ r(\mathbf{p_1}, \mathbf{p_2}) p_{t,1} p_{t,2}}{\langle N\rangle^2} \tag{5.11}$$

in other words, they are produced from the same volume fluctuations and initial state correlations that generate $\mathcal{R}$, and they functionally represent a transverse momentum weighted version of $\mathcal{R}$. $\mathcal{C}$, on the other hand, is sensitive to the system's expansion and equilibrium dynamics due to its momentum dependency.

The most important finding of this study is that the multiplicity momentum correlations, $\mathcal{D}$, correlations and fluctuations of transverse momentum,$\langle \delta p_{t1} \delta p_{t2}\rangle$ , multiplicity fluctuations, $\mathcal{R}$, and transverse momentum correlations, $\mathcal{C}$, are mathematically connected by the equation.

$$(1+\mathcal{R}) \langle \delta p_{t1} \delta p_{t2}\rangle + 2 \langle p_t\rangle \mathcal{D} - \mathcal{C} + \langle p_t\rangle^2 \mathcal{R} = 0. \tag{5.12}$$

This is how we arrive at the conclusion shown later in the upcoming sections in this chapter. When each observable is assessed separately, the result of (5.12) gives a previously undiscovered validation. As an added bonus, models that exhibit high agreement with one observable may now utilize that comparison as a baseline for simultaneously addressing the other two observables, and so on. Furthermore, each observable may represent a separate physical effect, and with the help of equation (5.12), one observed value may be subdivided into the contributions from each individual effect.

In the parts that follow, we will go over each observable in depth, as well as how we link them using an equation (5.12), which is also we defined it as the sum rule method.

## 5.3 Fluctuations and correlations

Fluctuations affect all observables, and these fluctuations are often influenced by the characteristics of the system, and they may be utilized to investigate these properties. These fluctuations can be divided into two categories. At the most fundamental level, each collision event is distinct from the others because a limited and changing number of particles are generated. The fact that each event has a finite magnitude is a fundamental source of fluctuations, which we refer to collectively as statistical fluctuations. We can determine the magnitude of these fluctuations by examining how a system acts while it is in local equilibrium. The second sort of fluctuations are those that occur above equilibrium, which we refer to as dynamical fluctuations. These fluctuations include all other forms of fluctuations.

In the event of a nuclear collision, one of the most fundamental quantities that may be seen is the number of particles that impact a detector. This observable is referred to as the multiplicity of the event and is denoted by the letter $N$. The event averaged multiplicity $\langle N \rangle$ is obtained by repeating this measurement for a large number (millions) of collisions and averaging the results.

$$\langle N \rangle = \int d^3\mathbf{p}\ \rho_1(\mathbf{p}) \tag{5.13}$$

Where

$$\rho_1(\mathbf{p}) = \frac{dN}{d^3\mathbf{p}} = \int d^3\mathbf{x}\, \langle f(\mathbf{x}, \mathbf{p}) \rangle \tag{5.14}$$

Here $\rho_1$ is the single-particle momentum density which is related to the average phase space density $\langle f(\mathbf{x}, \mathbf{p}) \rangle$.

The average number of particle pairs when auto-correlations are not taken into consideration is defined as,

$$\langle N(N-1)\rangle = \int\int d^3\mathbf{p}_1 d^3\mathbf{p}_2 \; \rho_2(\mathbf{p_1}, \mathbf{p_2}), \tag{5.15}$$

where

$$\rho_2(\mathbf{p_1}, \mathbf{p_2}) = \frac{dN}{d^3\mathbf{p}_1 d^3\mathbf{p}_2} = \int\int d^3\mathbf{x}_1 d^3\mathbf{x}_2 \left[\langle f(\mathbf{x_1}, \mathbf{p_1}) f(\mathbf{x_2}, \mathbf{p_2})\rangle - \langle f_1\rangle\, \delta(1-2)\right]. \tag{5.16}$$

Here $\rho_2$ is the pair momentum density which is related to the phase space density $f$.

It is necessary to define the two-particle momentum density before we can generate any correlation observables for two particles.

$$\rho_2(\mathbf{p_1}, \mathbf{p_2}) = \rho_1(\mathbf{p_1})\rho_1(\mathbf{p_2}) + r(\mathbf{p_1}, \mathbf{p_2}) \tag{5.17}$$

According to equation (5.17), particle pairs can be created in two different ways. If pairs are created from independent particles, by means there are no correlations between them, then the pair distribution is just the product of two single-particle densities multiplied by one another ($\rho_1\rho_1$). The second kind of correlated pairings is represented by the

$$r(\mathbf{p_1}, \mathbf{p_2}) = \rho_2(\mathbf{p_1}, \mathbf{p_2}) - \rho_1(\mathbf{p_1})\rho_1(\mathbf{p_2}) \tag{5.18}$$

Correlations are eliminated by construction in the situation of uncorrelated particle emission, which occurs when just statistical fluctuations are present.

At this point, we don't know what physical mechanisms are at work to make the correlations in equation (5.18) happen, even though there are many possibilities.
$\sum_{n=2} v_n \cos(n\phi - n\psi_n)$ [17, 52, 53], where $\sum_{n=2} v_n \cos(n\phi - n\psi_n)$ is the particle azimuthal distribution. The coefficients $v_n$ of a Fourier fit is used to the particle azimuthal distribution are called "flow," and they show how the angle of emission (momentum) changes with the event plane. A lot of effort has been expended in recent years to identify "nonflow" correlations such as HBT-like femtoscopic correlations [54, 55], momentum conservation [56, 57] resonance decays and final state interactions [58], and jets. Various papers [14, 59] have proposed that particles created in close spatial proximity to one another develop a momentum connection due to transverse expansion. We hypothesize

that this mechanism accounts for a large fraction of the signal found in two-particle correlations. Given that this influence is only loosely tied to the event of the reaction plane, many would classify this effect as a non-flow effect.

Rather than attempting to diagnose the relative contributions of distinct correlation mechanisms in a single observable, we suggest a set of observables that all begin with $\rho_2$, are sensitive to a different physics, and they are linked mathematically by sum-rule formula equation (5.12).

Correlation and fluctuation values are commonly measured in current research [60, 61, 50] using relative azimuthal angle ($\Delta\phi = \phi_1 - \phi_2$) and the relative pseudorapidity ($\Delta\eta = \eta_1 - \eta_2$). In several investigations, pairings separated by a pseudorapidity gap bigger than ($|\Delta\eta| \approx 1$) are also measured.

Analyzing observables as a function azimuthal angle for the identification of anisotropic flow contributions. As can be seen from the similarity of the patterns shown by the projections of differential measurements like (5.9), (5.10), and (5.11) onto the azimuthal axis, the two peaks at $\Delta\phi = 0$ and at $\Delta\phi = \pi$ that appear are consistent with anisotropic flow and momentum conservation. These observables likewise exhibit a wider peak at $\Delta\phi = \pi$ compared to the narrower peak at $\Delta\phi = 0$ in these data. These findings have been often ascribed to triangular flow.

In order to minimize 'short-range' $|\Delta\eta|$, correlations, and other phenomena like resonance decays and jets, pseudorapidity gaps between pairs are utilized. Separately, in differential measurements, the effects of HBT and track pileup are frequently eliminated by removing the $\Delta\eta = 0$ bin from the equation. All three differential measurements of (5.9), (5.10), and (5.11) indicate a "long-range" correlation, $|\Delta\eta| > 1 - 2$, in center collisions when projected onto the $\Delta\eta = 0$ axis of the differential observations. In addition to detector rapidity acceptances, this long-range 'near-side' ($\Delta\phi = 0$) connection appears to extend beyond the detector rapidity acceptances. As a result, the near-side peak is frequently depicted as a peak resting on a long and flat pedestal, which is referred to as 'the ridge.' Anisotropic flow harmonics [62, 60, 50, 63, 64] are frequently used to fit experimental measurements of the ridge with a Fourier series flat in $\Delta\eta$ and then connect the coefficients from the Fourier series to the anisotropic harmonics flow. It is the correlations in excess of the ridge (i.e., correlations in excess of flow correlations) that are represented by the peak sitting on the pedestal, which nevertheless extends to long-range in $\Delta\eta$ (and perhaps beyond the experimental acceptability) in center collisions. As collisions grow more peripheral, the $\Delta\eta$ of this surplus reduces in broadness. The widths of the peripheral peaks are in the range of 0.5 to 1, which is consistent with the resonance decay correlations and jet. The growing breadth of the near side peak as the number of collisions moves from peripheral to central implies that a correlation mechanism other than flow harmonics is at work. Reference [48] is an example of this.

Fourier series can be written as $\sum_{n=2} a_n \cos(n\Delta\phi)$. If the observables (5.9), (5.10), and (5.11) in $(\Delta\eta, \Delta\phi)$ are not measured individually, then all flow effects are excluded from consideration. To further understand this, consider the following scenario: the quantity $\mathcal{R}(\Delta\phi)$ has been measured and is well characterized by a Fourier series taking into consideration the terms $a_n \cos(n\Delta\phi)$ . To obtain the integrated amount, one calculates $\mathcal{R} = \int \mathcal{R}(\Delta\phi) d\Delta\phi$, where $\mathcal{R}$ again is the multiplicity fluctuation. For example, when computing the corresponding integral of the Fourier series over a symmetric interval, the integral of all terms $\cos(n\Delta\phi)$ across a symmetric interval vanishes term by term, suggesting that if correlations are solely characterized by flow, $\mathcal{R}$ =0 is obtained. Despite the fact that these residual correlations may be classified as non-flow, they are nevertheless fascinating and may give significant information about the dynamics of the collisions or their initial state. We pay particular attention to long-range approaching correlations in excess of flow. It is also possible to discriminate between different types of events depending on their jet features by looking at the integrated observables. Instead, the centrality and dependency on energy of these correlations might suggest how thermalized events are, which we will leave to future research.

The correlations (5.18) also illustrate the variations in generated particles that occur from event to event. It is important to note that integrating (5.18) over all momenta in the form of

$$\begin{aligned}\int\int d^3\mathbf{p_1}d^3\mathbf{p_2}r(\mathbf{p_1},\mathbf{p_2}) &= \int\int d^3\mathbf{p_1}d^3\mathbf{p_2}\left[\rho_2(\mathbf{p_1},\mathbf{p_2})-\rho_1(\mathbf{p_1})\rho_1(\mathbf{p_2})\right]\\ &= \langle N(N-1)\rangle - \left\langle N^2\right\rangle\\ &= Var(N) - \langle N\rangle\end{aligned}$$

where the fluctuations in generated particles are characterized by this method $Var(N) = \langle N^2\rangle - \langle N\rangle^2$. Given that each event is completely independent of the others, it is reasonable to expect this variance to follow the Poisson distribution - where the variance equals the mean. This would result in a vanishing integral of the variance (5.18).

It is possible to have non-Poissionian fluctuations in an ensemble of events when a physical mechanism (in initial state formation, dynamical expansion, or final state interactions) causes fluctuations that are correlated across all of the events in the ensemble; in this scenario, $r(\mathbf{p_1},\mathbf{p_2}) \neq 0$. Consequentially, because these fluctuations are linked to physical processes, they are not fully random and may be distinguished from one another using correlation observables. Non-Poissionian behavior seen in both experiments and simulations, and will be described in more detail in the following sections.

### 5.4 Correlations of transverse momentum fluctuations

It has been intensively explored as a putative indication for the existence of QGP as correlations of transverse momentum in excess of multiplicity fluctuations, as specified by (5.9) [65, 66, 67, 51, 68, 69, 70, 71, 72, 73, 62, 60, 74]. QCD critical point searches explore for non-monotonic behaviors because fluctuations are predicted to diverge if the system undergoes a phase transition [75, 76], and hence non-monotonic behaviors are sought. Additionally, the event-by-event change in $p_t$ may be utilized as a metric of temperature fluctuations throughout the course of an event [51, 77]. We are particularly interested in momentum correlations indicated by equation (5.9), which are experimentally quantifiable with

$$\langle \delta p_{t1}\delta p_{t2}\rangle = \frac{1}{\langle N(N-1)\rangle}\cdot\left\langle \sum_{i=1}^{N_k}\sum_{j=1,j\neq i}^{N_k}\delta p_{tj}\delta p_{tj}\right\rangle \tag{5.19}$$

where

$$\delta p_{t,i} = p_{t,i} - \langle p_t \rangle \tag{5.20}$$

is the term refers to the fluctuations of particle $i'$s transverse momentum in event $k$ from the total average transverse momentum per particle for a certain centrality class. Due to the fact that (5.20) represents a fluctuation, (5.19) represents a covariance of fluctuations. In order to prevent misunderstanding, we separate correlations of transverse momentum fluctuations (5.19) from the transverse momentum correlations, $\mathcal{C}$, in section 5.7 in this course. In section 5.8, we will look at the relation between these two types of correlations.

The covariance of the transverse momentum fluctuations deviating from the global average is measured by the function $\langle \delta p_{t1} \delta p_{t2} \rangle$. Each particle in a pair contributes positively to $\langle \delta p_{t1} \delta p_{t2} \rangle$ when the particles in the pair have bigger or smaller $p_t$ than the average. Each particle in a pair adds negatively to the sum of $\langle \delta p_{t1} \delta p_{t2} \rangle$ when one particle has a positive $\delta p_t$ and the other particle has a negative $\delta p_t$. $\langle \delta p_{t1} \delta p_{t2} \rangle = 0$ in the case of entirely independent particle emission.

A little difference exists between the definition (5.19) and the definitions discovered in experimental measurements. Experiments are used to measure

$$\langle \delta p_{t1} \delta p_{t2} \rangle = \frac{1}{N_{event}} \sum_{k=1}^{N_{event}} \frac{\mathcal{C}_k}{N_k(N_k - 1)} \tag{5.21}$$

where

$$\mathcal{C}_k = \sum_{i=1}^{N_k} \sum_{j \neq i, j=1}^{N_k} (p_{t,i} - M_{pt} >)(p_{t,i} - M_{pt}) \tag{5.22}$$

with

$$M_{pt} = \frac{1}{N_{event}} \sum_{k=1}^{N_{event}} \langle p_t \rangle_k \tag{5.23}$$

in which $\langle p_t \rangle_k$ denotes the average transverse momentum of event $k$, and

$$\langle p_t \rangle_k = \frac{1}{N_k} \sum_{i=1}^{N_k} p_{ti} \tag{5.24}$$

In this case, there are two distinctions. The first distinction is the average transverse momentum per particle for each event must first be determined individually before averaging that value over all events in the same centrality class can be calculated. As specified in (5.19), the average transverse momentum of a particle is defined as

$$\langle p_t \rangle = \frac{\langle P_T \rangle}{\langle N \rangle} \tag{5.25}$$

where

$$\langle P_T \rangle = \int d^3\mathbf{p}\rho_1(\mathbf{p})p_t = \left\langle \sum_{i=1}^{N_k} p_{ti} \right\rangle \tag{5.26}$$

This is more accurate in terms of our theoretical explanation of momentum density (5.14). The second distinction between (5.19) and (5.21) is one of normalization. The denominator of (5.19) is determined independently, but the ratio $\frac{\mathcal{C}_k}{N_k(N_k-1)}$ is determined event by event in (5.21). We make this decision in (5.19) in order to retain the greatest amount of consistency feasible between (5.9) and (5.8), (5.10), and (5.11). Both (5.19) and (5.21) are plotted in figure 5.1 since they were computed using the identical PYTHIA events. It has been noted that there is excellent agreement.

In $pp$ and $AA$ collisions, positive values of $\langle \delta p_{t1} \delta p_{t2} \rangle$ have been seen in experiments at a variety of energies. [51, 72, 74] show that $\langle \delta p_{t1} \delta p_{t2} \rangle$ reduces with centrality, but that this fall does not follow $\frac{1}{\langle N \rangle}$. If $\langle \delta p_{t1} \delta p_{t2} \rangle$ falls in the same direction as $\frac{1}{\langle N \rangle}$, then the number $\left(\frac{dN}{d\eta}\right) \langle \delta p_{t1} \delta p_{t2} \rangle$ should be relatively flat. However, experimental measurements of $\left(\frac{dN}{d\eta}\right) \langle \delta p_{t1} \delta p_{t2} \rangle$ show a gradual increase from periphery to mid-peripheral collisions and a plateau as the collisions get more central. According to some researchers [51, 72], this increase might signify the start of critical fluctuations or the impact of insufficient thermalization [45].

$\langle \delta p_{t1} \delta p_{t2} \rangle$ is commonly reported as a relative dynamical correlation in experimental measurements.

$$\frac{\sqrt{\langle \delta p_{t1} \delta p_{t2} \rangle}}{\langle p_t \rangle} \tag{5.27}$$

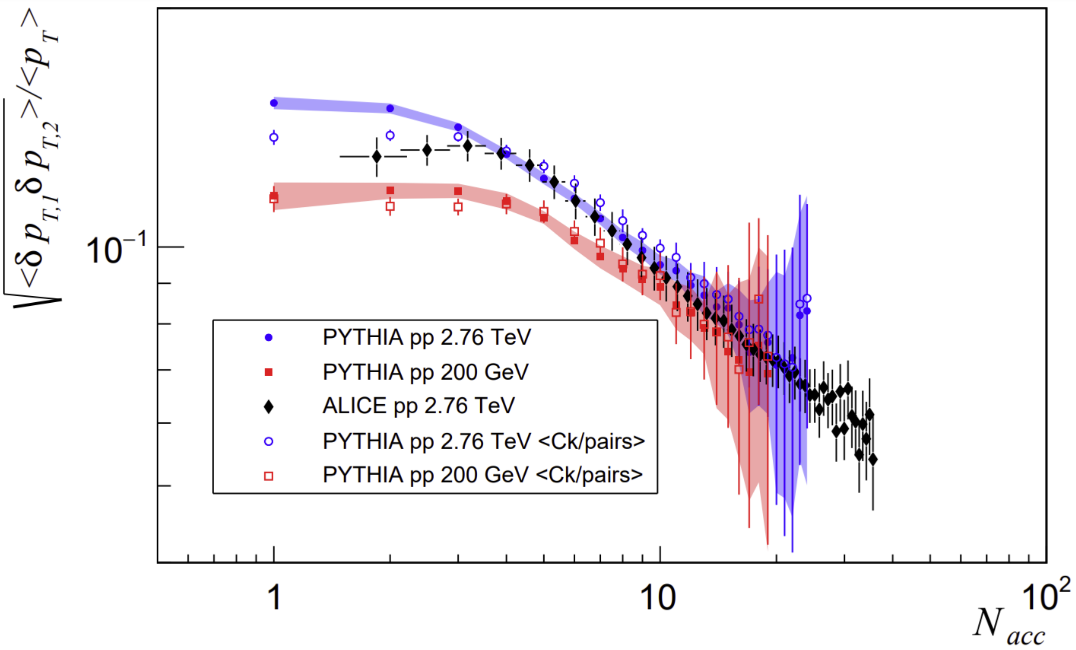

Figure 5.1: Equation (5.27) estimations from PYTHIA *pp* events (circles and squares) compared to ALICE measurements (solid diamonds) [72, 73]. (5.19) is represented by solid circles and squares, whereas open circles and squares are represented by equation (5.21).

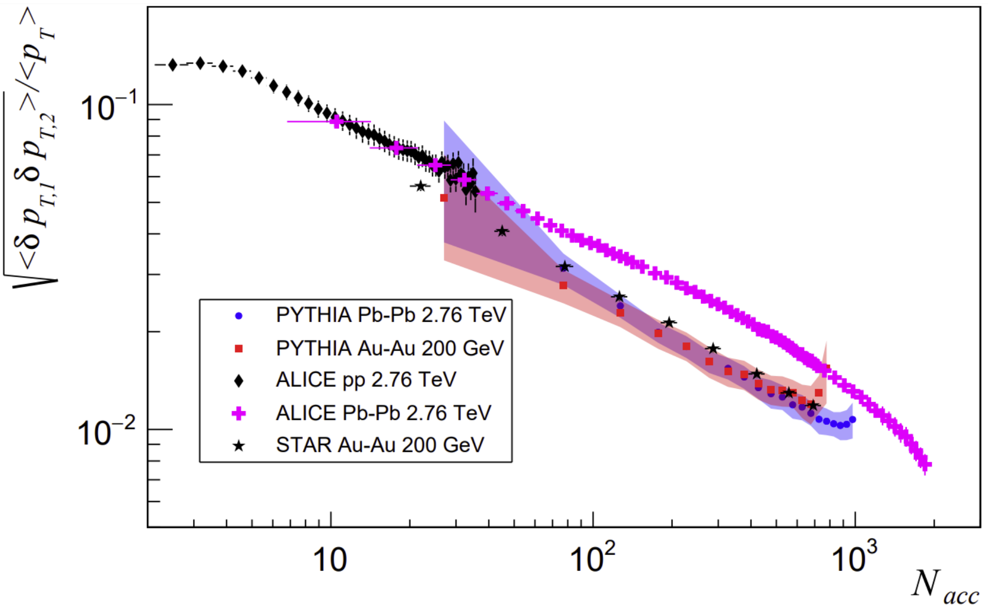

Figure 5.2: Equation (5.19) estimations from PYTHIA *AA* events were compared to measurements from ALICE *pp* and *PbPb* collisions [72, 73], as well as STAR *AuAu* collisions [74]. Multiplicity determines centrality.

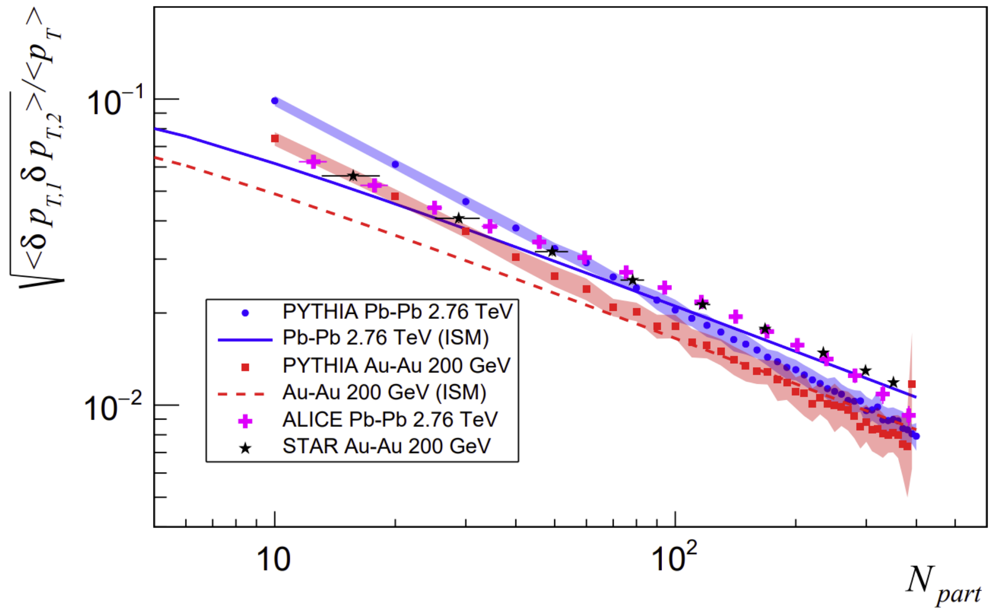

Figure 5.3: Equation (5.19) estimations from PYTHIA *AA* events were compared to measurements from ALICE *pp* and *PbPb* collisions [72, 73], as well as STAR *AuAu* collisions [74]. The number of participating nucleons determines centrality. The independent source model for wounded nucleons, Equation (6.27), is represented by solid lines .

it has no dimensions. It also rescales the growth of (5.19) such that it is determined by the total effect of correlations instead of the size of $\langle p_t \rangle$. The collision energy dependency of the observations is almost eliminated by this scaling [51, 72, 74]. We compute (5.27) using (5.19) and (5.25) from PYTHIA/Angantyr simulated events and compare it to experimental data in figures. 5.1, 5.2, and 5.3.

Experimental measurements of $\langle \delta p_{t1} \delta p_{t2} \rangle$ vary in terms of relative rapidity $\Delta\eta$ and relative azimuthal angle $\Delta\phi$, just as they do for $\mathcal{R}$ and $\mathcal{C}$. The ALICE collaboration measures $\frac{\langle \delta p_{t1} \delta p_{t2} \rangle (\Delta\eta, \Delta\phi)}{\langle p_t \rangle^2} = P_2(\Delta\eta, \Delta\phi)$, which has a particular ridge-like structure for charge independent correlations [60]. When using Fourier decomposition, the near-side ridge at $\Delta\phi$ equal to zero is not entirely explained, and the excess correlations in $\Delta\eta$ appear to be long-range in nature. $\langle \delta p_{t1} \delta p_{t2} \rangle$ correlations can be influenced by short-range phenomena such as resonance decays and jets; nevertheless, these effects alone are unable to adequately account for the excess long-range correlations observed in $P_2(\Delta\eta, \Delta\phi)$.

Several reasons have been postulated for these correlations. They include quark coalescence models [78], string percolation models in which clustered strings form colored sources [66], fluctuations in event entropy and size [79], and a boosted source model in which radial flow enhances correlations originating in initial state hotspots [14]. We argue that any explanation for these correlations should also address additional two-particle correlations derived from (5.18) such as (5.8), (5.10), and (5.11).

### 5.5 Multiplicity-momentum correlations

A novel observable $\mathcal{D}$, defined by (5.8), is used to investigate the relationship between transverse momentum and particle generation on an event-by-event basis. In chapter 6, we demonstrate that, in PYTHIA/Angantyr simulations, $\mathcal{D}$ is typically positive and has a magnitude that is comparable to $\langle \delta p_{t1} \delta p_{t2} \rangle$.

According to (5.8), $\delta p_t$ is defined by (5.20), and $\langle p_t \rangle$ is the average transverse momentum of a particle for a particular class of events with a certain centrality (5.25). (5.8) may be measured experimentally using the end state particle pair sum.

$$\mathcal{D} = \frac{1}{\langle N \rangle^2} \left\langle \sum_{i=1}^{N_k} \sum_{j\neq i, j=1}^{N_k} \delta p_{t,i} \right\rangle = \frac{1}{\langle N \rangle^2} \left\langle (N_k - 1) \sum_{i=1}^{N_k} \delta p_{t,i} \right\rangle \tag{5.28}$$

In order to comprehend this observable, we need to expand $\delta p_{t,i}$ in the intermediate term

$$\left\langle \sum_{i=1}^{N_k} \sum_{j\neq i, j=1}^{N_k} \delta p_{t,i} \right\rangle = \left\langle \sum_{i=1}^{N_k} \sum_{j\neq i, j=1}^{N_k} p_{t,i} \right\rangle - \left\langle \sum_{i=1}^{N_k} \sum_{j\neq i, j=1}^{N_k} \langle p_{t,i} \rangle \right\rangle \tag{5.29}$$

For any quantity $Y$, the event average can be expressed as $\langle Y \rangle = \frac{\sum_{k=1}^{N_{events}} Y_k}{N_{events}}$. When this occurs, $\langle N \rangle$ denotes the average number of particles in each event, and $\langle N(N-1) \rangle$ denotes the average number of particle pairs when autocorrelations are not taken into consideration.

Equation (5.29) can be written as

$$\left\langle \sum_{i=1}^{N_k} \sum_{j\neq i, j=1}^{N_k} \delta p_{t,i} \right\rangle = \langle N P_T \rangle - \langle P_T \rangle - \langle p_t \rangle \langle N(N-1) \rangle \tag{5.30}$$

Add and subtract $\langle N \rangle \langle P_T \rangle$ and use $\langle P_T \rangle = \langle p_t \rangle \langle N \rangle$ to equation (5.30), we find

$$\begin{aligned} \left\langle \sum_{i=1}^{N_k} \sum_{j\neq i, j=1}^{N_k} \delta p_{t,i} \right\rangle &= \langle N P_T \rangle - \langle N \rangle \langle P_T \rangle - \langle p_t \rangle \left( \langle N^2 \rangle - \langle N \rangle^2 \right) \\ &= Cov(N, P_T) - \langle p_t \rangle Var(N) \end{aligned}$$

where $Cov(N, P_T) = \langle NP_T \rangle - \langle N \rangle \langle P_T \rangle$ is the covariance between total transverse momentum and the multiplicity in a single event. $Var(N)$ is the event multiplicity variance. Now $\mathcal{D}$ can be written as

$$\mathcal{D} = \frac{Cov(N, P_T) - \langle p_t \rangle Var(N)}{\langle N \rangle^2} \tag{5.31}$$

The addition of any particle to an event will result in an increase in the total transverse momentum contained inside that event, because every particle carries a specific transverse momentum. As a result, there is a natural link between total $p_t$ and multiplicity that is dominated solely by fluctuations in multiplicity. Take note that this contribution is deducted from the rightmost phrase of the equation (5.31). Consequently, if multiplicity fluctuations are the only cause of multiplicity momentum correlations, $\mathcal{D}$ should be equal to zero.

Define

$$\mathcal{D}_E = \frac{Cov(N, E) - \epsilon Var(N)}{\langle N \rangle^2} \tag{5.32}$$

where $\epsilon = \frac{\langle E \rangle}{\langle N \rangle}$, we discover that $\mathcal{D}_E$ goes to zero when the energy per particle $\epsilon = \frac{\partial \langle E \rangle}{\partial \langle N \rangle}$ is satisfied.

In order to connect the energy and the transverse momentum, we consider

- Large transverse momentum of a particle ($p_t \gg m$). The transverse mass can be written as

  $$m_t = \sqrt{m^2 + p_t^2} = p_t \sqrt{(m/p_t)^2 + 1} \tag{5.33}$$

  we take the first order of taylor series of equation (5.33)

  $$m_t \approx p_t \tag{5.34}$$

- Near the mid-rapidity $y \approx 0$, we can write the energy as

  $$E_i = m_{t,i} \cosh y_i \tag{5.35}$$

  $$E_i \approx m_{t,i} \approx p_{t,i} \tag{5.36}$$

- The average total transverse momentum over all states is thus essentially equal to the average total energy.

$$\langle E \rangle \approx \langle P_T \rangle \tag{5.37}$$

The right side of equation (5.7) can be written as

$$\langle EN \rangle - \langle E \rangle \langle N \rangle = \langle P_T N \rangle - \langle P_T \rangle \langle N \rangle \tag{5.38}$$

equation (5.7) can be written as

$$\frac{\partial \langle E \rangle}{\partial \alpha} = \langle EN \rangle - \langle E \rangle \langle N \rangle = \frac{\partial \langle E \rangle}{\partial \langle N \rangle} \frac{\partial \langle N \rangle}{\partial \alpha} \tag{5.39}$$

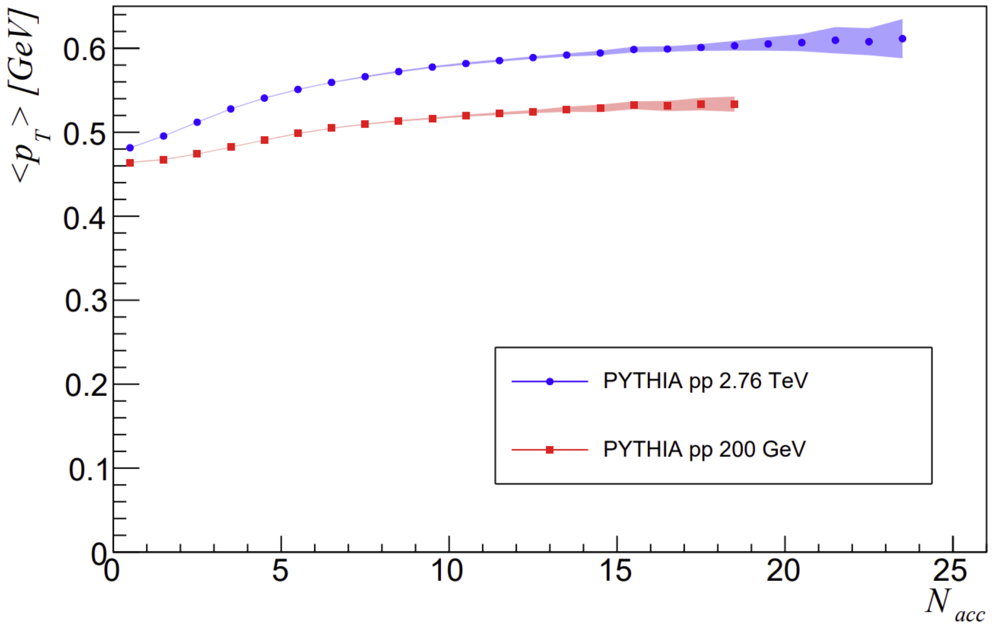

Figure 5.4: For *pp* collisions at various energy, average transverse momentum of a particle as a function of the reference of multiplicity. The PYTHIA error bars show statistical uncertainty.

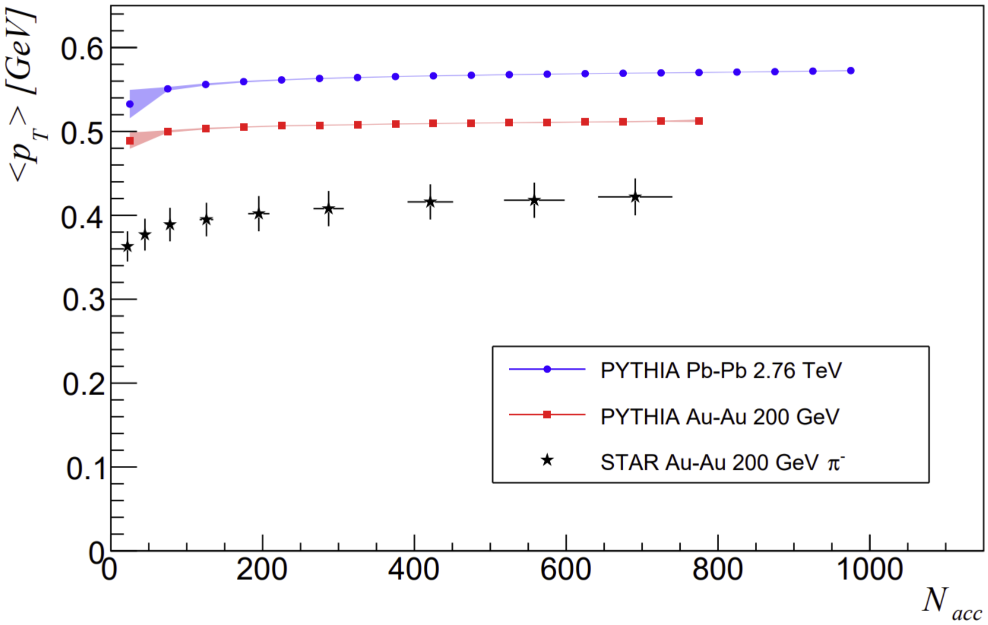

Figure 5.5: For certain $AA$ collision systems, average transverse momentum of a particle as a function of the reference multiplicity. On the PYTHIA results, error bars indicate statistical uncertainty. The STAR data is derived from [80].

We substitute $\frac{\partial\langle E\rangle}{\partial\langle N\rangle} = \frac{\partial\langle P_T\rangle}{\partial\langle N\rangle}$ in equation (5.39). $\langle p_t\rangle$ is consistent throughout a broad range of multiplicities, the definition of equation (5.25) yields $\frac{\partial\langle P_T\rangle}{\partial\langle N\rangle} \approx \langle p_t\rangle$. Using this information in (5.39) with (5.6), we find,

$$\langle P_T N\rangle - \langle P_T\rangle\langle N\rangle = \langle p_t\rangle \left(\langle N^2\rangle - \langle N\rangle^2\right) \tag{5.40}$$

Finally, we establish that $\mathcal{D} = 0$ by replacing (5.40) for (5.31).

A non-zero $\mathcal{D}$ can be caused by a variety of circumstances. Hadronization may cause the assumption that when $p_t$ much greater than $m$ holds for all particles to be violated. For example, in collision systems with $\sqrt{s} = 200GeV$, the average transverse momentum is around $\langle p_t\rangle \approx 0.5GeV$, which is obviously substantial when compared to the pion mass, but not when compared to the kaon or proton masses, according to some estimates. Heavy particles may cause the momentum multiplicity covariance to be skewed. When particle rapidities are greater than $|y| = 0.5$, the deviations from our $y = 0$ assumption become progressively large. If greater momentum particles, such as those with $p_t > 2GeV$, are produced at the expense of manufacturing fewer particles with average momentum, then the covariance $Cov(N, P_T)$ will become negative as a result. $Cov(N, P_T)$ will be positive if high momentum particles occur in conjunction with excess particles close to the average. The assumption $\langle p_t \rangle \approx \frac{\partial \langle P_T \rangle}{\partial \langle N \rangle}$ does not hold true if the transverse momentum per particle grows with increasing event multiplicity.

As seen in Figures 5.4 and 5.5, when we plot $\langle p_t \rangle$ against event multiplicity, we find that the average transverse momentum of a particle increases as the number of events increases. All collision systems and energies exhibit this phenomenon. reference [81] is an example of this. The transverse momentum and multiplicity covariance is positive, if only a slight one in this scenario. The production of jet particles or an increase in radial flow velocity in center collisions, as compared to peripheral collisions, are two possible explanations for this covariance. When $\langle p_t \rangle$ increases, it is thought to be a result of the multiple interaction model [82] and color reconnection [83], which have both been demonstrated in PYTHIA. A non-zero $\mathcal{D}$ shows a connection relating to particle creation and dynamics that is unique from $\mathcal{R}$, $\mathcal{C}$, and $\langle \delta p_{t1} \delta p_{t2} \rangle$ in each of these correlations. The contribution of correlations $\mathcal{D}$ to the other observables $\langle \delta p_{t1} \delta p_{t2} \rangle$ and $\mathcal{C}$ will be discussed in detail in the last section in this chapter.

### 5.6 Multiplicity fluctuations

Multiplicity fluctuations have been extensively investigated with the purpose of detecting the development of QGP (Quark-Gluon-Plasma). Net charge fluctuations are utilized to differentiate QGP from hadron gas [84, 85, 86, 87]. Such investigations depend on the concept of ″volume fluctuations″ to link event choices based on multiplicity to geometric description of the collision zone [88]. Other net charge fluctuation investigations search for substantial divergences that might indicate a QGP phase transition [75, 89, 90]. Inclusive multiplicity fluctuations have been connected to the system's isothermal compressibility [91, 92, 93], providing the midrapidity region can be characterized by the Grand Canonical Ensemble. (A research meant to be used as a base of statistical fluctuations originating from a hadron resonance in the Canonical Ensemble, Micro Canonical Ensemble, and Grand Canonical Ensemble can be found in this reference [94].) Net baryon fluctuations are utilized to detect small spots of chiral condensates in order to characterize events that indicate QGP production [95, 96]. All of these references make use of observables built from moments of inclusive or identifiable multiplicities of a particle [97, 98].

In this part, we will discuss elements of the multiplicity fluctuation observable (5.10) that is measured as

$$\mathcal{R} = \frac{\langle (N^2 - N) \rangle - \langle N \rangle^2}{\langle N \rangle^2} = \frac{\langle N^2 \rangle - \langle N \rangle^2 - \langle N \rangle}{\langle N \rangle^2}$$

so $\mathcal{R}$ can be written as

$$\mathcal{R} = \frac{Var(N) - \langle N \rangle}{\langle N \rangle^2} \tag{5.41}$$

We describe how $\mathcal{R}$ establishes an overall scale for each two particle correlation generated from the correlation function (5.18). As a result of this relationship, we investigate how the design of $\mathcal{R}$ results in a distinctive $\frac{1}{\langle N \rangle}$ behavior that effects the interpretation of each two particle correlation observable contained in this study.

Pruneau et al. show that the observable $\mathcal{R}$ is resilient to detection efficiency effects and acceptance restrictions for inclusive distributions in reference [98]. To demonstrate this, we begin by building (5.41) from the single particle distribution, $\rho_1$, and the pair distribution, $\rho_2$, respectively, using (5.3) and (5.15) and utilizing reasoning from both references [98] and [14]. Given $a$ and $b$ are arbitrary normalizations for $\rho_2$ and $\rho_1$ respectively such that

$$\rho_2 \rightarrow a\rho_2$$

$$\rho_1\rho_1 \rightarrow b\rho_1\rho_1$$

then (5.41) can be written as

$$\mathcal{R}_{acc} = \frac{a - b}{b} + \frac{a}{b}\mathcal{R} \tag{5.42}$$

It is possible for $\mathcal{R}$ to have a scale and offset that is dependent on the detector and collision mechanism, as well as the energy of the impact in case of $a \neq b$. If, on the other hand, $a$ and $b$ are equal, as is the case for detector tracking efficiency, then $\mathcal{R}_{acc} = \mathcal{R}$ is obtained. This is the motivating factor for the decision to normalize $\mathcal{R}$ by $1/\langle N \rangle^2$.

As a result, while looking at the rightmost definition of $\mathcal{R}$ in (5.41), you will see that in case of both terms have a scale of $\langle N\rangle$ in the numerator, then $\mathcal{R}$ will behave in a $\frac{1}{\langle N\rangle}$ manner. In this scenario, the multiplicity distribution follows binomial distribution or negative binomial distribution, which is the case in most cases. Independent particle production results in a Poisson statistics for the multiplicity distribution; the variance matches the mean, and $\mathcal{R} = 0$. Under chapter 6, we demonstrate that in an independent source model, the observables (all the observables) created in a manner similar to (5.10) trend in a manner similar to $\frac{1}{\langle K\rangle}$, where $K$ is the number of sources for a given event. These correlations are characterized by their $\frac{1}{\langle N\rangle}$ or $\frac{1}{\langle K\rangle}$ behavior, and we seek for deviations from this trend.

In order to identify critical fluctuations, the PHENIX collaboration calculated the scaled variance for the charged multiplicity

$$\omega = \frac{\sigma^2}{\mu} = \frac{\langle N^2\rangle - \langle N\rangle^2}{\langle N\rangle} \tag{5.43}$$

$\mu = \langle N\rangle$ is the average number of charged particles, and $\sigma^2$ is the variance [92]. A Negative Binomial Distribution ($NBD$) with a mean $\mu$ and a scaled variance $\omega = \frac{\mu}{k_{NBD}}+1$, where $K_{NBD}$ is a parameter, describes the distribution of heavy ion collision multiplicity. This parameter, $NBD$, is linked to (5.41) by

$$\mathcal{R} = \frac{\omega - 1}{\mu} = \frac{\sigma^2 - \mu}{\mu^2} = \frac{1}{k_{NBD}}. \tag{5.44}$$

The same $k_{NBD}$ will be found in subsets of an NBD that are randomly sampled with constant probability. If we consider an unlimited acceptance $\omega$ and $\mu$ represent the scaled variance and the mean multiplicity, respectively. Also, consider $\omega_{acc}$ and $\mu_{acc}$ to be the scaled variance and the mean from a fractional acceptance, respectively. In this case the scaled variance of fraction acceptance is $\omega_{acc} = 1 + \frac{\mu_{acc}}{k_{NBD}}$. With the use of $\mathcal{R} = \frac{1}{k_{NBD}}$ and the relationship (5.44) for $\mu_{acc}$ and $\omega_{acc}$, we can discover

$$\mathcal{R} = \frac{\omega_{acc} - 1}{\mu_{acc}} = \mathcal{R}_{acc}. \tag{5.45}$$

As previously stated, $k_{NBD}$ is same for both the fully accepted and the fractional accepted regions. In the case of $a = b$, this finding is consistent with (5.42) and establishes $\mathcal{R}$ as an appropriate measure of the strength of correlations.

According to equation (5.18), $\mathcal{R}$ sets the scale for all two-particle correlations that depend on the $r(\mathbf{p_1}, \mathbf{p_2})$ parameter, since correlations are connected to (5.41) by the multiplicity fluctuations (5.10). There are a number of factors that contribute to these correlations, starting with the energy deposition in the initial state. Perturbative QCD processes such as jets produce particles in a way that is fundamentally distinct from thermal $''$ hotspots $''$. Mesons and baryons, in particular, are constrained by the distinct energy scale. Fluctuations in the temperatures and quantity of hard scatterings at various hotspots also contribute to the changes in the (5.10).

Differential investigations of (5.41) resulted in the discovery of the ridge, which demonstrates that correlations extend to huge separations in rapidity [60, 99, 100, 101, 102], and the strength for the long-range correlations is determined by (5.18) [59, 103, 104]. There have been several hypotheses advanced to explain the appearance of the ridge, including flow or other correlations that have been modified by flow [14, 105]. However, this type of bulk correlation of particle momenta caused by the geometry of transverse collision that shifts the location of particles in the phase space and does not change the yields of particles.As previously established, a geometrical correlation on its own would result in a value of $\mathcal{R} = 0$ when the correlation is integrated.

It is possible to incorporate biases into the investigation of the centrality dependence of $\mathcal{R}$ (5.41) if the same particles are employed for measuring correlations and for measuring centrality. Although this will be covered in better detail later, it is useful to touch on one issue now. Imagine (5.41) was created by combining events with the same amount of particles. Then there's $\langle N \rangle^2 = \langle N^2 \rangle$ and

$$\mathcal{R} \to -\frac{1}{\langle N \rangle}. \tag{5.46}$$

This demonstrates a limiting behavior that occurs as a result of the use of multiplicity binning. It is necessary to distinguish between the multiplicity used to assess centrality and the multiplicity used to compute (5.41) centrality in order to prevent this effect. Aside from that, for a positive $\mathcal{R}$ to exist, the multiplicity variance must be greater than the number $\langle N \rangle$. The multiplicity variance must also change more quickly or more slowly than $\langle N \rangle$ with increasing centrality in order to deviate from a $\frac{1}{\langle N \rangle}$ distribution.

## 5.7 Transverse momentum correlations

As shown in (5.11), the transverse momentum correlations between two particles are quantifiable as

$$\mathcal{C} = \frac{\left\langle \sum_{i=1}^{N_k} \sum_{j\neq i}^{N_k} p_{t,i} p_{t,j} \right\rangle}{\langle N \rangle^2} - \frac{\langle P_T \rangle^2}{\langle N \rangle^2} \tag{5.47}$$

According to reference [106], the momentum correlation observable (5.47) was initially developed as part of an independent flow harmonic extraction approach for $\eta/s$, the shear viscosity-to-entropy density ratio. Relative pseudorapidity and azimuthal angle,$(\Delta\eta, \Delta\phi)$, $\mathcal{C}$ were measured for the first time by STAR [61]. In accordance with hydrodynamic flow calculations and expected AdS/CFT lower limit for $\eta/s = \frac{1}{4\pi}$ [107], this measurement limited $\eta/s$ to a range between 0.06 and 0.21. The measured range is mostly attributable to experimental systematic error, which may reduced by measuring the integral form for the rapidity width of (5.47) without the use of any fit functions like $\sigma_{\mathcal{C}}^2 = \int \mathcal{C}(\Delta\eta)\Delta\eta^2 d\Delta\eta$. ALICE is a significantly modified version of (5.47) defined as $G_2 = \frac{\mathcal{C}}{\langle p_t \rangle^2}$ [50, 108, 109, 110].

$$G_2 = \frac{\mathcal{C}}{\langle p_t \rangle^2} \tag{5.48}$$

In [63], the differential form of $G_2$ was used to detect harmonic Fourier coefficients in $\Delta\phi$ from the simulated data and compare those coefficients to harmonic flow coefficients $v_n$ obtained with the cumulant technique and a pseudorapidty gap $|\eta| = 0.7$.

The number density fluctuations and the transverse momentum fluctuations are sensitive to momentum correlations (5.47); both are required to address the diffusion of transverse momentum fluctuations because of shear viscosity. Shear viscous forces, according to reference [106], cause initial state momentum fluctuations to diffuse and dampen at the same time, resulting in an increase in the relative rapidity of correlations $\mathcal{C}$ during the collision lifespan. For $\mathcal{C}$, a centrality dependent assessment of $\mathcal{C}$'s relative rapidity width should reveal a monotonic rise due to the longer lifespan of central collisions than peripheral collisions. STAR was the first to see this phenomenon when they observed (5.47) differentiably in relative pseudorapidity and aziumuthal angle $\mathcal{C}(\Delta\eta, \Delta\phi)$ [61].

STAR discovered a differential correlation structure comparable to ridge, $\mathcal{R}(\Delta\eta, \Delta\phi)$, with broad in $\Delta\eta$ near-side peak at $\Delta\phi = 0$ and a flat in $\Delta\eta$ away-side peak at $\Delta\phi = \pi$. Because they can be (mainly) described by a Fourier cosine series, the double peaks in $\Delta\phi$ are generally interpreted as an indicator of hydrodynamic flow. On the near-side, however, there are correlations that are greater than the Fourier fit, and they reach their maximum at $\Delta\phi = \Delta\eta = 0$. A narrow $\Delta\eta$ profile associated with resonance decay or jet correlations is observed in peripheral collisions due to these excess correlations. According to [106], when collisions grow more central, the rapidity breadth of excess correlations increases.

Surprisingly, reference [61] discovered that the near side of $\mathcal{C}(\Delta\eta, \Delta\phi)$'s rapidity broadening was not Gaussian in nature. Rather than that, central collisions featured two $\Delta\eta$ peaks and a local minimal at $\Delta\eta = 0$. We explain in references [48, 111, 112] that non-Gaussian broadening is the signal of causal diffusion that is dependent on both shear viscosity and shear relaxation time.

In order to understand how (5.47) integrates number density fluctuations, we must write it interms of correlation function (5.18) to discover out (5.11). When (5.11) is compared to (5.10), it is clear that all multiplicity fluctuations in (5.47) are identical to those in (5.41), except that they are weighted by the average transverse momentum. This is significant because each particle possesses a certain amount of momentum, and hence correlations and diffusion of particles imply correlations and diffusion of momentum. Numerous momentum pairings are available in higher multiplicity events. Higher multiplicity events even have longer lifetimes, which allows for correlations to develop as a result of dynamic processes such as geometric flow. However, longer lifetimes also allow for more time for equilibration, that also destroys correlations.

In correlations of transverse momentum momentum fluctuations section, we discuss the transverse momentum correlations without number density fluctuations, but $\mathcal{C}$ was designed to investigate the transfer correlations of the transverse momentum between two points in QGP-from small rapidity to larger rapidity separations–and the density number fluctuations are a part of that process. Hot and cold zones are deposited across the collision volume in a kinetic theory or hydrodynamic model, each with a distinct local energy density and temperature. Viscous forces transfer energy density, particle number density, or momentum density from higher temperature locations to lower temperature places, causing movement toward equilibrium. Shear viscosity, interestingly, carries momentum perpendicular to the flow direction, therefore it distributes transverse momentum fluctuations throughout the longitudinal direction. Microscopic parton collisions and number density transmission can both spread that momentum.

To begin with, momentum correlations are formed as a result because pairs of particles come out of the same source and are often enforced by local conservation laws. Due to the fact that particles begin at the same spatial position, they have nearly the same dynamics and can form new correlations with one another and with the global event plane as a result of transverse expansion [14, 59, 113]. Furthermore, if correlations exist throughout a wide range of $|\Delta\eta| > 1-2$ unit rapidity ranges, causality necessitates that they arise from the earliest stages of the collisions [114]. Assuming that momentum correlations are formed as a result of particle pairs being emitted from the same source, the number of correlated pairs is generally directly proportional to the temperature generated by the source itself. There are more pairings, which means there is a stronger correlation between them. The differentiation between various sources is eliminated in equilibrium, lowering the correlation's strength.

### 5.8 Sum rule

In accordance with their common origin (5.18) and the concept of a transverse momentum fluctuation $\delta p_t$, the observables $\langle \delta p_{t1}\delta p_{t2}\rangle$, (5.19), $\mathcal{D}$, (5.28), $\mathcal{R}$, (5.41), and $\mathcal{C}$, (5.47) are mathematically connected (5.20). Eventually, we discover the connection (5.12).

We start with the definition (5.19) and work our way up to the argument $\langle \delta p_{t1}\delta p_{t2}\rangle$ in order to discover

$$\langle N(N-1)\rangle \langle \delta p_{t1}\delta p_{t2}\rangle = \left\langle \sum_{i=1}^{N_k}\sum_{j\neq i}^{N_k} p_{t,i}p_{t,j}\right\rangle - \left\langle \sum_{i=1}^{N_k}\sum_{j\neq i}^{N_k} \left(p_{t,i}\langle p_t\rangle + p_{t,j}\langle p_t\rangle\right)\right\rangle + \left\langle \sum_{i=1}^{N_k}\sum_{j\neq i}^{N_k} \langle p_t\rangle^2\right\rangle$$

we will work through the right side of the above equation term by term in order to find the relationship between the observables.

If we add and subtract $\langle P_T\rangle^2$ from the first term and after that compare it to (5.47), we will find

$$\left\langle \sum_{i=1}^{N_k}\sum_{j\neq i}^{N_k} p_{t,i}p_{t,j}\right\rangle + \langle P_T\rangle^2 - \langle P_T\rangle^2 = \langle N\rangle^2\mathcal{C} + \langle P_T\rangle^2 \tag{5.49}$$

If we compare (5.29) to (5.30) we will find

$$\left\langle \sum_{i=1}^{N_k}\sum_{j\neq i}^{N_k} p_{t,i}\right\rangle = \langle NP_T\rangle - \langle P_T\rangle = \left\langle \sum_{i=1}^{N_k}\sum_{j\neq i}^{N_k} p_{t,j}\right\rangle \tag{5.50}$$

and

$$\left\langle \sum_{i=1}^{N_k}\sum_{j\neq i}^{N_k} \langle p_t\rangle\right\rangle = \langle p_t\rangle\langle N(N-1)\rangle \tag{5.51}$$

from (5.50) we can write the second term as

$$\left\langle \sum_{i=1}^{N_k}\sum_{j\neq i}^{N_k} \left(p_{t,i}\langle p_t\rangle + p_{t,j}\langle p_t\rangle\right)\right\rangle = 2\langle p_t\rangle\left(\langle NP_T\rangle - \langle P_T\rangle\right) \tag{5.52}$$

substitute (5.49), (5.51) and (5.52), then add and subtract $2\langle p_t\rangle^2\langle N^2\rangle + 2\langle p_t\rangle\langle P_T\rangle\langle N\rangle$ to the main equation, we make use of definitions (5.31) and (5.41) in order to build

$$\langle N(N-1)\rangle\langle\delta p_{t1}\delta p_{t2}\rangle = \langle N\rangle^2\mathcal{C} - \langle N\rangle^2\langle p_t\rangle^2\mathcal{R} - 2\langle N\rangle^2\langle p_t\rangle\mathcal{D} \tag{5.53}$$

we can rewrite (5.41) as

$$(1+\mathcal{R}) = \frac{\langle N(N-1)\rangle}{\langle N\rangle^2} \tag{5.54}$$

substitute (5.54) in (5.53). we construct

$$\langle\delta p_{t1}\delta p_{t2}\rangle = \frac{\mathcal{C} - \langle p_t\rangle^2\mathcal{R} - 2\langle p_t\rangle\mathcal{D}}{(1+\mathcal{R})} \tag{5.55}$$

In the case of (5.55) the denominator is a result of the differing normalization of (5.19) when compared to (5.28), (5.41), and (5.47). The normalization of $\langle\delta p_{t1}\delta p_{t2}\rangle$ is left unchanged in order to allow for direct comparison with measured data. However, according to (5.55) the definition of $\langle\delta p_{t1}\delta p_{t2}\rangle$ must be (5.19) rather than (5.21). According to figure 5.1, the effect of this adjustment on measurement is small.

The fundamental finding of this study is that equation (5.55) is identical to equation (5.12). We can see from (5.55), that correlations of transverse momentum fluctuations may be read as multiplicity fluctuations with transverse momentum correlations removed $(-\langle p_t \rangle^2 \mathcal{R} + \mathcal{C})$ only if $\mathcal{D}$, the multiplicity momentum correlation, is zero.

Suppose that $\mathcal{D}$ is small, the discrepancy $-\langle p_t \rangle^2 \mathcal{R} + \mathcal{C}$ indicates the building of $\langle \delta p_{t1} \delta p_{t2} \rangle$. Notably, $\mathcal{C}$ would be at least an order of magnitude greater than $\langle \delta p_{t1} \delta p_{t2} \rangle$, indicating that multiplicity fluctuations, $\mathcal{R}$, to dominate momentum correlations, $\mathcal{C}$. In spite of this, the results of the $\langle \delta p_{t1} \delta p_{t2} \rangle$ measurements are non zero and positive, indicating that momentum correlations are formed by a physical mechanism that is not explained by multiplicity fluctuations. In order to explain that mechanism, any phenomenological or theoretical explanation must address both the origin of correlations and the reason why they are not eliminated by $\mathcal{D}$ or $\mathcal{R}$.

We compute $\mathcal{D}$ values in simulated PYTHIA events in chapter 6. We discover that $\mathcal{D}$ on the same order of magnitude compared to $\langle \delta p_{t1} \delta p_{t2} \rangle$, if not bigger. As a result, while measuring $\langle \delta p_{t1} \delta p_{t2} \rangle$ or $\mathcal{C}$, $\mathcal{D}$ should not be ignored.

$\langle \delta p_{t1} \delta p_{t2} \rangle$'s $\frac{1}{\langle N \rangle}$ (or divergence from $\frac{1}{\langle N \rangle}$) behavior can also be investigated (5.55). $\mathcal{R}$, in particular, has the most evident representation of the $\frac{1}{\langle N \rangle}$ trend; by construction, $\mathcal{C}$ and $\mathcal{D}$ should behave similarly. In an independent source model this is more clear. We put this behavior to the test with simulated occurrences.

Additionally, the impact of $\langle p_t \rangle$ is seen in (5.19) and (5.55). Given that $\langle p_t \rangle$ appears to increase in magnitude with multiplicity, it is a possible cause of divergence from $\frac{1}{\langle N \rangle}$ scaling for $\langle \delta p_{t1} \delta p_{t2} \rangle$ that is not attributable to critical events. Because $\langle p_t \rangle$ also grows as collision energy increases, tests validated a scaling (5.27) for $\langle \delta p_{t1} \delta p_{t2} \rangle$ that exhibits good agreement across a wide range of systems and energies [51, 72, 74]. Choices in centrality measure have some bearing on the quality of agreement. We can see in (5.55), how constituent correlation observables make a contribution to this scaling and how centrality determines this agreement. To avoid having to interpret the square root in

(5.27), we assume $\frac{\langle \delta p_{t1} \delta p_{t2} \rangle}{\langle p_t \rangle^2}$ and write (5.12) as a

$$\frac{(1{+}\mathcal{R}) \langle \delta p_{t1} \delta p_{t2} \rangle}{\langle p_t \rangle^2} = \frac{\mathcal{C}}{\langle p_t \rangle^2} - \mathcal{R} - \frac{2\mathcal{D}}{\langle p_t \rangle} \tag{5.56}$$

We can see from (5.56) that scaling with collision energy necessitates a consistent treatment of multiplicity fluctuation $\mathcal{R}$. Fortunately, when $\mathcal{R}$ and $\mathcal{C}$ are assessed using the similar methods, $\mathcal{R}$ compensates for $\mathcal{C}$'s centrality biases. Well that's what makes $\langle \delta p_{t1} \delta p_{t2} \rangle$ resistant to various definitions of centrality.

We may also investigate the transverse momentum correlations of two-particle by rewriting (5.56) as,

$$(1{+}\mathcal{R}) \langle \delta p_{t1} \delta p_{t2} \rangle + 2 \langle p_t \rangle \mathcal{D} + \langle p_t \rangle^2 \mathcal{R} = \mathcal{C}. \tag{5.57}$$

Different physical impacts on momentum correlations are distinguished by Equation (5.57). The $\mathcal{R}$ term denotes the contribution from multiplicity fluctuations alone (including volume fluctuations). This is by far the most significant contribution to $\mathcal{C}$. For example, in this case, the difference between $\mathcal{R}$ and $\mathcal{C}$ may be measured. $\mathcal{C}$ is influenced by factors such as viscosity, which are represented by the existence of $\langle \delta p_{t1} \delta p_{t2} \rangle$. Similarly, the existence of $\mathcal{D}$ indicates how the mechanism that links total transverse momentum-multiplicity is influencing $\mathcal{C}$ event by event.

The $G_2(\Delta\eta, \Delta\phi) = \frac{\mathcal{C}(\Delta\eta,\Delta\phi)}{\langle p_t \rangle^2}$ differential quantity is measured by the ALICE consortium [50, 108, 109, 110]. To locate the integrated version, use (5.56) and (5.48)

$$G_2 = \frac{(1{+}\mathcal{R}) \langle \delta p_{t1} \delta p_{t2} \rangle}{\langle p_t \rangle^2} + \mathcal{R} + \frac{2\mathcal{D}}{\langle p_t \rangle} \tag{5.58}$$

However, each of the terms can also be assessed differently in addition to the others. For example, in reference [60], the numbers $\mathcal{R}(\Delta\eta, \Delta\phi)$ and $P_2(\Delta\eta, \Delta\phi) = \frac{\langle \delta p_{t1} \delta p_{t2} \rangle (\Delta\eta,\Delta\phi)}{\langle p_t \rangle^2}$ are measured in the same way. $G_2(\Delta\eta, \Delta\phi)$ can be tested empirically by measuring $\frac{\mathcal{D}(\Delta\eta,\Delta\phi)}{\langle p_t \rangle}$ and comparing it to the calculated value (5.58).

Finally, multiplicity fluctuations, $\mathcal{R}$, dictate the scale of correlations at the underlying level, (5.18) which is governed by particle production processes, volume fluctuations, and perhaps phase change fluctuations. When we talk about momentum correlations, $\mathcal{C}$, we are referring to how the initial state correlations survive to the end state particle $p_t$, as well as how transverse momentum can be transported across the collision volume by forces such as shear viscosity. A correlation between total transverse momentum and multiplicity for each event is represented by $\mathcal{D}$. Equation (5.31) reveals that these correlations are greater than those resulting from random multiplicity fluctuations, and that $\mathcal{D}$ is consequently associated with particle production. As an added bonus, the absence of correlations $\mathcal{D}$ might indicate equilibrium while the augmentation of $\mathcal{D}$ could indicate the presence of the QGP critical point. The correlations of transverse momentum fluctuations, $\langle \delta p_{t1} \delta p_{t2} \rangle$, have a variety of theoretical interpretations, including temperature variations and boosted hot spots. A significant finding is that the outcomes (5.12), (5.55), (5.56), (5.56), or (5.58) show that a theoretical or experiential explanation with one of the observables $\mathcal{R}$ , $\mathcal{D}$ , $\mathcal{C}$ , or $\langle \delta p_{t1} \delta p_{t2} \rangle$ may be examined by addressing each of the other observables in turn. Similarly, when all four observables (5.19), (5.28), (5.31), and (5.47) are measured simultaneously in the experiments, equation (5.12) serves as a validation tool for each measurement as well as a way to explicitly differentiate multiplicity fluctuations from other correlation processes when searching for critical phenomena.

# CHAPTER 6 INDEPENDENT SOURCE MODEL (ISM)

The independent source model is critical in our study because it allows us to scale our pp collision results to AA collisions. Nuclear collisions, according to this hypothesis, are a superposition of individual proton-proton collisions. However, this ignores hadron rescattering, implying that charged particle pairs will only be associated if they are created in the same collision.

We calculate the observables (5.8), (5.9), (5.10), and (5.11) in this chapter using an independent source model. Equations (6.13), (6.17), (6.19), and (6.22) all support the $\frac{1}{\langle N\rangle}$ dependency of the observables if the overall multiplicity is the sum of the multiplicities of the individual sources. Additionally, Equations (6.13) and (6.17) demonstrate that source fluctuations can dominate $\mathcal{R}$ and $\mathcal{C}$. This shows that these observables can be utilized to discriminate across systems with fundamentally different intial states and particle production mechanisms.

There are numerous distinct physical mechanisms that might generate particle sources, but for the sake of simplicity, we will only examine the wounded nucleon model to test. The discrepancy between the PYTHIA/Angantyr results for nucleon nucleon collisions and our computation of wounded nucleons is most likely related to the Angantyr nucleon-nucleon superposition model and our use of simple participant nucleon sources. Interestingly, among all the observables, $\mathcal{D}$ appears to be the most sensitive to this change.

Additionally, we demonstrate that (5.12) may be utilized to discern between the centrality trends of $\mathcal{C}$ and $\mathcal{R}$. Even while $\mathcal{R}$ is usually constant or lowering as a function of $N_{part}$, $\mathcal{C}$ exhibits a tiny non-monotonic rise when the number of participants decreases. We see that this increase is related to the contributions of $\langle\delta p_{t1}\delta p_{t2}\rangle$ and $\mathcal{D}$ to momentum correlations, and we urge for comparable measurements in real experimental systems to corroborate our findings.

## 6.1 Observables in ISM

Independent source models ignore interactions between the emitted particles from distinct sources and assume that nuclear collisions are made up of a superposition of independent particles from each source. A variable number of sources are associated with each event, and each source has momentum distribution of particles and a fluctuating multiplicity associated with it. We'll go through how the observables described in sections 5.4, 5.5, 5.6, and 5.7 are affected by both forms of fluctuation in this part. Reference [14] has a similar explanation, however it only covers $\mathcal{R}$ and $\langle \delta p_{t1} \delta p_{t2} \rangle$.

In our independent source model, a single collision event is defined as the total of $K$ independent particle sources. A momentum distribution is used to represent each source. $\hat{\rho}_1(\mathbf{p})$ normalized in such a way that $\mu = \int d^3\mathbf{p}\hat{\rho}_1(\mathbf{p})$ denotes the average multiplicity per source. The average particle distribution among sources may be seen by imagining a large number of sources, each emitting $n_k$ particles, running from $k = 1, 2, ..., N_{sr}$. The average number of particles from each source is then calculated as

$$\bar{n} = \frac{1}{N_{sr}} \sum_{k=1}^{N_{sr}} \sum_{i=1}^{n_k} 1 \tag{6.1}$$

In case $N_{sr}$ tends to infinity, then the average multiplicity per source can be written as

$$\mu = \int d^3\mathbf{p}\hat{\rho}_1(\mathbf{p}) \tag{6.2}$$

Where $\rho_1$ in equation (6.2) is represent the particle momentum distribution for each source in the limit of a continuum of all potential sources and the overbar in equation (6.1) represents an average over all sources. That's when the variance is $\sigma^2 = (\bar{n^2}) - \bar{n}^2$ and the mean is $\bar{n} = \mu$ for each source multiplicity. The distribution of pairs particle released from a single source is also similar and can be written as

$$\overline{n(n-1)} = \frac{1}{N_{sr}} \sum_{k=1}^{N_{sr}} \sum_{i=1}^{n_k} \sum_{j=1}^{n_k} 1 \tag{6.3}$$

In case of $N_{sr}$ tends to infinity we found

$$\mu^2 - \mu + \sigma^2 = \int \int d^3\mathbf{p}_1 d^3\mathbf{p}_2 \hat{\rho}_2(\mathbf{p}_1, \mathbf{p}_2) \tag{6.4}$$

$\hat{\rho}_2$ denotes the particle pair distribution for a single source.

The event averaged momentum distributions of singles and pairs

$$\rho_1 = \langle K \hat{\rho}_1(\mathbf{p}) \rangle \tag{6.5}$$

$$\rho_2 = \langle K\hat{\rho}_2(\mathbf{p}_1, \mathbf{p}_2) + K(K-1)\hat{\rho}_1(\mathbf{p}_1)\hat{\rho}_1(\mathbf{p}_2)\rangle \tag{6.6}$$

The average across all events is shown in angled brackets, but every event has $K$ independent sources. The event multiplicity is defined by Equation (6.5) as a combination of $K$ sources.

$$\langle N\rangle = \mu \langle K\rangle \tag{6.7}$$

According to Equation (6.6), particle pairings are composed of the sum of pairs from each of the $K$ separate sources, each of which contains $\hat{\rho}_2(\mathbf{p}_1, \mathbf{p}_2)$ pairs, with the sum of pairs in which one particle that comes from the pairs is from one source and the second particle is from another source. Assuming that there are $K(K-1)$ sets of sources, this means that for every pair of sources, the particle pair distribution is $\hat{\rho}_1(\mathbf{p}_1)\hat{\rho}_1(\mathbf{p}_2)$. The average number of particle pairs per event is thus

$$\langle N(N-1)\rangle = \mu^2 \left\langle K^2\right\rangle + \langle K\rangle \left(\sigma^2 - \mu\right) \tag{6.8}$$

We will start with multiplicity-fluctuation observable, $\mathcal{R}$, we find

$$\mathcal{R} = \frac{1}{\langle N\rangle^2}\int\int d^3\mathbf{p}_1 d^3\mathbf{p}_2 r_{12} = \frac{1}{\langle N\rangle^2}\int\int d^3\mathbf{p}_1 d^3\mathbf{p}_2(\rho_2 - \rho_1\rho_1) \tag{6.9}$$

where in (6.9) we used equation (5.10) and (5.18). Substitute equation (6.5) and (6.6) in (6.9), we find

$$\mathcal{R} = \left[\frac{1}{\langle N\rangle^2}\int\int(\hat{\rho}_2 - \hat{\rho}_1\hat{\rho}_1)\langle K\rangle + \frac{1}{\langle N\rangle^2}\int\int\left(\left\langle K^2\right\rangle - \langle K\rangle^2\right)\hat{\rho}_1\hat{\rho}_1\right] d^3\mathbf{p}_1 d^3\mathbf{p}_2 \tag{6.10}$$

substitute (6.2), (6.4) and (6.7) in equation (6.10). The first right term in equation (6.10) can be written as

$$\frac{1}{\langle N\rangle^2}\int\int(\hat{\rho}_2 - \hat{\rho}_1\hat{\rho}_1)\langle K\rangle\, d^3\mathbf{p}_1 d^3\mathbf{p}_2 = \frac{\sigma^2 - \mu}{\langle K\rangle \mu^2} = \frac{\mathcal{R}_{sr}}{\langle K\rangle} \tag{6.11}$$

where $\mathcal{R}_{sr}$ is the arithmetic equivalent of (5.41) for sources when an ensemble among all possible independent sources is averaged.

For the second right term of equation (6.10) we find

$$\frac{1}{\langle N\rangle^2}\int\int\left(\langle K^2\rangle - \langle K\rangle^2\right)\hat{\rho}_1\hat{\rho}_1 d^3\mathbf{p}_1 d^3\mathbf{p}_2 = \frac{\langle K^2\rangle - \langle K\rangle^2}{\langle K\rangle^2} \tag{6.12}$$

The variance of $K$ in the equation (6.12) describes the event-by-event variability in the number of sources. Because the sources are assumed to be independent, this variance approaches Poisson statistics, which means that $\langle K\rangle = \langle K^2\rangle - \langle K\rangle^2$, and therefore fluctuations (6.10) are reduced by $\frac{1}{\langle K\rangle}$.

We can find the multiplicity fluctuations in independent source model by substituting (6.11) and (6.12) in (6.10)

$$\mathcal{R} = \frac{\mathcal{R}_{sr}}{\langle K\rangle} + \frac{\langle K^2\rangle - \langle K\rangle^2}{\langle K\rangle^2} \tag{6.13}$$

For two-particle transverse momentum correlations, $\mathcal{C}$, we will define the following

- Total average transverse momentum for each source can be written as

  $$\bar{P}_T = \int p_t\hat{\rho}_1 d^3\mathbf{p} = \frac{\langle P_T\rangle}{\langle K\rangle} \tag{6.14}$$

  where $\langle P_T\rangle$ is the average for the total transverse momentum for events.

- By substituting (5.25) for (6.7), the event averaged transverse momentum of a particle is equivalently expressed as

  $$\langle p_t\rangle = \frac{\bar{P}_T}{\mu} \tag{6.15}$$

- Transverse momentum for pair source defined as

  $$\int\int d^3\mathbf{p}_1 d^3\mathbf{p}_2 p_{t1}p_{t2}\hat{\rho}_2(\mathbf{p}_1,\mathbf{p}_2) = \mu^2\langle p_t\rangle^2 - \mu\langle p_t\rangle + \sigma^2_{P_T} \tag{6.16}$$

  where $\sigma^2_{P_T}$ is the variance of the total transverse momentum of each source, which is equal to $\overline{P_T^2} - \bar{P}_T^2$

The transverse momentum correlations of two particle are defined by equation (5.11). Use equation (5.18) with (6.6), (6.5), (6.14), (6.15) and (6.16) we find

$$\mathcal{C} = \frac{\mathcal{C}_{sr}}{\langle K\rangle} + \langle p_t\rangle^2\left(\frac{\langle K^2\rangle - \langle K\rangle^2}{\langle K\rangle^2}\right) \tag{6.17}$$

where

$$\mathcal{C}_{sr} = \frac{\sigma^2_{P_T} - \mu \langle p_t \rangle}{\mu^2} \tag{6.18}$$

is the equivalent of equation (5.47) for sources.

Take note that both equations (6.13) and (6.17) have a comparable contribution from source number fluctuations. Since each source is independent of the others, the value of (6.17) decreases with $\frac{1}{\langle K \rangle}$ in the same way as (6.13). However, because the correlation function is weighted by $p_t$, momentum correlations (6.17) are sensitive to transverse expansion. The effects of anisotropic flow are completely avoided when $\mathcal{C}$ is measured using the definition in (5.11) rather than differentially in psedurapidity or relative azimuthal angle. As a result, we may use $\mathcal{C}$ to indicate the magnitude of the transverse momentum correlations induced by the fireball. A measured divergence from the expectations of the independent source model may indicate that the sources of the correlations are not independent, which would be the case in a partially or completely equilibrated system.

Multiplicity-momentum correlations, denoted by the letter $\mathcal{D}$, are defined as (5.8). We obtain by following the same technique as we did for $\mathcal{R}$ and $\mathcal{C}$

$$\begin{aligned}
\mathcal{D} &= \frac{1}{\langle N \rangle^2} \int\int d^3\mathbf{p}_1 d^3\mathbf{p}_2 (\rho_2 - \rho_1\rho_1)\delta p_t \\
&= \frac{1}{\langle N \rangle^2} \int\int \left(\rho_2 p_{t1} - \langle p_t \rangle \rho_2 - \rho_1\rho_1 p_{t1} + \langle p_t \rangle \rho_1\rho_1\right) d^3\mathbf{p}_1 d^3\mathbf{p}_2 \\
&= \frac{\langle K \rangle}{\langle N \rangle^2} \int\int \hat{\rho}_2 (p_{t1} - \langle p_t \rangle) d^3\mathbf{p}_1 d^3\mathbf{p}_2
\end{aligned}$$

where from the equation in the second line, the third and forth term equal to $\langle p_t \rangle \langle K \rangle^2 \mu^2$ with opposite signs. If we integrate the third line and follow the same steps as $\mathcal{R}$ and $\mathcal{C}$, we will find

$$\mathcal{D} = \frac{\mathcal{D}_{sr}}{\langle K \rangle} \tag{6.19}$$

where

$$\mathcal{D}_{sr} = \frac{\langle P_T \mu \rangle - \langle P_T \rangle \langle \mu \rangle - \langle p_t \rangle \sigma^2}{\mu^2} = \frac{Cov(P_T, \mu) - \langle p_t \rangle \sigma^2}{\mu^2} \tag{6.20}$$

is the equivalent of equation (5.28) when referring to sources rather than events.

Notably, because (5.28) is structured to exclude the impacts of multiplicity fluctuations, (6.19) does not rely on source fluctuations in the same way as $\mathcal{R}$ or $\mathcal{C}$ do. However, the three observables $\mathcal{C}$, $\mathcal{R}$, and $\mathcal{D}$ are still decreased by the inverse of the source count.

Finally, correlations between transverse momentum fluctuations are described as (5.9). If we go back to equation (5.18) with (6.5) and (6.6), we're good to find

$$\begin{aligned}\langle \delta p_{t1} \delta p_{t2} \rangle &= \frac{\left(\mathcal{C}_{sr} - \langle p_t \rangle^2 \mathcal{R}_{sr} - 2 \langle p_t \rangle \mathcal{D}_{sr}\right) \langle K \rangle}{\langle K \rangle \mathcal{R}_{sr} + \langle K^2 \rangle} && (6.21)\\ &= \frac{\langle \delta p_{t1} \delta p_{t2} \rangle_{sr}}{\langle K \rangle} \frac{(1+\mathcal{R}_{sr})}{(1+\mathcal{R})} && (6.22)\end{aligned}$$

where

$$(1+\mathcal{R}_{sr}) \langle \delta p_{t1} \delta p_{t2} \rangle_{sr} = \mathcal{C}_{sr} - \langle p_t \rangle^2 \mathcal{R}_{sr} - 2 \langle p_t \rangle \mathcal{D}_{sr} \qquad (6.23)$$

using the same rationale as in equation (5.12), except that the ensemble of all conceivable independent sources is averaged rather than the individual sources. (5.9) has a different denominator than the other observables in this study, but because $\langle \delta p_{t1} \delta p_{t2} \rangle$ is thoroughly investigated in the literature, this form is more suitable for direct compare to measured data. As a result, the effects of fluctuating independent sources are less obvious than the effects of the other observable variables. By reviewing (6.22) we can see that $\langle \delta p_{t1} \delta p_{t2} \rangle$ approximates $\frac{1}{\langle K \rangle}$ in the limit of very large $K$ and small $\mathcal{R}$.

## 6.2 Calculations of observables in pp collisions

If we assume that the source's origins are the nucleons of the participants in the collision, then the minimal source for any collision is two. Independent source correlations in proton-proton ($pp$) collisions can be represented by the calculations of the $\mathcal{R}_{sr}$, $\mathcal{C}_{sr}$, $\mathcal{D}_{sr}$, and $\langle \delta p_{t1} \delta p_{t2} \rangle_{sr}$ in proton-proton collisions. In this situation, proton-proton collisions always have $K$ equal to 2 and have never had a variance in the number of sources involved in the collision. As a result, we do have $\langle K^2 \rangle - \langle K \rangle^2 = 0$ in (6.13) and in (6.17). Using (6.13) as an example, we can see that $\mathcal{R}_{pp} = \frac{\mathcal{R}_{sr}}{2}$ is obtained for $K = 2$ participants in proton-proton collisions. When $K = N_{part}$ and $\mathcal{R}_{sr} = 2\mathcal{R}_{pp}$, $\mathcal{C}_{sr} = 2\mathcal{C}_{pp}$ , $\mathcal{D}_{sr} = 2\mathcal{D}_{pp}$ and $\langle \delta p_{t1} \delta p_{t2} \rangle_{sr} = 2 \langle \delta p_{t1} \delta p_{t2} \rangle_{pp}$ are used for $AA$ collisions, the result is as follows:

- Multiplicity fluctuations, substitute the conditions from $pp$ collisions into (6.13), we will find

$$\mathcal{R} = \frac{2\mathcal{R}_{pp}}{\langle N_{par}\rangle} + \frac{\left\langle N_{part}^2\right\rangle - \langle N_{part}\rangle^2}{\langle N_{part}\rangle^2} \tag{6.24}$$

- Transverse momentum correlations, substitute the conditions from *pp* collisions into (6.17), we will find

$$\mathcal{C} = \frac{2\mathcal{C}_{pp}}{\langle N_{par}\rangle} + \langle p_t\rangle^2 \left(\frac{\left\langle N_{part}^2\right\rangle - \langle N_{part}\rangle^2}{\langle N_{part}\rangle^2}\right) \tag{6.25}$$

- Multiplicity-momentum correlations, substitute the conditions from *pp* collisions into (6.19), we will find

$$\mathcal{D} = \frac{2\mathcal{D}_{pp}}{\langle N_{par}\rangle} \tag{6.26}$$

- Correlations of transverse momentum fluctuations, substitute the conditions from *pp* collisions into (6.22), we will find

$$\langle \delta p_{t1}\delta p_{t2}\rangle = \frac{2\,\langle \delta p_{t1}\delta p_{t2}\rangle_{pp}}{\langle N_{par}\rangle}\frac{(1+\mathcal{R}_{pp})}{(1+\mathcal{R})} \tag{6.27}$$

We ascribe all volume fluctuations in this work to source fluctuations. To illustrate how volume (source) fluctuations affect multiplicity fluctuations, consider that the variance of, $N_{part}$, the participants number in the numerator of (6.24) for the rightmost term follows Poisson statistics. Then $\left\langle N_{part}^2\right\rangle - \langle N_{part}\rangle^2 = \langle N_{part}\rangle$ and (6.24) can be written as

$$\mathcal{R} = \frac{2\mathcal{R}_{pp} + 1}{\langle N_{par}\rangle} \tag{6.28}$$

It should be noted that the contribution from real source correlations is indicated by the number $2\mathcal{R}_{pp}$. Then, if $2\mathcal{R}_{pp} = 1$, half of the multiplicity fluctuations are caused by actual correlations, while the other half are caused by source fluctuations. As long as $2\mathcal{R}_{pp}$ is less than one, fluctuations source contribute more to $\mathcal{R}$ than actual correlations. If $2\mathcal{R}_{pp}$ is greater than one, the contribution of source fluctuations to $\mathcal{R}$ is less than the contribution of actual correlations. We compute $\mathcal{R}_{pp}$ employing PYTHIA simulations, and we report the results in Table 6.1 for impact energies of $\sqrt{s} = 200GeV$ and $\sqrt{s} = 2760GeV$, respectively. When $\sqrt{s} = 200GeV$ is used, source fluctuations account for somewhat less than two-thirds of the total $\mathcal{R}$ . When $\sqrt{s} = 2760 GeV$ is used, source variations account for almost half of $\mathcal{R}$.

This dependency on source fluctuations is also seen in the transverse momentum correlations, (6.25). The Poissonian distribution from participant sources is represented by the following:

| Integrated values of observables using PYTHIA *pp* collision | | |
|---|---|---|
| $\sqrt{s}$ | 200 GeV | 2760 GeV |
| $\mathcal{R}_{pp}$ | $0.2731 \pm 7.58 \times 10^{-4}$ | $0.453 \pm 1.02 \times 10^{-3}$ |
| $\mathcal{C}_{pp}$ | $0.0842 \pm 2.20 \times 10^{-4}$ | $0.1738 \pm 4.84 \times 10^{-4}$ |
| $\mathcal{D}_{pp}$ | $0.01685 \pm 9.32 \times 10^{-5}$ | $0.0348 \pm 1.68 \times 10^{-4}$ |
| $\langle \delta p_{t1} \delta p_{t2} \rangle_{pp}$ | $0.00257 \pm 2.27 \times 10^{-5}$ | $0.00446 \pm 3.67 \times 10^{-5}$ |
| $\langle N \rangle_{pp}$ | $6.635 \pm 3.65 \times 10^{-3}$ | $8.453 \pm 8.10 \times 10^{-3}$ |
| $\langle p_t \rangle_{pp}$ | $0.4860 \pm 1.33 \times 10^{-4}$ | $0.5356 \pm 1.78 \times 10^{-4}$ |

Table 6.1: The calculations are performed using charged particles from the kinematic area and an $|\eta| < 1$ at 200 $GeV$ or $|\eta| < 0.8$ at 2760 $GeV$. Uncertainties are expressed as standard deviation of subgroup values.

$$\mathcal{C} = \frac{2\mathcal{C}_{pp} + \langle p_t \rangle^2}{\langle N_{par} \rangle}. \tag{6.29}$$

Source fluctuations and genuine correlations have equal contributions to transverse momentum correlations incase of $2\mathcal{C}_{pp} = \langle p_t \rangle^2$. Using values from Table 6.1, we find that for $200 GeV$, the contributions to $\mathcal{C}$ from genuine correlations and source fluctuations are about similar, but source fluctuations are somewhat bigger at $200 GeV$ and genuine correlations are slightly larger at $2760 GeV$. We'll look at collision energy dependency in the future.

### 6.3 Simulation results

The major purpose of this section is to estimate $\mathcal{D}$ and test the connection (5.12) using simulated collision events. We do not try to conduct a complete investigation comparing different collision dynamics methods using different simulation algorithms; this is something that will be addressed in our research. To keep things simple, we used PYTHIA 8.2 [115], which has a well-established description of pp collisions and contains the Angantyr model of nuclear collisions [116], which offers a baseline calculation based on wounded nucleons.

We are looking for values of the novel observable $\mathcal{D}$ that are not zero, as described by equations (5.8) or (5.31). $\mathcal{D}$ denotes a multiplicity-momentum correlation and, potentially, a deviation from the thermal equilibrium, as discussed in multiplicity-momentum correlations section. Additionally, we examine the $\frac{1}{\langle N \rangle}$ dependency of (5.8), (5.9), (5.10), and (5.11) when multiplicity is used as a centrality measurement. Disruption from this pattern indicates the presence of non-Poissonian particle generation, which means that correlations arise between particles emerging from separate sources, or that other correlation processes are at work.

When correlations are calculated using the moments of a distribution of multiplicity, centrality biases can be severe, much more so when the same particles used to generate the correlations can also be used to define centrality [117]. When assessing observable dependencies on multiplicity, we use the centrality approach described in reference [14] to eliminate centrality biases caused by volume fluctuations. Because of this procedure, one-particle-wide multiplicity bins may be created without experiencing the biases outlined at the conclusion of multiplicity-fluctuations Section in chapter 5.

The observables are computed using all charged particles in the region of $|\eta| < 0.5$, and the centrality is estimated using all charged particles in the remainder of the experimental rapidity acceptance range. We denote these acknowledged centrality-determining particles by the abbreviation $N_{acc}$. $N_{acc}$ is compared to STAR using charged particles in the range $0.5 < |\eta| < 1$. $N_{acc}$ is compared to ALICE using charged particles in the range $0.5 < |\eta| < 0.8$. We depict the average mid-rapidity multiplicity versus $N_{acc}$ in PYTHIA events in Figures (6.1) and (6.2). The acceptance discrepancy between ALICE and STAR explains why the slopes of the mid-rapidity multiplicities differ. This centrality measure even has the effect of changing two-particle correlation observables to three-particle correlations, as the correlation is calculated using two particles and $N_{acc}$ is determined using different particles. It is possible to take multiplicity trends at face value if the pseudorapidity distribution for a charged particles is essentially flat in the rapidity acceptance, in which case the correlation between the mid-rapidity regions and particles number in the centrality determining is effectively 1.

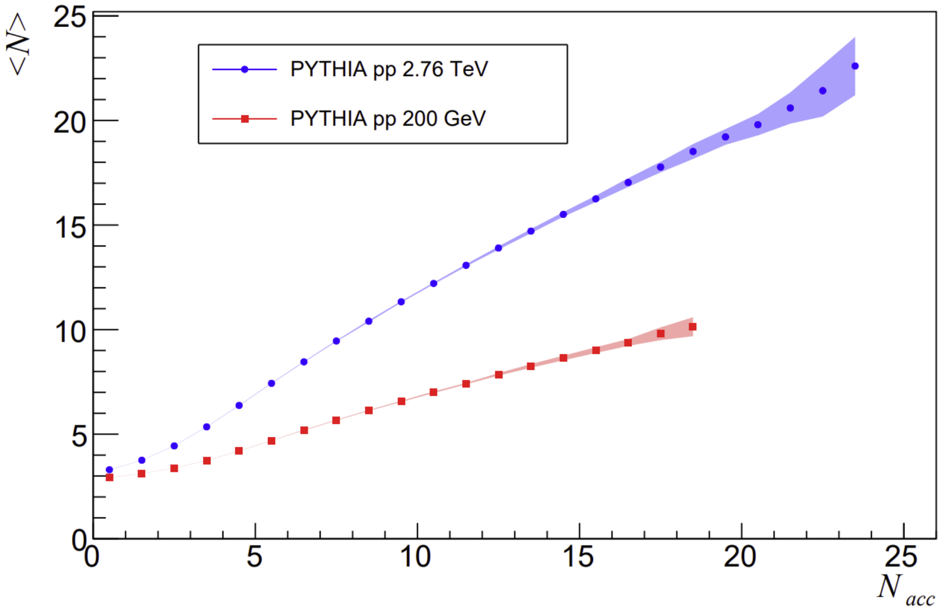

Figure 6.1: Variation of sub-group averaged multiplicity $\langle N \rangle$ versus the accepted multiplicity $N_{acc}$ for pp collsions at 200 $GeV$ and $2.76 TeV$ in the region $0.5 < |\eta| < 1$ and $0.5 < |\eta| < 0.8$ respectively.

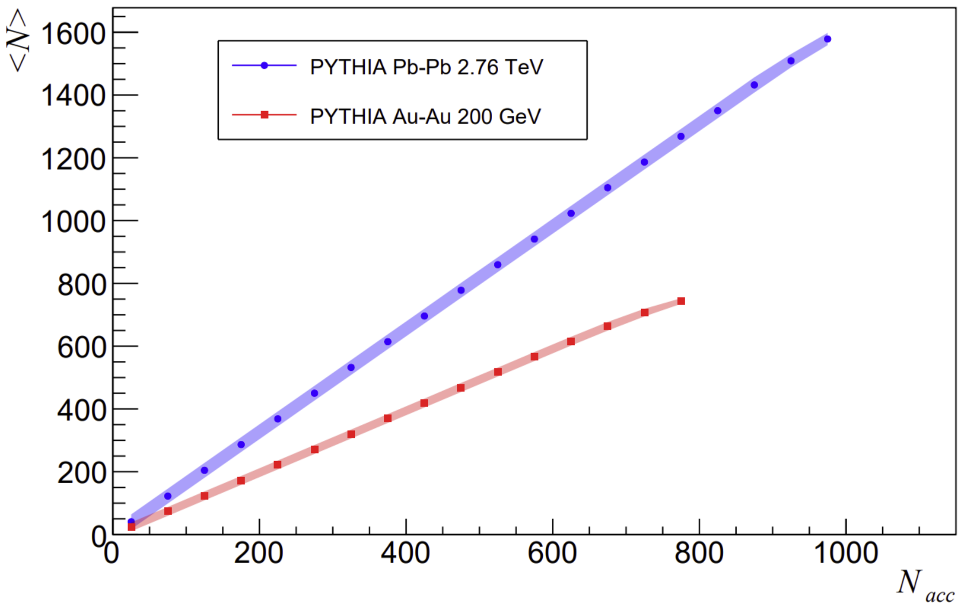

Figure 6.2: Variation of averaged sub-group mid-rapidity multiplicity $\langle N \rangle$ versus the accepted multiplicity $N_{acc}$ for AA collisions at 200 $GeV$ for Au-Au and $2.76 TeV$ for Pb-Pb in the region $0.5 < |\eta| < 1$ and $0.5 < |\eta| < 0.8$ respectively.

A nonlinear correlation between accepted multiplicity and the midrapidity multiplicity may cause some variation in correlation measurements that is not consistent with the predicted $\frac{1}{\langle N\rangle}$ trend. Nevertheless, as seen in Figures. 6.1 and 6.2 for pp and AA collisions, the average mid-rapidity multiplicity $\langle N\rangle$ tracks quite linearly with $N_{acc}$ for PYTHIA events.

Similarly to Reference [74], we estimate the uncertainty of observables correlation using the so-called ″subgroup″ technique. Our methodology divides the total set of events for a particular centrality class into Thirty subgroups and calculates all observables for each subgroup. After averaging each observable over all subgroups, the standard deviation is being used to quantify the uncertainty. When multiplicity is utilized to determine centrality in AA collisions, we average observable values over many multiplicity bins and then set the error band to match the standard deviation with those values.

As shown in Figures 5.4 and 5.5, we have calculated the average transverse momentum for each particle from PYTHIA events in a variety of proton-proton (pp) and nucleus-nucleus (AA) systems and energies. Both the centrality and sub-group methodologies mentioned above have been employed in this study to generate all of the PYTHIA simulation results presented in this thesis. Both graphs demonstrate an increase in $p_t$ for each particle as multiplicity rises. In a subsequent section, we shall argue that this is critical for understanding momentum-multiplicity correlations $\mathcal{D}$. The lower increase in AA collisions relative to pp collisions is very certainly a factor in the disparate magnitudes of $\mathcal{D}$ estimations from different collision systems.

Now we will estimate the observables $\mathcal{R}$, $\mathcal{D}$, $\mathcal{C}$, and $\langle\delta p_{t1}\delta p_{t2}\rangle$, as well as their mathematical connection (5.12), using PYTHIA simulations of AA and pp collision systems at various energies. We investigate the events that occur after (5.41), (5.47), (5.19), and (5.28) for each of the four observables. For gold-gold collisions at $\sqrt{s} = 200\ GeV$, we used $p_t$ in the range between 0.15 $GeV$ and 2 $GeV$ , and $|\eta|$ in the kinematic range less than 1, while for lead-lead collisions at $\sqrt{s} = 2.76\ TeV$, we choose $|\eta|$ less than 0.8. We plot the product of each of the four observables with the multiplicity $\langle N\rangle$ to find deviations from $\frac{1}{\langle N\rangle}$ behavior. It is possible that the results will remain constant with multiplicity if there is no divergence from the value $\frac{1}{\langle N\rangle}$; nevertheless, the magnitudes will be different.

(5.10) or (5.41) are used to determine multiplicity fluctuations, which are linked to volume fluctuations, $\mathcal{R}$. Figure 6.3(a) illustrates the results for $\langle N\rangle\mathcal{R}$ from a PYTHIA simulation of proton-proton collisions at $200GeV$ and $2.76TeV$. At smaller multiplicities, the variation from $\frac{1}{\langle N\rangle}$ behavior is most likely due to a slight variance in the overall multiplicity generated by these events. Likewise, values turn negative in the extremely low multiplicity zone. Consider that events with such a small number of particles in the rapidity zone defined by centrality also have a small number of particles in the midrapidity region. The variance of midrapidity is almost negligible in this scenario. As a result of the reasoning around equation (5.46), it is reasonable to assume negative values of $\mathcal{R}$. At higher multiplicities, the factor $\langle N\rangle\mathcal{R}$ is becoming more and more flat and the error band widens as the number of events decreases.

It's worth noting that in pp collisions the factor $\langle N\rangle\mathcal{R}$ at $\sqrt{s} = 2.76TeV$ decreases somewhat quicker than $\frac{1}{\langle N\rangle}$ with increasing multiplicity as compared to collisions at $\sqrt{s} = 200GeV$. It will be fascinating to see whether this effect is preserved at greater or lower collision energy for both simulation and experiment. Additionally, it is critical to note

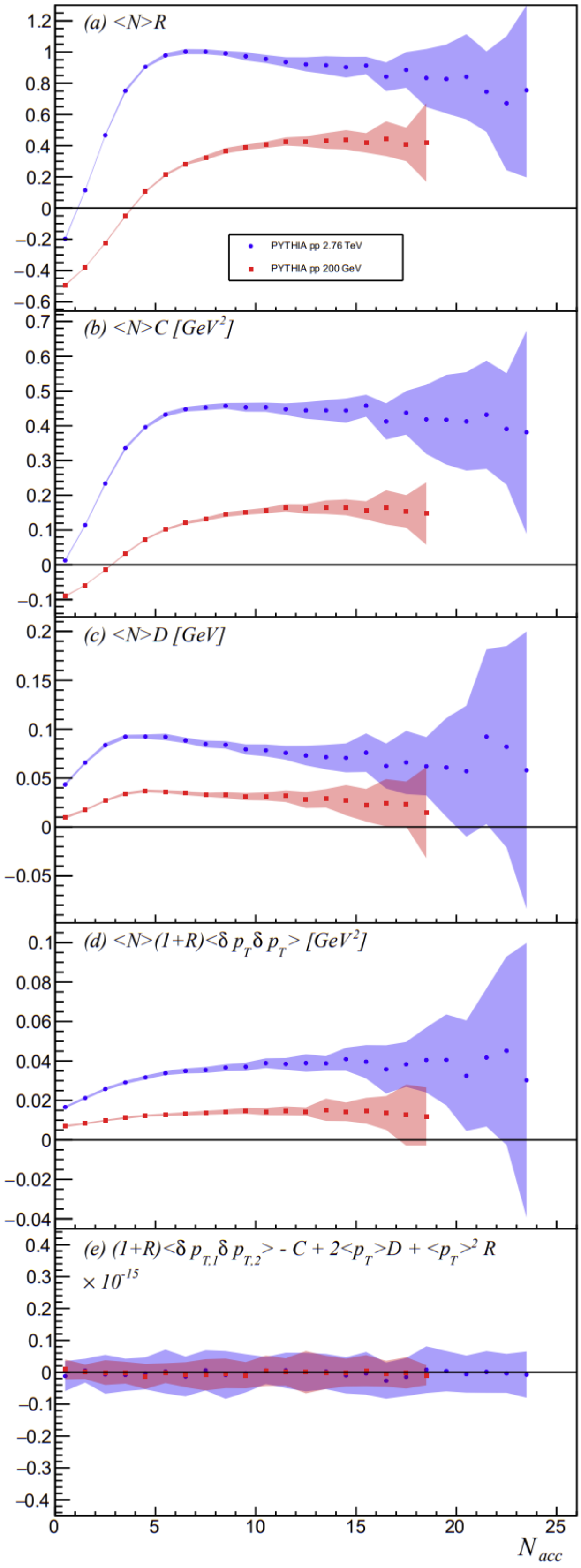

Figure 6.3: Observables (5.8), (5.9) ,(5.10) and (5.11) were calculated using PYTHIA pp collisions and scaled by the mid-rapidity multiplicity $\langle N \rangle$.

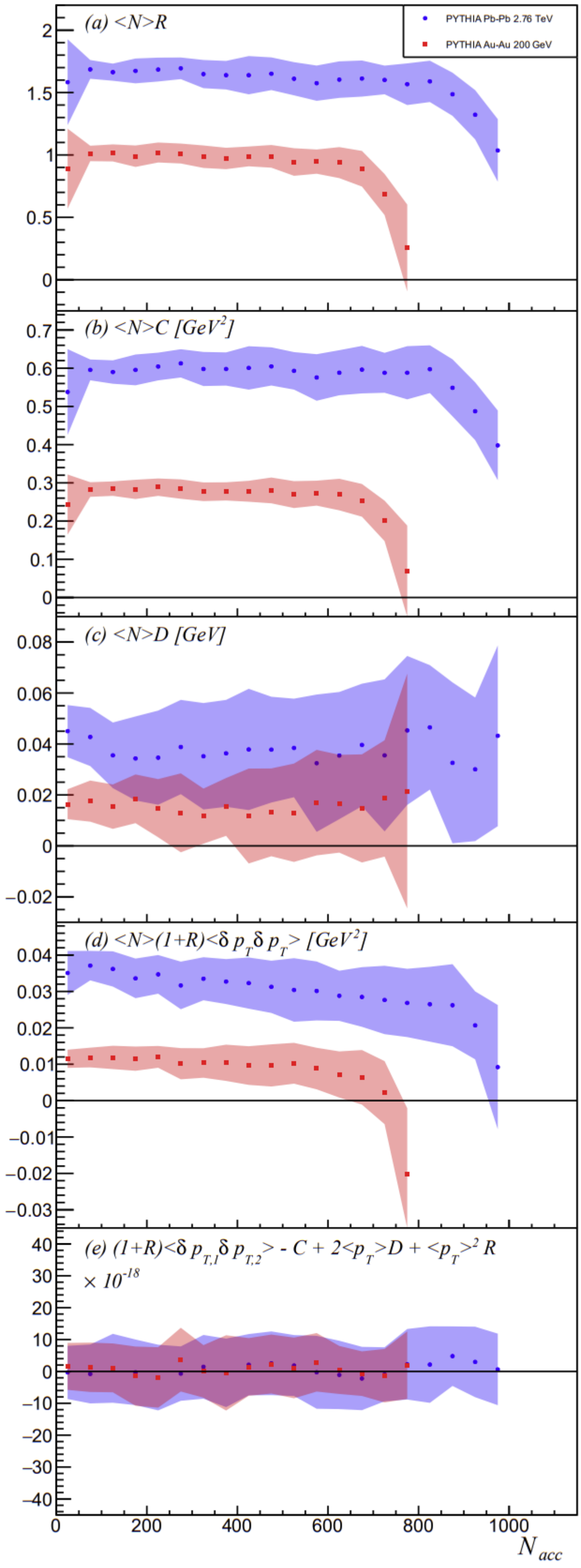

Figure 6.4: Observables (5.8), (5.9) ,(5.10) and (5.11) were calculated using PYTHIA/Angantyr AA collisions and scaled by the mid-rapidity multiplicity $\langle N \rangle$.

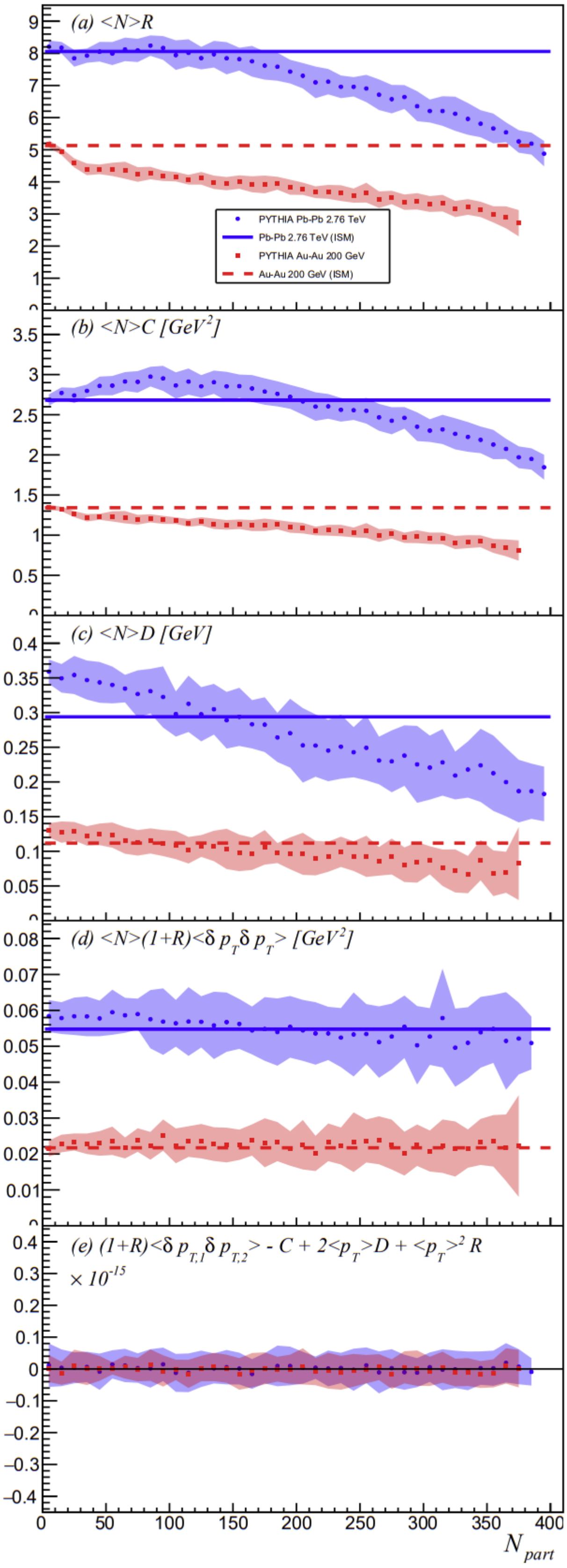

Figure 6.5: Observables (5.8), (5.9) ,(5.10) and (5.11) were calculated using PYTHIA/Angantyr AA collisions and scaled by the mid-rapidity multiplicity $\langle N \rangle$. The wounded nucleon model is shown by solid lines.

that $\langle N \rangle \mathcal{R}$ is greater than zero, indicating that particle production is not Poissonian and hence not independent. This reaffirms the fact that $\mathcal{R}$ quantifies a fundamental process of particle production. Distinction between experimental data and PYTHIA estimations may indicate the presence of different particle sources. In order to evaluate the commencement of QGP or jet impacts on particle production, it may be beneficial to conduct a comparison of different energies and collision systems

In Figure 6.4(a), the results of the PYTHIA/Angantyr simulation of Pb-Pb and Au-Au collisions at $\sqrt{s} = 2.76TeV$ and $\sqrt{s} = 200GeV$ are shown against multiplicity to highlight the effect of $\langle N \rangle \mathcal{R}$. When multiplicity is used to assess centrality, $\langle N \rangle \mathcal{R}$ seems to be constant in perhaps the most central points. The deviation seen in higher multiplicity events is almost certainly due to insufficient statistics. As a result of averaging the first several lowest multiplicity bins, where values may be tiny or negative for the same reasons as small or negative values arose in low multiplicity proton-proton collisions, the lowest multiplicity point drops to its lowest possible value. As a general rule, the almost constant value of $\langle N \rangle \mathcal{R}$ as a function of multiplicity is compatible with a superposition of the proton-proton sub-collision model.

Figure 6.5 (a) shows a plot of the same amount, $\langle N \rangle \mathcal{R}$, versus the number of participants ($N_{part}$), which is used to test the Independent Source Model (ISM). We depict (6.24) as dashed and solid lines on the figure, using participating nucleons as particle sources. Assuming the variance of $N_{part}$ in (6.24) is Poissonian, the rightmost term is reduced to $\frac{1}{\langle N_{par} \rangle}$. Additionally, we use PYTHIA to construct the "integrated" value $\mathcal{R}_{pp}$, which includes all pp events regardless of their centrality constraints. Table 6.1 contains values for proton-proton collisions at $\sqrt{s} = 2760\ GeV \equiv 2.76\ TeV$ and $\sqrt{s} = 200GeV$. We utilize the entire experimental rapidity acceptance to compute all observables when determining centrality with $N_{par}$, and the same is true for integrated values. Equation (6.24) closely matches the data when $N_{par} = 2$ on Figure. 6.5 (a), but deviates when $N_{par}$ increases. This might imply that the source value is dominated by low multiplicity events for pp collisions, or that participating nucleons are not a reliable predictor of all particle sources on their own.

Correlations of momentum, $\mathcal{C}$, are described by equations (5.11) or (5.47). Due to its comparable construction, it exhibits many of the same patterns in centrality as $\mathcal{R}$. $\mathcal{C}$ scales with both $\langle p_t \rangle^2$ and $\mathcal{R}$; the latter scaling may be seen by looking at the data (6.17). $\langle N \rangle \mathcal{C}$ is shown in Figures 6.3(b), 6.4(b), and 6.5(b). Except for Figure 6.5(b), centrality behaviors are generally correspond to those of $\langle N \rangle \mathcal{R}$. In comparing to our independent source model for wounded nucleons in lead-lead collisions at $\sqrt{s} = 2.76\,TeV$, $\langle N \rangle \mathcal{C}$ grows with peripheral collisions and reaches a maximum at $N_{part} \approx 100$. In $\langle N \rangle \mathcal{R}$, this increase is not observed for the almost same collision system. Furthermore, this peak is absent for $\langle N \rangle \mathcal{C}$ in gold-gold collisions with $\sqrt{s} = 200 GeV$.

The dependency of $\mathcal{C}$ on its centrality may be evaluated in the context of (5.58). $\langle N \rangle (1 + \mathcal{R}) \langle \delta p_{t1} \delta p_{t2} \rangle$ and $\langle N \rangle \mathcal{D}$ both surpass the wounded nucleon model estimate in the same location where $\langle N \rangle \mathcal{C}$ rises in Figure 6.5(b). Caution should be exercised when interpreting the peak in Figure. 6.5(b): when $\langle N \rangle \mathcal{C}$ is plotted against multiplicity as in Figure. 6.4(b), the peak behavior is not visible. As a result, we utilize these observations solely to highlight the utility of seeing correlation observables as a complimentary set with a mathematical relationship, such as (5.12).

The equations (5.9) or (5.19) define the correlations of the transverse momentum fluctuations, $\langle \delta p_{t1} \delta p_{t2} \rangle$. STAR and ALICE have both quantified a comparable form (5.21), typically referring to it as (5.27). In Figure. 5.1, we compare the estimated value of (5.27) for pp collisions to experimental data for pp collisions. In general, the two techniques (5.19) and (5.21) accord well. AA collisions provide similar findings, but they are excluded from Figure. 5.2 for clarity.

Figure 5.2 shows PYTHIA data compared to experimental AA data. Although there is considerable agreement with STAR data, there is a major discrepancy with ALICE data. This is most likely due to variations in how STAR and ALICE calculate multiplicity centrality; our method closely matches STAR's.

To demonstrate that $\langle \delta p_{t1} \delta p_{t2} \rangle$ is $\frac{1}{\langle N \rangle}$ dependent, we plot $\langle N \rangle (1 + \mathcal{R}) \langle \delta p_{t1} \delta p_{t2} \rangle$ in Figures 6.3(d), 6.4(d), and 6.5(d). As seen in sum rule section in chapter 5 and observables in ISM section, the factor $(1 + \mathcal{R})$ is necessary to rescale (5.19) such that it exhibits the same $\frac{1}{\langle N \rangle}$ trends like the other observables.

The PYTHIA values for $\langle N \rangle (1+\mathcal{R}) \langle \delta p_{t1} \delta p_{t2} \rangle$ in proton-proton collisions, as shown in Figure 6.3(d), are essentially flat except for slight fluctuations in peripheral collisions. As can be shown in Figure 6.4(d), the trend in AA collisions is a $\frac{1}{\langle N \rangle}$ except in the most center collisions which are statistically limited, as can be seen inside the error band. In compared to $\mathcal{R}$ or $\mathcal{C}$, $\langle \delta p_{t1} \delta p_{t2} \rangle$ has a lower influence from small fluctuations in low multiplicity. $\langle \delta p_{t1} \delta p_{t2} \rangle$ eliminates multiplicity fluctuations through construction (see the discussion after Equation (5.47) in Sum rule section in chapter 5). As a result, $\langle \delta p_{t1} \delta p_{t2} \rangle$ appears to be insensitive to centrality selection via participating nucleons or multiplicity. The results in Figure 6.5(d) of $\langle N \rangle (1+\mathcal{R}) \langle \delta p_{t1} \delta p_{t2} \rangle$ are also constant with respect to the number of participating nucleons, which is consistent with the wounded nucleon model, Equation (6.27).

The difference between the wounded nucleon model in Figure 5.3 and Figure 6.5(d) is most likely due to a combination of factors. To begin, the integrated value of of the average transverse momentum in pp collisions is utilized in conjunction with (6.27). $\langle p_t \rangle$ is the same for individual sources as it will be for entire event in the independent source model. In our basic wounded nucleon model, $\langle p_t \rangle_{pp}$ does not change, while $\langle p_t \rangle$ does in the dependent of the centrality measurement. Finally, the component $(1+\mathcal{R})$ in the denominator of (6.27) results in a deviation from the PYTHIA values. Figure 6.5(a) shows that $\mathcal{R}\int$ for our wounded nucleon model is greater than PYTHIA values, which is particularly the case in more central collisions.

The correlations between multiplicity and momentum, denoted by $\mathcal{D}$, are determined by equations (5.8) or (5.28). The purpose of this research is to generate interest in experimental measurements of $\mathcal{D}$. The initial estimations of $\langle N \rangle \mathcal{D}$ from PYTHIA AA and pp collisions are plotted in Figures 6.3(c), 6.4(c), and 16.5(c). Observations made immediately include the fact that $\mathcal{D}$ doesn't equal to zero and its positive. $\mathcal{D}$'s nonzero positive value is compatible with $\langle p_t \rangle$ computations. Consider, for example, Figure 5.4, where the average transverse momentum of each particle grows as the number of particles increases. This is a correlation between multiplicity and momentum.The substantial difference between $\langle N\rangle\,\mathcal{D}$ in pp and AA collisions might be explained by the fact that somehow the rate of growth of $p_t$ as a function of multiplicity is faster in pp collisions than in AA collisions for PYTHIA simulations.

The flatness of the factor $\langle N\rangle\,\mathcal{D}$ in relation to centrality confirms the $\frac{1}{\langle N\rangle}$ dependency. Surprisingly, pp collisions have a slight negative slope as multiplicity increases, implying a quicker than $\frac{1}{\langle N\rangle}$ decline as multiplicity increases. This slope appears to rise as collision energy increase from 200 $GeV$ to 2.76 $TeV$. We want experimental evidence for this phenomenon over a broader range of collision energy.

As seen in Figure 6.5(c), peripheral collisions have larger $\mathcal{D}$ values than those predicted by our wounded nucleon model when centrality is dictated by participating nucleons. This might simply be a difference between our independent source model, which uses just participant nucleons as sources, and the PYTHIA/Angantyr model. If such is the case, then $\mathcal{D}$ is the observable that is most sensitive to the difference.

Finally, $\mathcal{D}$ may also be affected by the medium's thermalization. Similarly, as demonstrated in Reference [45], if $\langle \delta p_{t1}\delta p_{t2}\rangle$ can be utilized to quantify partial thermalization, then $\mathcal{D}$ and $\mathcal{C}$ may impose further limitations on the model. This is something we'll take up in the future.

## 6.4 Summary

As a conclusion, we show that the same parent correlation function is used to create two-particle multiplicity fluctuations ($\mathcal{R}$), transverse momentum correlations ($\mathcal{C}$), correlations of the transverse momentum fluctuations ($\langle \delta p_{t1}\delta p_{t2}\rangle$), and multiplicity-momentum correlations ($\mathcal{D}$) and these four observabels are mathematically linked together by equation (5.12). These observables and their relationship to PYTHIA/Angantyr simulated collision events at 200 $GeV$ and 2.76 $TeV$ have been estimated energy of collision. A novel observable, multiplicity-momentum correlations, is computed for the first time in this paper.

We argue that when observables and their mathematical relationships are observed or calculated concurrently, they can reveal more information than the total of the individual measurements. The Measurements of these observables across a broad range of energies and collision systems may yield essential information regarding the mechanics of initial state particle production in hadronic collisions, as well as the following equilibration process throughout the collision medium.

# CHAPTER 7 OBSERVABLES IN PARTIAL THERMALIZATION

When dealing with a macroscopic or many-body system, knowing everything about it is nearly difficult. Using classical physics as an example, $6N$ real numbers are necessary to completely characterize an $N$-body system. This is because each particle required three real numbers to define its location and three real numbers to define its momentum. Newton's equations of motion may be solved in theory for the future evolution of each particle if the initial circumstances for each particle are known in advance. Now if we assume we have a huge number of molecules/particles its difficult or impossible to solve. For example, a gram mole of gas has $10^{23}$ molecules, which means that solving huge numbers of differential equations simultaneously is nearly impossible if $N$ is very large. Additionally, it is not necessary for practical reasons. A macroscopic system may be described by macroscopic variables, such as volume, pressure, temperature,energy etc... and the system's dynamics can then be expressed as a function of these macroscopic variables. If an isolated many-body system for some assumptions, is left alone for a long enough period of time, it is assumed that it will eventually reach equilibrium. Even though the system is in equilibrium, its elements remain dynamic. We understand equilibrium as the state of a system in which all of its macro-level variables are independent of time or more general we can say the probability to find the system in a certain microstate doesn't change with respect to time. Statistical physics and thermodynamics are concerned with the many-body system's equilibrium features, without discussing the process of equilibration, which is dealt with in kinetic theory. The goal of kinetic theory is to comprehend the process of approaching equilibrium.

The purpose of this chapter is to design a methodology for determining the degree of thermalization by combining momentum-multiplicity correlation observables in kinetic theory. The Boltzmann equation in relaxation time approximation plus Langevin noise is used to investigate the influence of thermalization on these correlations. We propose a novel non-equilibrium transport equation (4.56) for the two-body distribution function that is compatible with the conservation principles that apply to microscopic scattering phenomena. We discover that these conservation constraints restrict the correlation observables' long-range behavior to behave differently depending on their degree of thermalization. We discovered that transverse momentum fluctuations in peripheral lead-lead (Pb-Pb) collisions at the LHC and gold-gold (Au-Au) collisions at the RHIC deviates significantly from equilibrium. We suggest new measurements that we believe will deliver more accurate information.

On the other hand, we demonstrate that the observables $\mathcal{R}_{PT}$, $\mathcal{C}_{PT}$, $\mathcal{D}_{PT}$, and $\langle \delta p_{t1} \delta p_{t2} \rangle_{PT}$, which are all two-particle correlation observables, are mathematically connected by equation (7.46) interms of survival probability. When these observables are observed or calculated at the same time using the same method, (7.49) can be used as a validation tool for theoretical models, depending on the circumstances.

In Section 7.2, we will explore briefly how to design a generic two-particle correlation function ($G_{12}$), Equation (5.18). The four related two-particle correlation observables (7.23), (7.29), (7.39) and (7.45) all originate from this common source.

### 7.1 Signs of partial thermalization

We employ (4.56) to compute the long-range contribution to transverse momentum, $p_t$, fluctuations in Section (7.2.4) to highlight the promise of these approaches as well as the practical challenges involved. We indicated in Reference [118] that these fluctuations may be exploited to investigate thermalization. There is now a sufficient body of evidence [51, 72, 119] to support this claim. It is well acknowledged that hydrodynamic flow occurs in central collisions of large nuclei. Thus, we predict the earliest signs of thermalization to appear in peripheral collisions, with the significance of these signs growing with increasing in centrality as the system lifespan grows.

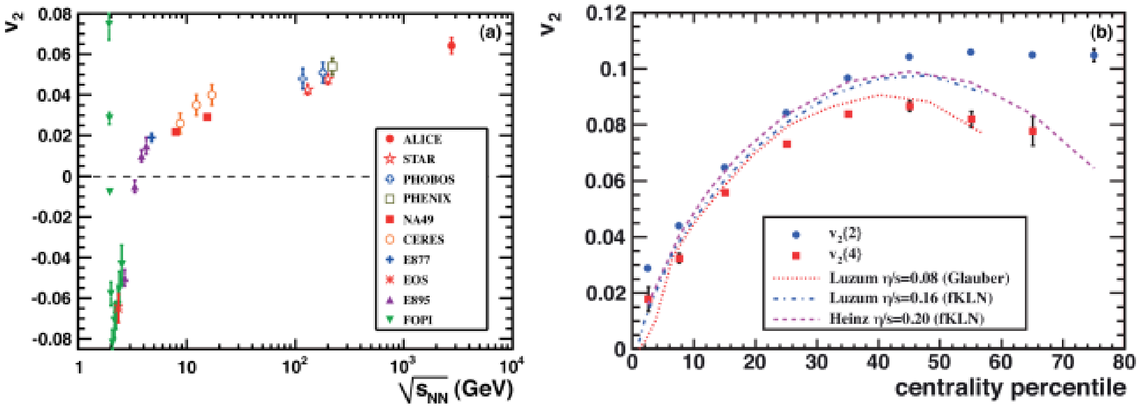

Figure 7.1: Left side figure represent the Integrated elliptic flow $v_2$ at 2.76 $TeV$ compared to lower energies with similar centralities. On the other hand the right side figure represents the elliptic flow vs event centrality for 2-particle and 4-particle cumulant approaches compared to hydrodynamic model calculation[26].

Figure 7.1 illustrates experimental observations of $v_2$. The left figure illustrates elliptic flow throughout a broad range of collisional energies, demonstrating a consistent increase in $v_2$ as energy increases. On the right, the ALICE experiment plots $v_2$ with respect to the centrality (as described in Figure 2.4). Additionally, curves derived from hydrodynamic simulations are displayed. The remarkable correspondence between these curves and data from the central region illustrates hydrodynamics applicability for those collisions. Notably, hydrodynamic models do not agree with evidence from the most peripheral region.

In search of discrepancies with hydrodynamic behavior, Gavin and Moschelli studied the quantity $\langle \delta p_{t1} \delta p_{t2} \rangle$ several years ago [14]. To simulate hydrodynamic flow, they used a blast wave model (the same blast wave that we mentioned in Chapter 2) [16] to get the result as shown in Figure 7.2. They found that, the blast wave model in central collisions fits quite well over a wide range of energy. Importantly, this model systematically fails to account for the peripheral points in the collisions at all energies. This may indicate that the peripheral events are not producing fully equilibrated flow. We will now investigate this hypothesis.

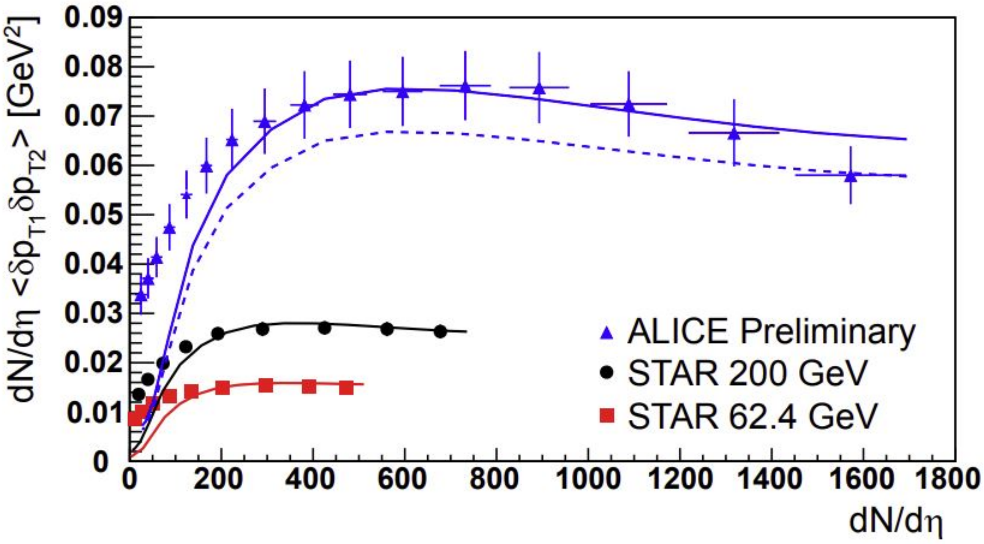

Figure 7.2: Transverse momentum variations versus the number of participants for the three beam energies [14].

One of the thesis objectives is to provide an explanation for this phenomenon. When a system is in local equilibrium, hydrodynamics is relevant. According to data, central collision systems have sufficient time for particle dispersion to thermalize the system. Collisions near the periphery result in systems that are less dense and have shorter lifetimes, and they may be unable to achieve a state of complete equilibrium. Our research is motivated by evidence of insufficient thermalization of data.

Peripheral nuclear collisions are more analogous to proton-proton collisions, since they include far fewer particles and provide significantly less opportunity for equilibration. During the course of its existence, a peripheral collision is unlikely to equilibrate. We will represent nuclear collisions in this chapter, as somewhat of a superposition between the equilibrium expansion (from the blast wave model) and the non-interacting development of an initial state (from ISM), and the connection between the initial and equilibrium state for most observables depends on the survival probability, $S$.

### 7.2 Observables interms of survival probability

The differential phase space elements in this chapter are denoted by the abbreviation $d\omega = d\mathbf{x}d\mathbf{p}$. The event averages must be distinguished from the average across thermal fluctuations in chapter 4. We'll refer to the thermal noise average as $\langle Y\rangle_n$ from now on.

The average of a noise-averaged quantity $\langle\langle Y\rangle_n\rangle$ over events is equal to the average of $\langle Y\rangle_n$ over initial circumstances.

The fluctuation observables $\mathcal{R}_{PT}$, $\mathcal{C}_{PT}$, $\mathcal{D}_{PT}$, and $\langle\delta p_{t1}\delta p_{t2}\rangle_{PT}$ are expressed in this section as integrals of the pair correlation function $G_{12}$. To write fluctuation observables as integrals, we shall establish the following relevant relations

$$\sum_{i,j} u_i v_j = \sum_{i\neq j} u_i v_j + \sum_i u_i v_i \tag{7.1}$$

$$\sum_{i,j} u_i v_j = \int\int u_1 v_2 \left\langle f_1 f_2\right\rangle_n d\omega_1 d\omega_2 \tag{7.2}$$

$$\sum_i u_i v_i = \int\int u_1 v_2 \left\langle f_1\right\rangle_n \delta(1-2) d\omega_1 d\omega_2 \tag{7.3}$$

$$\bar{U} = \int\int u \left\langle f\right\rangle_n d\omega \tag{7.4}$$

$$\bar{V} = \int\int v \left\langle f\right\rangle_n d\omega \tag{7.5}$$

where $u$ and $v$ are either 1, $p_t$ or $\delta p_t$ and $\langle f\rangle_n$ is the noise average of the distribution function.

Take note of the fact that each of observabels quantities has the same form:

$$\left\langle N\right\rangle^2 F_{uv} = \left\langle \sum_{i\neq j} u_i v_j \right\rangle - \left\langle \sum_i u_i \right\rangle \left\langle \sum_i v_i \right\rangle \tag{7.6}$$

all averages in (7.6) are averages over events. We must now know the distinction between this event average and the average over thermal noise that was employed primarily in the preceding equations.

Add and subtract $\bar{U}\bar{V}$ to (7.2)

$$\sum_{i,j} u_i v_j = \int\int u_1 v_2 \left[\left\langle f_1 f_2\right\rangle_n - \left\langle f_1\right\rangle_n \left\langle f_2\right\rangle_n + \left\langle f_1\right\rangle_n \left\langle f_2\right\rangle_n\right] d\omega_1 d\omega_2. \tag{7.7}$$

From (7.7) we can see the first two terms on the right-side is equivalent to $\int\int u_1 v_2 C_{12} d\omega_1 d\omega_2$, where $C_{12}$ is the noise-averaged correlation function (4.19). Averaging (7.7) quantity over events yields

$$\left\langle \sum_{i,j} u_i v_j \right\rangle = \langle \bar{U}\bar{V} \rangle + \int\int u_1 v_2 \langle C_{12} \rangle d\omega_1 d\omega_2. \tag{7.8}$$

substitute (7.1) in (7.6), we will find

$$\langle N \rangle^2 F_{uv} = \left\langle \sum_{i,j} u_i v_j \right\rangle - \left\langle \sum_{i} u_i v_i \right\rangle - \langle \bar{U} \rangle \langle \bar{V} \rangle \tag{7.9}$$

substitute (4.29) in (7.8), we'll find out

$$\left\langle \sum_{i,j} u_i v_j \right\rangle = \int\int u_1 v_2 \langle G_{12} \rangle d\omega_1 d\omega_2 + \int\int u_1 v_2 \langle f \rangle_n d\omega_1 d\omega_2 + \langle \bar{U}\bar{V} \rangle \tag{7.10}$$

subrogate (7.10) in (7.9)

$$\begin{aligned} \langle N \rangle^2 F_{uv} = \int\int u_1 v_2 \langle G_{12} \rangle d\omega_1 d\omega_2 + \int\int u_1 v_2 \langle f \rangle_n d\omega_1 d\omega_2 + \langle \bar{U}\bar{V} \rangle \\ - \left\langle \sum_{i} u_i v_i \right\rangle - \langle \bar{U} \rangle \langle \bar{V} \rangle \end{aligned}$$

From the above, we can notice that the second and fourth terms on the right side of the equation, they both cancel each other out. So,

$$\langle N \rangle^2 F_{uv} = \int\int u_1 v_2 \langle G_{12} \rangle d\omega_1 d\omega_2 + \langle \bar{U}\bar{V} \rangle - \langle \bar{U} \rangle \langle \bar{V} \rangle . \tag{7.11}$$

By employing the equilibrium distribution $G^e_{12}$, we derive a generic equation for $F_{uv}$. The projection operators in $G^e_{12} = P_1 P_2 G_{12}$ suggest that $G^e_{12} = -f^e_1 \delta(1-2)$, which has a straightforward interpretation. The one-body distribution $f$ implies a stochastic path towards the local equilibrium distribution $f^e$ for a given initial state. All such pathways go to the same $f^e$, with no correlations. Following that, the event-averaged correlation function is expressed as $\langle G^e_{12} \rangle = -\langle f^e_1 \rangle \delta(1-2)$. Add and subtract $\int\int u_1 v_2 G^e_{12} d\omega_1 d\omega_2$ to (7.11), We discover

$$\langle N \rangle^2 F_{uv} = \langle N \rangle^2 F^e_{uv} + \int\int u_1 v_2 \langle G_{12} - G^e_{12} \rangle d\omega_1 d\omega_2 \tag{7.12}$$

where

$$\langle N \rangle^2 F^e_{uv} = \langle \bar{U}\bar{V} \rangle - \langle \bar{U} \rangle \langle \bar{V} \rangle + \int\int u_1 v_2 G^e_{12} d\omega_1 d\omega_2 \tag{7.13}$$

the last term in (7.13) is equivalent to $\langle N\rangle \langle uv\rangle^e$, where $\langle N\rangle \langle uv\rangle^e$ is averaged over the equilibrium $f^e$.

In particular, we want to underline that the $\left\langle \bar{U}\bar{V}\right\rangle - \left\langle \bar{U}\right\rangle \left\langle \bar{V}\right\rangle$ contribution to $F^e_{uv}$ only takes into account fluctuations in the total $U$ and $V$ resulting from the initial fluctuations in each event. The final term denotes the fluctuations in the equilibrium state. We shall find that observed correlations deviate from these contributions when the influence of non-equilibrium correlations (7.12) is negligible or is prohibited by conservation laws.

### 7.2.1 Multiplicity-fluctuations

In order to find the multiplicity-fluctuation, $\mathcal{R}_{PT}$, under partial thermalization conditions we will use $u = v = 1$ and $F_{uv} \equiv \mathcal{R}_{PT}$ in (7.12) to find

$$\langle N\rangle^2 \mathcal{R}_{PT} = \langle N\rangle^2 \mathcal{R}^e + \int\int \langle G_{12} - G^e_{12}\rangle \, d\omega_1 d\omega_2 \tag{7.14}$$

where,

$$\langle N\rangle^2 \mathcal{R}^e = \left\langle \bar{N}(\bar{N}-1)\right\rangle - \left\langle \bar{N}\right\rangle^2 \tag{7.15}$$

$$\bar{N} = \sum_{i=1}^{N_k} 1 = \int\int \langle f\rangle_n \, d\omega \tag{7.16}$$

$$\bar{N}(\bar{N}-1) = \sum_{i=1}^{N_k}\sum_{i\neq j}^{N_k} 1 = \int\int \left[\langle f_1 f_2\rangle_n - \langle f_1\rangle_n \delta(1-2)\right] d\omega_1 d\omega_2 \tag{7.17}$$

The evolution of each event effectively conserves particle number $N$, so that $\bar{N} = N$. If we compare the second right term in (7.14) to (4.45) and (4.56), we will find

$$\int\int \langle G_{12} - G^e_{12}\rangle \, d\omega_1 d\omega_2 = \int\int \langle X_{12} + X_{21} + \Delta G_{12}\rangle \, d\omega_1 d\omega_2 \tag{7.18}$$

so,

$$\int\int \langle G_{12} - G^e_{12}\rangle \, d\omega_1 d\omega_2 = S\int\int \left(X^0_{12} + X^0_{21}\right) d\omega_1 d\omega_2 + S^2\int\int \Delta G^0_{12} d\omega_1 d\omega_2 \tag{7.19}$$

where

$$X^0_{21} = \langle \delta f_1 f^e_2\rangle_n - \langle \delta f_1\rangle_n \langle f^e_2\rangle_n \tag{7.20}$$

$$X^0_{12} = \langle \delta f_2 f^e_1 \rangle_n - \langle \delta f_2 \rangle_n \langle f^e_1 \rangle_n \tag{7.21}$$

$$\Delta G^0_{12} = \langle \delta f_1 \delta f_2 \rangle_n - \langle \delta f_1 \rangle_n \langle \delta f_2 \rangle_n - \langle \delta f_1 \rangle_n \delta(1-2) \tag{7.22}$$

in which the integrals in (7.19) are valid across the whole momentum range as well as the constant proper time freeze out surface. In $X^0_{12}$, $X^0_{21}$ and $\Delta G^0_{12}$, the projection operators $(1-P)$ enforce number conservation by causing the integrals on the right hand side in (7.19) to vanish. In this way,

$$\mathcal{R}_{PT} = \mathcal{R}^e \tag{7.23}$$

where $\mathcal{R}^e$ is multiplicity fluctuations at local-equilibrium. We pick in this thesis that, $\mathcal{R}^e = \frac{const}{dN/dy}$ and adjust the proportionality constants to make the computation of the blast wave consistent. The reason for this is to make sure that the events described by $\langle \delta p_{t1} \delta p_{t2} \rangle_{eq}$ and $\langle \delta p_{t1} \delta p_{t2} \rangle_0$ have the same number of particles in them.

### 7.2.2 Multiplicity-momentum correlations

In order to derive multiplicity-momentum correlations, $\mathcal{D}_{PT}$, we use the values $u = \delta p_t = p_t - \langle p_t \rangle$ and $v = 1$. The result of Equation (7.12) is

$$\mathcal{D}_{PT} = \mathcal{D}^{eq} + \frac{\int\int \delta p_{t1} \langle G_{12} - G^e_{12} \rangle d\omega_1 d\omega_2}{\langle N \rangle^2} \tag{7.24}$$

where $\mathcal{D}^{eq}$ is the multiplicity-momentum correlations at equilibrium, as determined by the blast wave model. The second right-term in (7.24) compared to (4.45) and (4.56) can be written as

$$\begin{aligned}\frac{\int\int \delta p_{t1} \langle G_{12} - G^e_{12} \rangle d\omega_1 d\omega_2}{\langle N \rangle^2} = & \frac{\int\int (p_{t1} X_{12} + p_{t1} X_{21} + p_{t1} \Delta G_{12}) d\omega_1 d\omega_2}{\langle N \rangle^2} \\ & - \langle p_t \rangle \frac{\int\int (X_{12} + X_{21} + \Delta G_{12}) d\omega_1 d\omega_2}{\langle N \rangle^2}\end{aligned}$$

the second right-term will vanish compared to (7.18) and (7.19), since in $X^0_{12}$, $X^0_{21}$ and $\Delta G^0_{12}$, the projection operators $(1-P)$ enforce number conservation by causing the integral to vanish. While for the first right-term the projection operator $(1-P)$ in $X^0_{12}$ and $\Delta G^0_{12}$ enforce number conservation, forcing the integrals to vanish since,

$$\int\int p_{t1} X_{12} d\omega_1 d\omega_2 \approx \langle p_t \rangle S \int\int X^0_{12} d\omega_1 d\omega_2 = 0 \tag{7.25}$$

$$\int\int p_{t1}\Delta G_{12}d\omega_1 d\omega_2 = S^2\int\int p_{t1}\Delta G^0_{12}d\omega_1 d\omega_2 = 0 \tag{7.26}$$

$$\int\int p_{t1}X_{21}d\omega_1 d\omega_2 = S\int\int p_{t1}X^0_{21}d\omega_1 d\omega_2 = \langle N\rangle^2 AS \tag{7.27}$$

where the presence of the non-conserved quantity $p_t$ in (7.27) prevents the projection $1 - P_1$ from annihilating this integral. Where $A$ in (7.27) is $\int\int p_{t1}X^0_{12}d\omega_1 d\omega_2/\langle N\rangle^2$. Both numerator and denominator in $A$ depends on $\tau$ through the range of paths in the integrand. We can write (7.24) as

$$\mathcal{D}_{PT} = \mathcal{D}^{eq} + AS. \tag{7.28}$$

We assume that $A$ is approximately constant when we integrate over the full rapidity. We are currently utilizing the fact that when

$$\tau \to \tau_0 \qquad S(0) \approx 1 \qquad \& \qquad \tau \to \infty \qquad S(\infty) \to 0.$$

We can notice that, from the above conditions of survival probability $A$ equal to $\mathcal{D}^0 - \mathcal{D}^{eq}$. The final relation of (7.28) can be written as

$$\mathcal{D}_{PT} = \mathcal{D}^0 S + \mathcal{D}^{eq}(1 - S) \tag{7.29}$$

where $\mathcal{D}^0$ is the initial multiplicity-momentum fluctuations, which is obtained from ISM, $\mathcal{D}^{eq}$ is the multiplicity-momentum fluctuations at local equilibrium and $S$ is the survival probability. The fact that the terms in (7.29) contain just one power of $S$ is directly related to the fact that they are integrated over the momentum space of only a single particles. In principle, elastic scattering influences the momentum of particles but not their number, and when we examine only one momentum, we obtain only a single power of $S$, the survival probability.

### 7.2.3 Transverse momentum correlations

Taking $u = v = p_t$ gives the transverse momentum correlations, $\mathcal{C}_{PT}$, as follows from (5.47). We have obtained

$$\mathcal{C}_{PT} = \mathcal{C}^{eq} + \frac{\int\int p_{t1}p_{t2}\left\langle G_{12} - G_{12}^{e}\right\rangle d\omega_1 d\omega_2}{\left\langle N\right\rangle^2} \tag{7.30}$$

where

$$\mathcal{C}^{eq} = \left\langle \bar{P}_t^2\right\rangle - \left\langle \bar{P}_t\right\rangle^2 - \left\langle N\right\rangle \left\langle p_t^2\right\rangle^e \tag{7.31}$$

is the transverse momentum correlations at equilibrium, as determined by the blast wave model. The second right-term in (7.30) compared to (4.45) and (4.56) can be written as

$$\frac{\int\int p_{t1}p_{t2}\left\langle G_{12} - G_{12}^{e}\right\rangle d\omega_1 d\omega_2}{\left\langle N\right\rangle^2} = \frac{\int\int p_{t1}p_{t2}\left(X_{12} + X_{21} + \Delta G_{12}\right) d\omega_1 d\omega_2}{\left\langle N\right\rangle^2} \tag{7.32}$$

The first right-part of (7.32), can be determined as

$$\frac{\int\int p_{t1}p_{t2}X_{12} d\omega_1 d\omega_2}{\left\langle N\right\rangle^2} = S\frac{\int\int p_{t1}p_{t2}X_{12}^0 d\omega_1 d\omega_2}{\left\langle N\right\rangle^2} \approx S\left\langle p_t\right\rangle \frac{\int\int p_{t2}X_{12}^0 d\omega_1 d\omega_2}{\left\langle N\right\rangle^2}. \tag{7.33}$$

Compare (7.33) to (7.27) with the value of $A$ from $\mathcal{D}_{PT}$, we will obtain

$$\frac{\int\int p_{t1}p_{t2}X_{12} d\omega_1 d\omega_2}{\left\langle N\right\rangle^2} = \left\langle p_t\right\rangle (\mathcal{D}^0 - \mathcal{D}^{eq})S. \tag{7.34}$$

Now, if we do same steps for the second right-part of (7.32) compared to the first part. We will obtain the following

$$\frac{\int\int p_{t1}p_{t2}X_{21} d\omega_1 d\omega_2}{\left\langle N\right\rangle^2} = \left\langle p_t\right\rangle (\mathcal{D}^0 - \mathcal{D}^{eq})S. \tag{7.35}$$

For the last right-part of (7.32), we will obtain

$$\frac{\int\int p_{t1}p_{t2}\Delta G_{21} d\omega_1 d\omega_2}{\left\langle N\right\rangle^2} = S^2\frac{\int\int p_{t1}p_{t2}\Delta G_{21}^0 d\omega_1 d\omega_2}{\left\langle N\right\rangle^2} \approx BS^2 \tag{7.36}$$

where $B = \int\int p_{t1}p_{t2}\Delta G_{21}^0 d\omega_1 d\omega_2 / \left\langle N\right\rangle^2$. The presence of the non-conserved quantity $p_{t1,2}$ in (7.36) prevents the projection $(1 - P_1)(1 - P_2)$ from annihilating this integral. Both numerator and denominator in $B$ depends on $\tau^2$ through the range of paths in the integrand. We assume that $B$ is approximately constant when we integrate over the full rapidity.

Substitute (7.34), (7.35) and (7.36) in (7.30). We will have

$$\mathcal{C}_{PT} = \mathcal{C}^{eq} + 2\left\langle p_t \right\rangle (\mathcal{D}^0 - \mathcal{D}^{eq})S + BS^2. \tag{7.37}$$

In order to determine $B$, we will use the preceding conditions of $S$. So

$$B = \mathcal{C}^0 - \mathcal{C}^{eq} - 2\left\langle p_t \right\rangle (\mathcal{D}^0 - \mathcal{D}^{eq}) \tag{7.38}$$

substitute (7.38) in (7.37), in order to obtain the following relation

$$\mathcal{C}_{PT} = \mathcal{C}^0 S^2 + 2\left\langle p_t \right\rangle (\mathcal{D}^0 - \mathcal{D}^{eq})S(1-S) + \mathcal{C}^{eq}(1-S^2) \tag{7.39}$$

where $\mathcal{C}^0$ is the initial momentum-momentum fluctuations, $\mathcal{C}^e$ is the momentum-momentum fluctuations at local equilibrium and $\langle p_t \rangle$ represented the average transverse momentum at local equilibrium. To facilitate understanding, we split in (7.39) the initial and equilibrium variables. Finally, we discover that $\mathcal{C}_{PT}$ relationship to $S$ is more complicated than the other observables. The symbiotic relationship between $\mathcal{C}$ and $\mathcal{D}$ is especially interesting. As $S$ declines from 1 to 0, this middle term's proportional contribution increases from 0 to 1. $\mathcal{C}^{eq}$, on the other hand, develops at a far quicker rate compared to the middle term.

### 7.2.4 Correlations of transverse momentum fluctuations

To calculate the influence of thermalization on transverse momentum fluctuations we will assume $u = v = \delta p_t$, then the following equation will be used

$$\left\langle \delta p_{t1} \delta p_{t2} \right\rangle_{PT} = \left\langle \delta p_{t1} \delta p_{t2} \right\rangle_{eq} + \frac{\int\int \delta p_{t1} \delta p_{t2} \left\langle G_{12} - G^e_{12} \right\rangle d\omega_1 d\omega_2}{\left\langle N(N-1) \right\rangle} \tag{7.40}$$

where, for a system in local equilibrium, the amount $\left\langle \delta p_{t1} \delta p_{t2} \right\rangle_{eq}$ contains both initial and thermal state fluctuations. In order to determine the right most term of (7.40), we will expand the $p_t$ fluctuations as,

$$\delta p_{t1} \delta p_{t2} = p_{t1} p_{t2} - \left\langle p_t \right\rangle p_{t1} - \left\langle p_t \right\rangle p_{t2} + \left\langle p_t \right\rangle^2 \tag{7.41}$$

The second right-term in (7.40) compared to (4.45) and (4.56) can be written as

$$\frac{\int\int \delta p_{t1} \delta p_{t2} \left\langle G_{12} - G^e_{12} \right\rangle d\omega_1 d\omega_2}{\left\langle N(N-1) \right\rangle} = \frac{\int\int \delta p_{t1} \delta p_{t2} \left( X_{12} + X_{21} + \Delta G_{12} \right) d\omega_1 d\omega_2}{\left\langle N(N-1) \right\rangle} \tag{7.42}$$

Now combine (7.41) to (7.42). The first right term from (7.42) can be written as

$$\begin{aligned}
\frac{\int\int \delta p_{t1}\delta p_{t2}X_{12}}{\langle N(N-1)\rangle} &\approx S\frac{\int\int \left(p_{t1}p_{t2} - \langle p_t\rangle p_{t1} - \langle p_t\rangle p_{t2} + \langle p_t\rangle^2\right) X_{12}^0 d\omega_1 d\omega_2}{\langle N(N-1)\rangle} \\
&\approx S\left(\langle p_t\rangle \frac{\int\int p_{t2}X_{12}^0}{\langle N(N-1)\rangle} - 0 - \langle p_t\rangle \frac{\int\int p_{t2}X_{12}^0}{\langle N(N-1)\rangle} + 0\right) \\
&= 0
\end{aligned}$$

The second right-term of (7.42)

$$\begin{aligned}
\frac{\int\int \delta p_{t1}\delta p_{t2}X_{21}}{\langle N(N-1)\rangle} &\approx S\frac{\int\int \left(p_{t1}p_{t2} - \langle p_t\rangle p_{t1} - \langle p_t\rangle p_{t2} + \langle p_t\rangle^2\right) X_{21}^0 d\omega_1 d\omega_2}{\langle N(N-1)\rangle} \\
&\approx S\left(\langle p_t\rangle \frac{\int\int p_{t1}X_{21}^0}{\langle N(N-1)\rangle} - \langle p_t\rangle \frac{\int\int p_{t1}X_{21}^0}{\langle N(N-1)\rangle} - 0 + 0\right) \\
&= 0
\end{aligned}$$

The third right-term of (7.42)

$$\begin{aligned}
\frac{\int\int \delta p_{t1}\delta p_{t2}\Delta G_{12}}{\langle N(N-1)\rangle} &\approx S^2\frac{\int\int \left(p_{t1}p_{t2} - \langle p_t\rangle p_{t1} - \langle p_t\rangle p_{t2} + \langle p_t\rangle^2\right) \Delta G_{12}^0 d\omega_1 d\omega_2}{\langle N(N-1)\rangle} \\
&\approx S^2\left(\frac{\int\int p_{t1}p_{t2}\Delta G_{12}^0}{\langle N(N-1)\rangle} - 0 - 0 + 0\right) \\
&= A'S^2
\end{aligned}$$

where $A' = \int\int p_{t1}p_{t2}\Delta G_{21}^0 d\omega_1 d\omega_2 / \langle N(N-1)\rangle$. Both numerator and denominator in $A'$ depends on $\tau^2$ through the range of paths in the integrand. We assume that $A'$ is approximately constant when we integrate over the full rapidity.

Combine the three calculated terms to (7.40), we will obtain

$$\langle \delta p_{t1}\delta p_{t2}\rangle_{PT} = \langle \delta p_{t1}\delta p_{t2}\rangle_{eq} + A'S^2 \tag{7.43}$$

We'll utilize the preceding conditions of $S$ to calculate $A'$. So

$$A' = \langle \delta p_{t1}\delta p_{t2}\rangle_0 - \langle \delta p_{t1}\delta p_{t2}\rangle_{eq} \tag{7.44}$$

substitute (7.44) in (7.43), in order to obtain the following relation

$$\langle \delta p_{t1}\delta p_{t2}\rangle_{PT} = \langle \delta p_{t1}\delta p_{t2}\rangle_0 S^2 + \langle \delta p_{t1}\delta p_{t2}\rangle_{eq}(1-S^2) \tag{7.45}$$

where $S$ again denotes the chance of survival. At the formation time $\tau$, fluctuations begin with an initial value $\langle \delta p_{t1}\delta p_{t2}\rangle_0$ and develop to the equilibrium value $\langle \delta p_{t1}\delta p_{t2}\rangle_{eq}$.

The local equilibrium value $\langle \delta p_{t1}\delta p_{t2}\rangle_{eq}$ has been determined by fluctuations in the initial participant geometry from event to event. These fluctuations are estimated using the blast wave model described in Reference [14]. This model exhibits outstanding agreement with a wide variety of fluctuation, correlation, and flow harmonic observations at both soft and hard scales [59, 120, 121].

### 7.3 Complimentary fluctuation and correlation observables

In accordance with their common origin (7.12) and the concept of a transverse momentum fluctuation $\delta p_t$, the observables $\langle \delta p_{t1}\delta p_{t2}\rangle_{PT}$, (7.45), $\mathcal{D}_{PT}$, (7.29), $\mathcal{R}_{PT}$, (7.23), and $\mathcal{C}_{PT}$, (7.39) are mathematically connected same as Equation (5.12).

We start with the definition (5.12) and work our way up in order to find the relationship between the observables as a function of survival probability.

$$(1+\mathcal{R}_{PT})\,\langle \delta p_{t1}\delta p_{t2}\rangle_{PT} + 2\,\langle p_t\rangle\,\mathcal{D}_{PT} - \mathcal{C}_{PT} + \langle p_t\rangle^2\,\mathcal{R}_{PT} = 0. \tag{7.46}$$

Substitute (7.29), (7.23) and (7.39) in (7.46). we will obtain

$$(1+\mathcal{R}^{eq})\,\langle \delta p_{t1}\delta p_{t2}\rangle_{PT} - \mathcal{C}^{eq} + 2\,\langle p_t\rangle\,(\mathcal{D}^0 - \mathcal{D}^{eq})S^2 + 2\,\langle p_t\rangle\,\mathcal{D}^{eq} - (\mathcal{C}^0 - \mathcal{C}^{eq})S^2 + \langle p_t\rangle^2\,\mathcal{R}^{eq} = 0. \tag{7.47}$$

rearrange (7.47) to obtain

$$(1+\mathcal{R}^{eq})\,\langle \delta p_{t1}\delta p_{t2}\rangle_{PT} - \mathcal{C}^{eq} + 2\,\langle p_t\rangle\,\mathcal{D}^{eq} + \langle p_t\rangle^2\,\mathcal{R}^{eq} - \left[\mathcal{C}^0 - \mathcal{C}^{eq} - 2\,\langle p_t\rangle\,(\mathcal{D}^0 - \mathcal{D}^{eq})\right] S^2 = 0. \tag{7.48}$$

substitute (7.45) in (7.48), then add and subtract $\langle p_t\rangle^2\,\mathcal{R}^{eq}S^2$ from (7.48) to obtain

$$\begin{aligned} &\left[(1+\mathcal{R}^{eq})\,\langle \delta p_{t1}\delta p_{t2}\rangle_{eq} + 2\,\langle p_t\rangle\,\mathcal{D}^{eq} - \mathcal{C}^{eq} + \langle p_t\rangle^2\,\mathcal{R}^{eq}\right](1-S^2)+ \\ &\qquad \left[(1+\mathcal{R}^{eq})\,\langle \delta p_{t1}\delta p_{t2}\rangle_0 + 2\,\langle p_t\rangle\,\mathcal{D}^0 - \mathcal{C}^0 + \langle p_t\rangle^2\,\mathcal{R}^{eq}\right] S^2 = 0. \end{aligned} \tag{7.49}$$

As seen in (7.49), the sum rule varies between the initial and equilibrium states. We can see that at $S = 1$, only the initial observables survive, and equation (7.49) becomes identical to the ISM's sum rule. When $S = 0$, however, as shown in (7.49), only the equilibrium observables remain and the equation becomes identical to the sum rule from blast wave. Finally, when $S$ varies between 0 and 1, our model exists and the partial thermalization sum rule is zero in the range of $10^{-15}$.

## 7.4 Results and discussions

The partial thermalized observables $\mathcal{C}_{PT}$, $\mathcal{D}_{PT}$, and $\langle \delta p_{t1} \delta p_{t2} \rangle_{PT}$ are all dependent on the survival probability except $\mathcal{R}_{PT}$, as shown by the fact that there is a relationship between the initial circumstances and the local equilibrium for each of them depending on the survival probability in the calculations above. For the sake of computing the partial thermalized observables, we will concentrate on two important aspects in this chapter.

First, in order to compute the initial production of the partial thermalized obsrevables, it was necessary to assume that each observable did not contain any bulk collectivity or QGP phase; therefore, in this case we used the Independent Source Model (ISM), which assumes that nuclear collision events are composed of a superposition of the independent sources of particles (see Chapter 6 for more information) and ignores any interactions between the emitted particles from different sources. A variable number of sources are associated with each event, and each source has a fluctuating multiplicity with momentum distribution of particles associated with it. In the following equations, the initial states of the four observables compared to (6.26), (6.27), (6.28) and (6.29) are expressed as

$$\langle \delta p_{t1} \delta p_{t2} \rangle_0 = \frac{2 \langle \delta p_{t1} \delta p_{t2} \rangle_{pp}}{\langle N_{par} \rangle} \frac{(1 + \mathcal{R}_{pp})}{(1 + \mathcal{R})} \tag{7.50}$$

$$\mathcal{C}^0 = \frac{2\mathcal{C}_{pp} + \langle p_t \rangle^2}{\langle N_{part} \rangle}. \tag{7.51}$$

$$\mathcal{R}^0 = \frac{2\mathcal{R}_{pp} + 1}{\langle N_{par} \rangle} \tag{7.52}$$

$$\mathcal{D}^0 = \frac{2\mathcal{D}_{pp}}{\langle N_{part} \rangle} \tag{7.53}$$

where $\langle \delta p_{t1} \delta p_{t2} \rangle_{pp}$, $\mathcal{R}_{pp}$, $\mathcal{C}_{pp}$ and $\mathcal{D}_{pp}$ are the integrated values of observables using PYTHIA *pp* collision (see Table 6.1 and Table 7.1) and $\langle N_{part} \rangle$ is calculated from Equation (2.30) using Glauber model and $\langle p_t \rangle$ from blast wave model (from Chapter 2 Section 2.3).

Second, hydrodynamic theory presupposes that the system remains in local equilibrium throughout the lifetime of the expansion. We will use blast wave model in order to find the four observables $\langle \delta p_{t1} \delta p_{t2} \rangle_{eq}$ (7.45), $\mathcal{R}^{eq}$ (7.23), $\mathcal{C}^{eq}$ (7.31) and $\mathcal{D}^{eq}$ (7.28) since this model was essentially a boosted source type of model and it assumed local equilibrium. Back to Chapter 2, our blast wave performs admirably for the seven various energies tested, and it is sufficiently accurate to be used for the calculation for the values of the four observables in case of local equilibrium

We chose to work with $\langle \delta p_{t1} \delta p_{t2} \rangle_{PT}$ in order to compare our results with those obtained by experiment since this data is the most easily available for a variety of collisional energy. According to (7.50) and its dependency on $\mathcal{R}$, we will examine three distinct versions of $\mathcal{R}$ for each energy, and for each version, we will employ a different type of multiplicity fluctuation. To explain why we employed three distinct versions as we discussed before. We expected the number conservation (7.23). By means the in equilibrium and out of equilibrium, event-by-event multiplicity variations are similar. We would like to emphasize that this is not always the case (by comparing the three distinct versions of $\mathcal{R}$, we will get different values of $\sqrt{\langle \delta p_{t1} \delta p_{t2} \rangle} / \langle p_t \rangle$ as shown for different energies in the plots below). For (7.23), we made substantial assumptions about the equation's linearity and several reducing assumptions about the system's nature in these derivations. Nonetheless, we feel that this illustrated example might aid in gaining a better understanding of the thermalization process.

For the first column for each of the Figures 7.4, 7.6, 7.8, 7.10, 7.12, 7.14 and 7.16 $\langle \delta p_{t1} \delta p_{t2} \rangle_0$ (7.50) was calculated using $\mathcal{R} = \mathcal{R}^0$ (7.52), and we utilized the same scaled $\mathcal{R}^0$ for local equilibrium $\langle \delta p_{t1} \delta p_{t2} \rangle_{eq}$. Then via superposition between $\langle \delta p_{t1} \delta p_{t2} \rangle_0$ and $\langle \delta p_{t1} \delta p_{t2} \rangle_{eq}$, we calculate $\langle \delta p_{t1} \delta p_{t2} \rangle_{PT}$. The solid black curve line in these Figures represented the partial thermalization data, the blue dashed line (initial production) represented the PYTHIA integrated production to AA collision data (ISM), the brown dotted line (local equilibrium flow) represented the blast wave data, the circles, squares and triangles represented the data from STAR at energies 11.5, 19.6, 27, 39, 62.4, and 200 $GeV$ for $Au - Au$ collisions, and the flipped triangles represented the data from ALICE for $Pb - Pb$ collisions at 2760 $GeV$. This assumption leads to a poor fitting of the data from the STAR experiment, particularly at low energies (11.5, 27 and 39 $GeV$). The fit becomes slightly better at higher energies (62.4 and 200 $GeV$), where a handful of points in the central region match the model (black curve line). On the case of $Pb-Pb$ collisions from ALICE at 2760 $GeV$, the model only fit the first five points from data collected in the peripheral region. As a result, we conclude that employing multiplicity fluctuations, $\mathcal{R}^0$, from the Independent Source Model is not a good decision, contrary to what we anticipated.

Due to our belief that $\mathcal{R} = \frac{Const}{dN/dy}$ has physical significance (according to Ref [14] ), we have chosen this as our second option of multiplicity fluctuation condition. In Figure 7.3, it appears that $\mathcal{R} = \frac{Const}{dN/dy}$ estimates are in good agreement with the data from PHENIX for $Au-Au$ at 62.4 $GeV$ and 200 $GeV$ for central collisions only. We pick $\mathcal{R} = \frac{Const}{dN/dy}$ and adjust the proportionality constants to make the computation of the blast wave consistent in the second column for Figures 7.4, 7.6, 7.8, 7.10, 7.12, 7.14 and 7.16. This is done to verify that $\langle \delta p_{t1} \delta p_{t2} \rangle_{eq}$ and $\langle \delta p_{t1} \delta p_{t2} \rangle_0$ accurately represent events with almost the same number of particles. The Au-Au collisions at 11.5 $GeV$ from STAR data still do not fit well with the partial thermalized curve ($\langle \delta p_{t1} \delta p_{t2} \rangle_{PT}$) in Figure 7.16. For Figures 7.14, 7.12 and 7.10, Au-Au collisions at 19.6, 27, and 39 $GeV$, the central region matches somewhat better than the first version of $\mathcal{R}$ ($\mathcal{R} = \mathcal{R}^0$). On the other hand, for $Au-Au$ collisions at 62.4 $GeV$ (Figure 7.8) and 200 $GeV$ (Figure 7.6), the STAR data matches perfectly to the center collision but misses the peripheral collision, however when compared to the initial version of $\mathcal{R}$, the gap in the periphery region between the partial thermalized curve and the data has reduced. In the instance of $Pb-Pb$ collisions at 2760 $GeV$ (Figure 7.4), the partial thermalized curve fits the ALICE data very well, with the exception of the most central and two most peripheral spots. We infer that the model may perform quite well for high energy but not for low energies.

Regarding the third column for figures 7.4, 7.6, 7.8, 7.10, 7.12, 7.14 and 7.16. We used $\mathcal{R} = \frac{Const}{(dN/dy)^{1.125}}$ in (7.5); this version has no physical meaning, but the point is to demonstrate that the data for these figures, in case of $Au-Au$ collisions from STAR at 19.6, 27, 39, 62.4 and 200 $GeV$ matches our model perfectly in this scenario. However, the ALICE data for $Pb-Pb$ collisions at 2760 $GeV$ also matches perfectly.

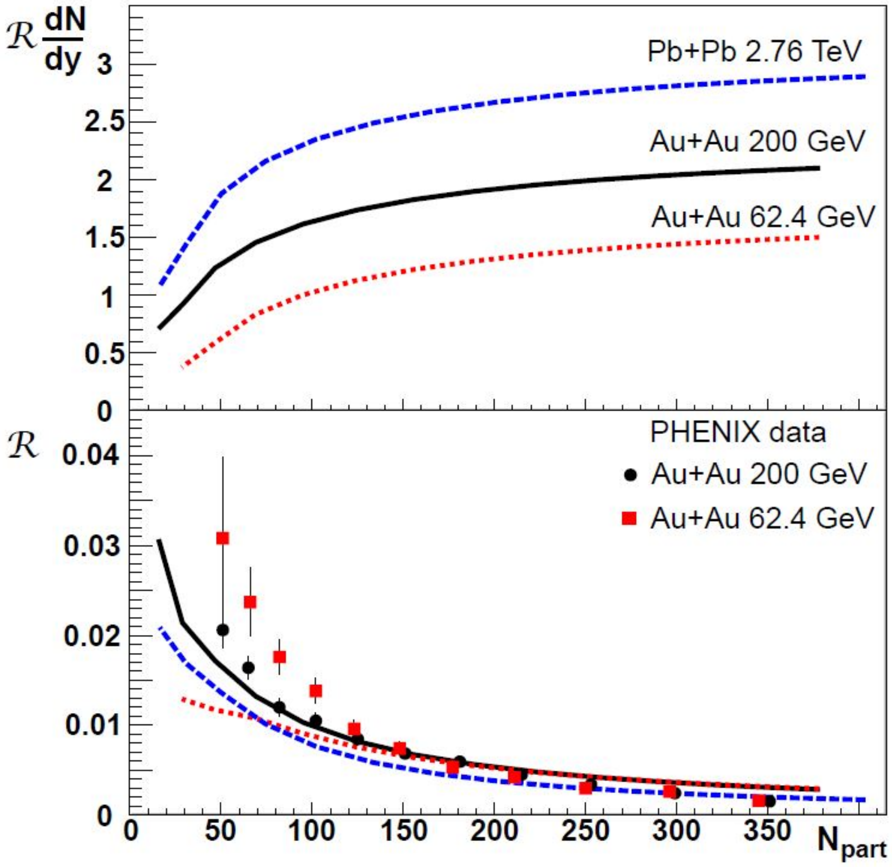

Figure 7.3: $\mathcal{R}dN/dy$ prediction as a function of the number of participants $N_{part}$ for three different beam energies. This plot is taken from Ref [14].

In both $Pb{-}Pb$ collisions at 2760 $GeV$ and $Au{-}Au$ collisions at 11.5, 19.6, 27, 39, 62.4, and 200 $GeV$,the second row of plots from the Figures 7.5, 7.7, 7.9, 7.11, 7.13, 7.15 and 7.17 shows the prediction curves for $\mathcal{C}$ are displayed versus the number of participants for the three distinct versions of $\mathcal{R}$. With the help of the independent source model (ISM) Equation (7.51), the initial production curve can be computed. It is possible to determine the $pp$ reference value in PYTHIA (See Table 6.1 and Table 7.1). The blast wave model is used once more to represent local equilibrium flow (dotted brown line). The partial thermalization curve (solid black line ) is determined with the help of the formula (7.39). $\mathcal{C}$ behaves as predicted in the most peripheral and most central areas, matching the initial and local equilibrium curves, respectively, in the most peripheral and most central regions. The value of the initial production curve does not differ significantly from the value of the equilibrium flow when the present model parameters are used. This means that we do not anticipate $\mathcal{C}$ to provide us with much information on the thermalization of the system while it is operating in the most extreme conditions.

According to Figures 7.5, 7.7, 7.9, 7.11, 7.13, 7.15 and 7.17, the third row graphs shows the prediction of the value of $\mathcal{D}$ in $Pb-Pb$ collisions at 2760 $GeV$ and $Au-Au$ collisions at 11.5, 19.6, 27, 39, 62.4, and 200 $GeV$ versus the number of participants for the three distinct versions of $\mathcal{R}$ (in the first column the three observables, $\mathcal{R}$, $\mathcal{C}$ and $\mathcal{D}$, are calculated when $\mathcal{R} \propto \langle N_{part} \rangle^{-1}$, while in the second column the observables are calculated when $\mathcal{R} \propto (dN/dy)^{-1}$, and for the third column when $\mathcal{R} \propto (dN/dy)^{-1.125}$ ). According to Equation (7.53), an initial production curve was produced using the pp (See Table 6.1 and Table 7.1) reference value computed in PYTHIA as the starting point. In the blast wave model, the value of $\mathcal{D}$ at the local equilibrium was estimated. The blast wave curve for $\mathcal{D}$ has an unusual characteristic in that it is completely in the fourth quadrant. This might be due to a flow that comes from the blast wave model, which would produce a reduction in $\mathcal{D}$ or a lack of jets in this model (blast wave model), which would induce an increase in $\mathcal{D}$ if there were any. We are presently looking into this feature to see whether or not this is the case. When we zoom in on the periphery region for all energies except the 11.5 $GeV$ for the three distinct versions of $\mathcal{R}$ to analyze the partial thermalization curve more closely, we notice a striking shift in the sign of $\mathcal{D}$ that is not apparent in the other observables. The transition from positive to negative values may represent the point at which the flow-like effects of more thermalized center collisions begin to outweigh the jet-like effects found in peripheral proton-proton and nucleus-nucleus collisions.

Importantly, none of the three independent forms of $\mathcal{R}$ break the sum rule for all energies (7.49).

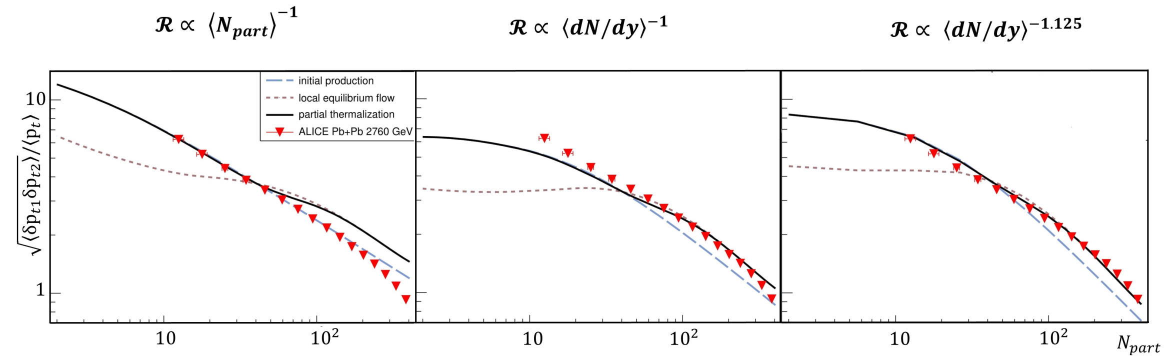

Figure 7.4: Partial thermalized observable (black solid curve) $\langle \delta p_{t1} \delta p_{t2} \rangle_{PT}$ (7.45) were calculated by superposition, using PYTHIA (initial production) and Blast Wave model (local equilibrium flow) for three distinct versions of $\mathcal{R}$ compared to data for $Pb - Pb$ at $\sqrt{s} = 2760\ GeV$. The flipped triangles represent the ALICE data [72].

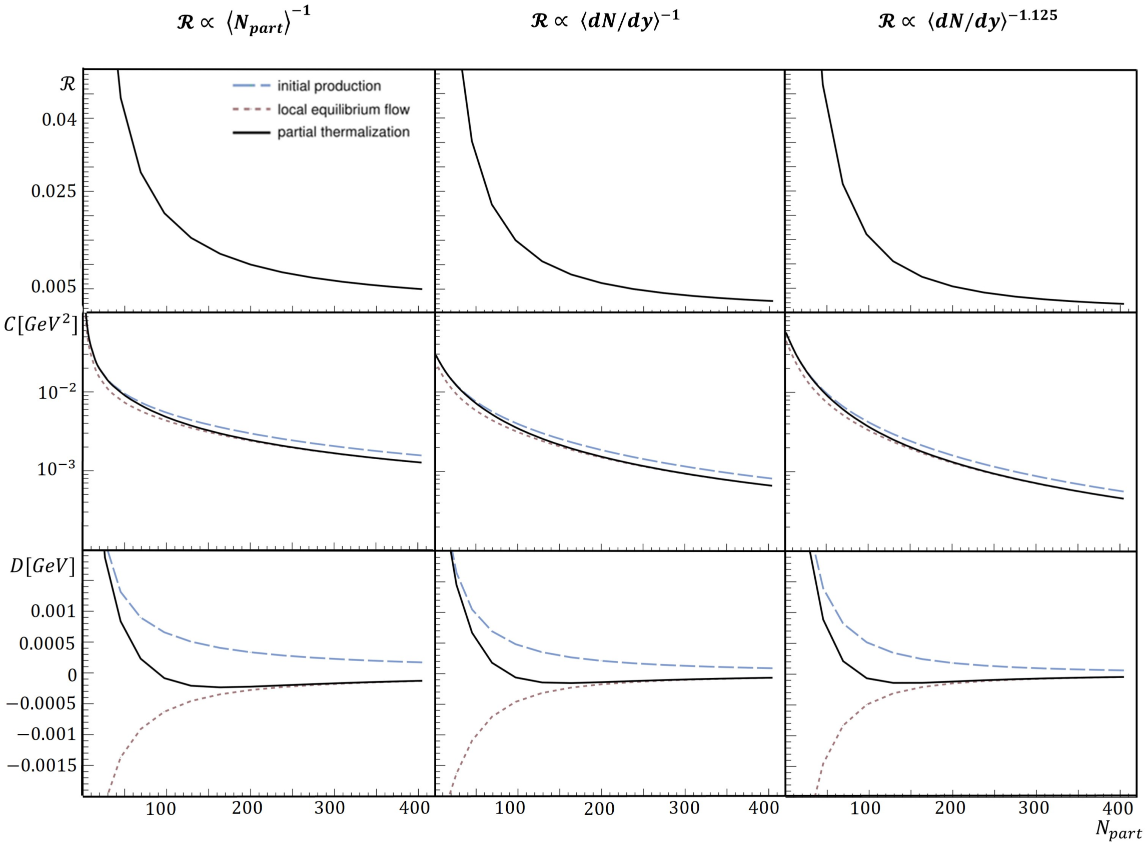

Figure 7.5: Partial thermalized observables (black solid curve) $\mathcal{R}_{PT}$, $\mathcal{C}_{PT}$ and $\mathcal{D}_{PT}$, for $Pb - Pb$ at $\sqrt{s} = 2760\ GeV$ were calculated by superposition, using PYTHIA (initial production) and Blast Wave model (local equilibrium flow) for three distinct versions of $\mathcal{R}$. First column the three observables ( $\mathcal{R}$, $\mathcal{C}$ and $\mathcal{D}$) calculated when $\mathcal{R} \propto \langle N_{part} \rangle^{-1}$, second column when $\mathcal{R} \propto (dN/dy)^{-1}$, and the third column when $\mathcal{R} \propto (dN/dy)^{-1.125}$.

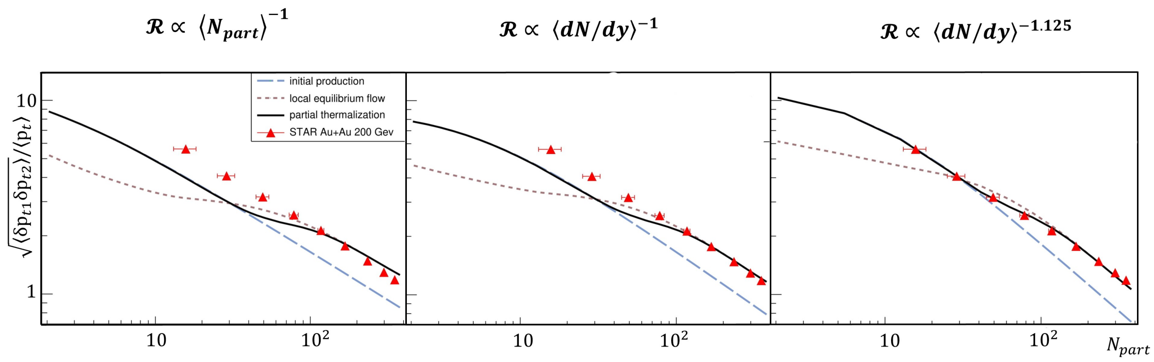

Figure 7.6: Partial thermalized observable (black solid curve) $\langle \delta p_{t1} \delta p_{t2} \rangle_{PT}$ (7.45) were calculated by superposition, using PYTHIA (initial production) and Blast Wave model (local equilibrium flow) for three distinct versions of $\mathcal{R}$ compared to data for $Au - Au$ at $\sqrt{s} = 200\ GeV$. The triangles represent the STAR data [74].

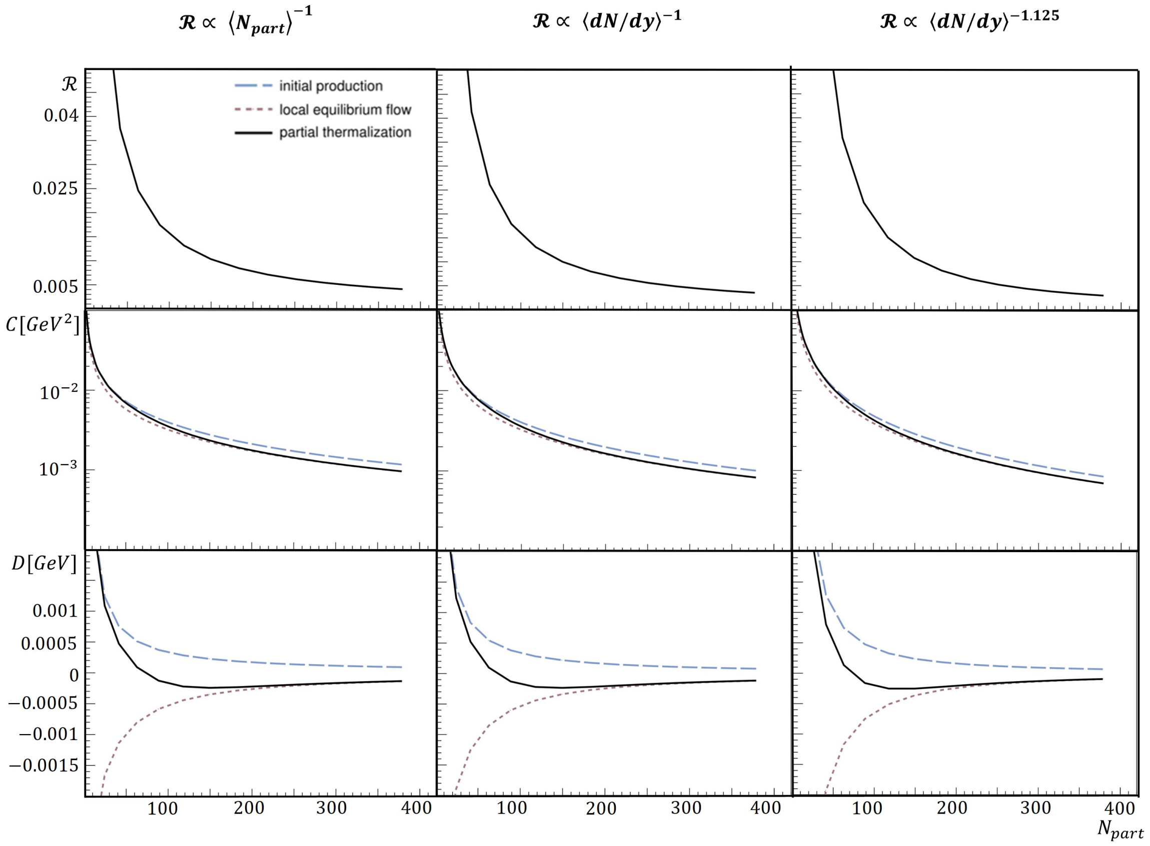

Figure 7.7: Partial thermalized observables (black solid curve) $\mathcal{R}_{PT}$, $\mathcal{C}_{PT}$ and $\mathcal{D}_{PT}$, for $Au - Au$ at $\sqrt{s} = 200\ GeV$ were calculated by superposition, using PYTHIA (initial production) and Blast Wave model (local equilibrium flow) for three distinct versions of $\mathcal{R}$. First column the three observables ( $\mathcal{R}$, $\mathcal{C}$ and $\mathcal{D}$) calculated when $\mathcal{R} \propto \langle N_{part} \rangle^{-1}$, second column when $\mathcal{R} \propto (dN/dy)^{-1}$, and the third column when $\mathcal{R} \propto (dN/dy)^{-1.125}$.

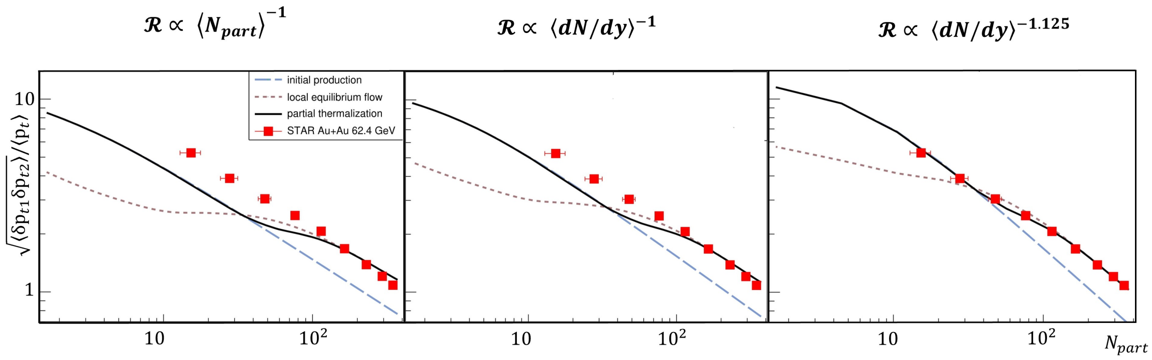

Figure 7.8: Partial thermalized observable (black solid curve) $\langle \delta p_{t1} \delta p_{t2} \rangle_{PT}$ (7.45) were calculated by superposition, using PYTHIA (initial production) and Blast Wave model (local equilibrium flow) for three distinct versions of $\mathcal{R}$ compared to data for $Au - Au$ at $\sqrt{s} = 62.4\ GeV$. The squares represent the STAR data [74].

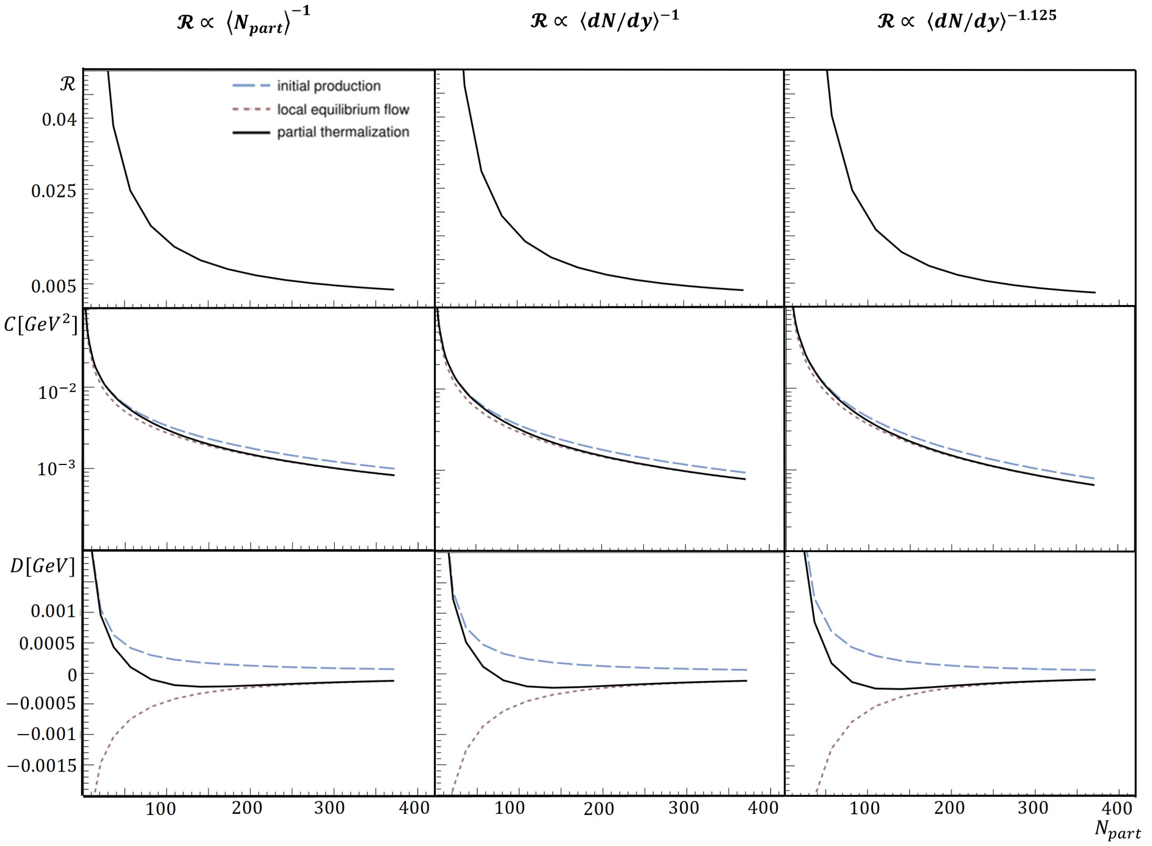

Figure 7.9: Partial thermalized observables (black solid curve) $\mathcal{R}_{PT}$, $\mathcal{C}_{PT}$ and $\mathcal{D}_{PT}$, for $Au - Au$ at $\sqrt{s} = 62.4\ GeV$ were calculated by superposition, using PYTHIA (initial production) and Blast Wave model (local equilibrium flow) for three distinct versions of $\mathcal{R}$. First column the three observables ( $\mathcal{R}$, $\mathcal{C}$ and $\mathcal{D}$) calculated when $\mathcal{R} \propto \langle N_{part} \rangle^{-1}$, second column when $\mathcal{R} \propto (dN/dy)^{-1}$, and the third column when $\mathcal{R} \propto (dN/dy)^{-1.125}$.

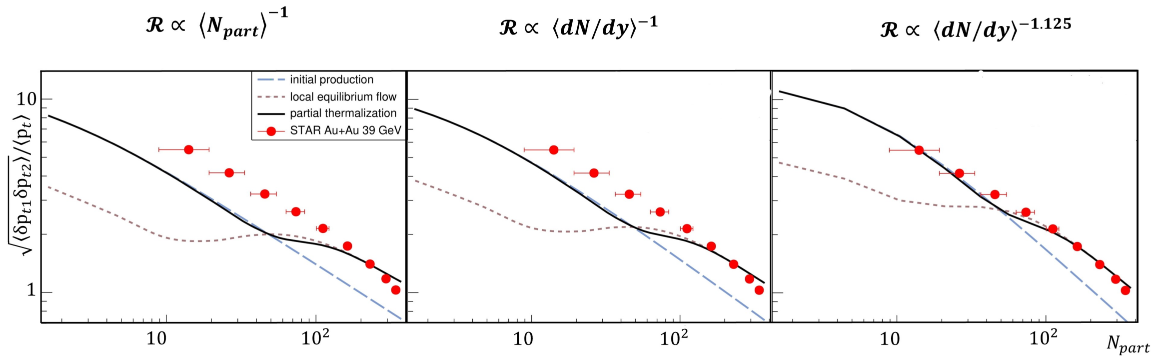

Figure 7.10: Partial thermalized observable (black solid curve) $\langle \delta p_{t1} \delta p_{t2} \rangle_{PT}$ (7.45) were calculated by superposition, using PYTHIA (initial production) and Blast Wave model (local equilibrium flow) for three distinct versions of $\mathcal{R}$ compared to data for $Au - Au$ at $\sqrt{s} = 39\ GeV$. The circles represent the STAR data [74].

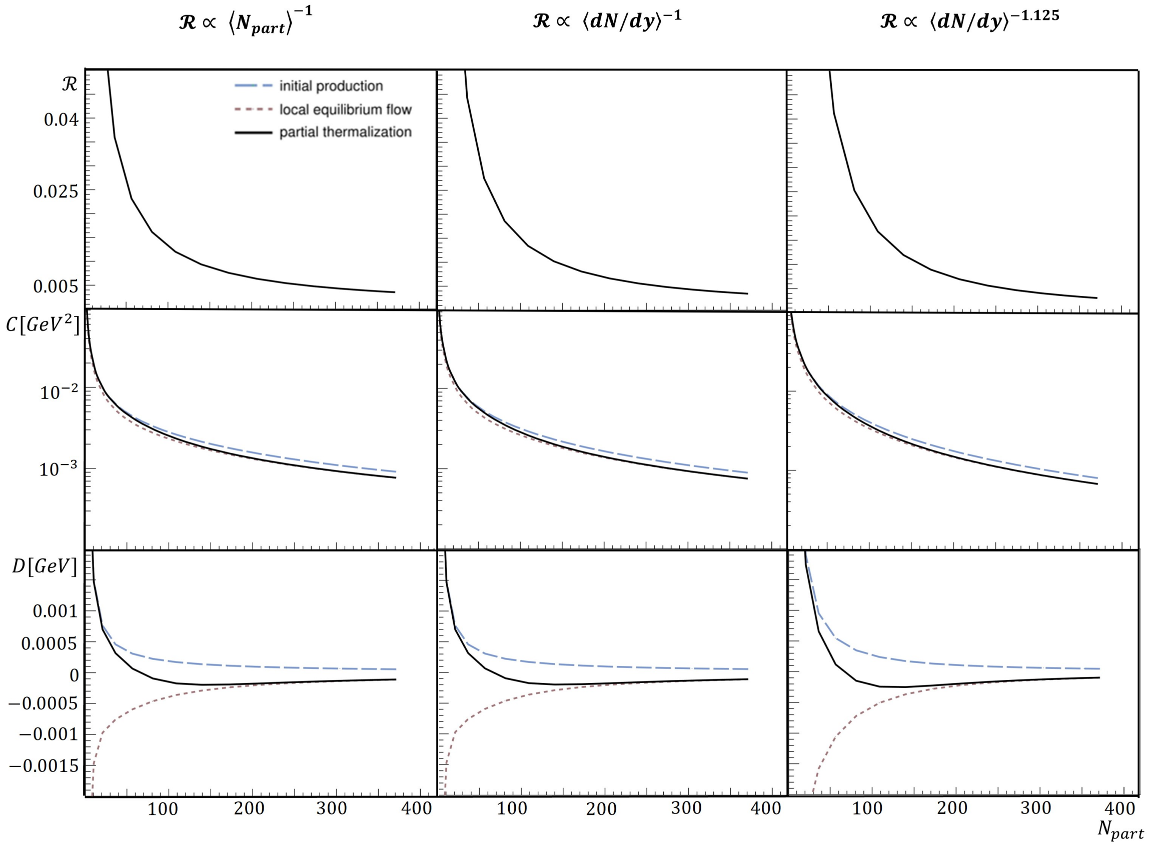

Figure 7.11: Partial thermalized observables (black solid curve) $\mathcal{R}_{PT}$, $\mathcal{C}_{PT}$ and $\mathcal{D}_{PT}$, for $Au - Au$ at $\sqrt{s} = 39\ GeV$ were calculated by superposition, using PYTHIA (initial production) and Blast Wave model (local equilibrium flow) for three distinct versions of $\mathcal{R}$. First column the three observables ( $\mathcal{R}$, $\mathcal{C}$ and $\mathcal{D}$) calculated when $\mathcal{R} \propto \langle N_{part} \rangle^{-1}$, second column when $\mathcal{R} \propto (dN/dy)^{-1}$, and the third column when $\mathcal{R} \propto (dN/dy)^{-1.125}$.

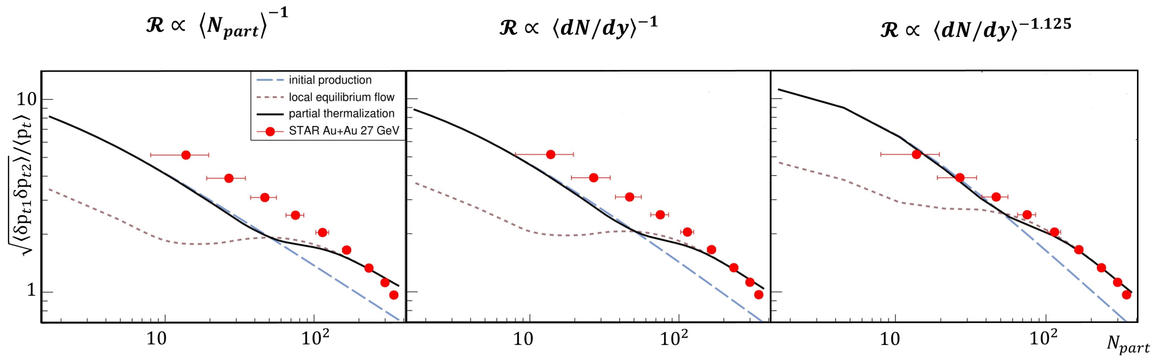

Figure 7.12: Partial thermalized observable (black solid curve) $\langle \delta p_{t1} \delta p_{t2} \rangle_{PT}$ (7.45) were calculated by superposition, using PYTHIA (initial production) and Blast Wave model (local equilibrium flow) for three distinct versions of $\mathcal{R}$ compared to data for $Au-Au$ at $\sqrt{s} = 27\ GeV$. The circles represent the STAR data [74].

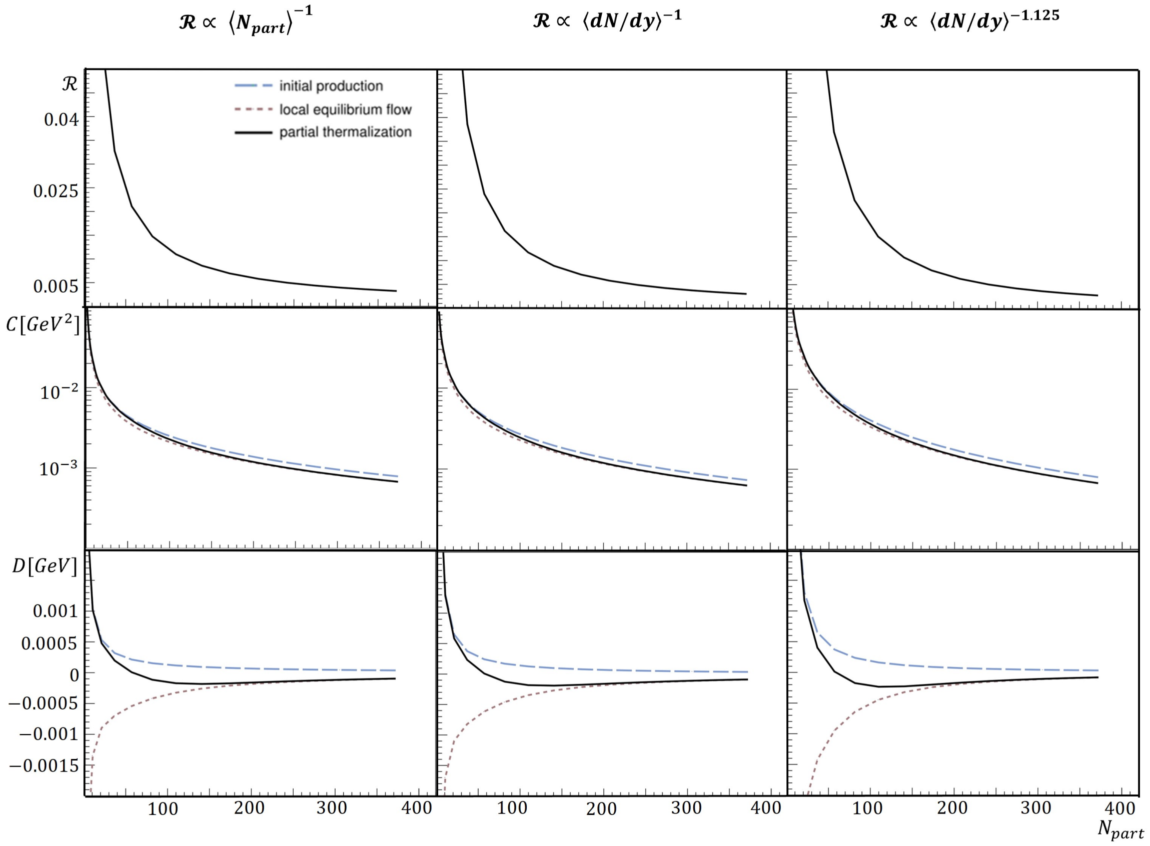

Figure 7.13: Partial thermalized observables (black solid curve) $\mathcal{R}_{PT}$, $\mathcal{C}_{PT}$ and $\mathcal{D}_{PT}$, for $Au-Au$ at $\sqrt{s} = 27\ GeV$ were calculated by superposition, using PYTHIA (initial production) and Blast Wave model (local equilibrium flow) for three distinct versions of $\mathcal{R}$. First column the three observables ( $\mathcal{R}$, $\mathcal{C}$ and $\mathcal{D}$) calculated when $\mathcal{R} \propto \langle N_{part} \rangle^{-1}$, second column when $\mathcal{R} \propto (dN/dy)^{-1}$, and the third column when $\mathcal{R} \propto (dN/dy)^{-1.125}$.

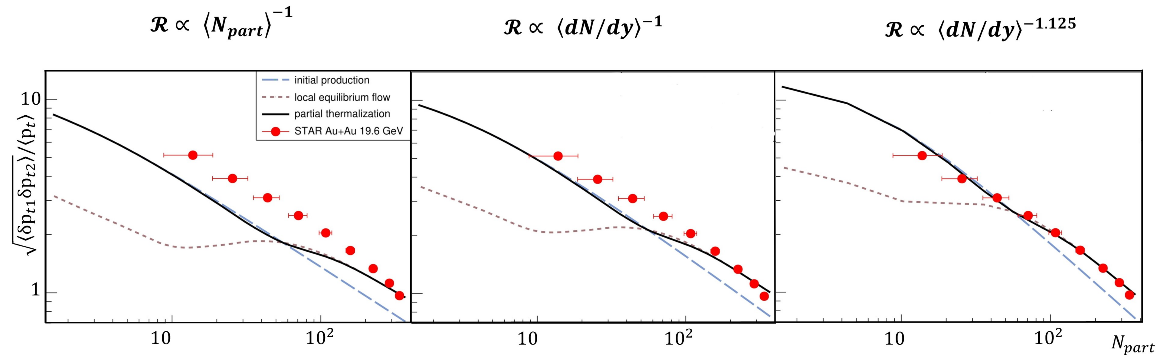

Figure 7.14: Partial thermalized observable (black solid curve) $\langle \delta p_{t1} \delta p_{t2} \rangle_{PT}$ (7.45) were calculated by superposition, using PYTHIA (initial production) and Blast Wave model (local equilibrium flow) for three distinct versions of $\mathcal{R}$ compared to data for $Au-Au$ at $\sqrt{s} = 19.6\ GeV$. The circles represent the STAR data [74].

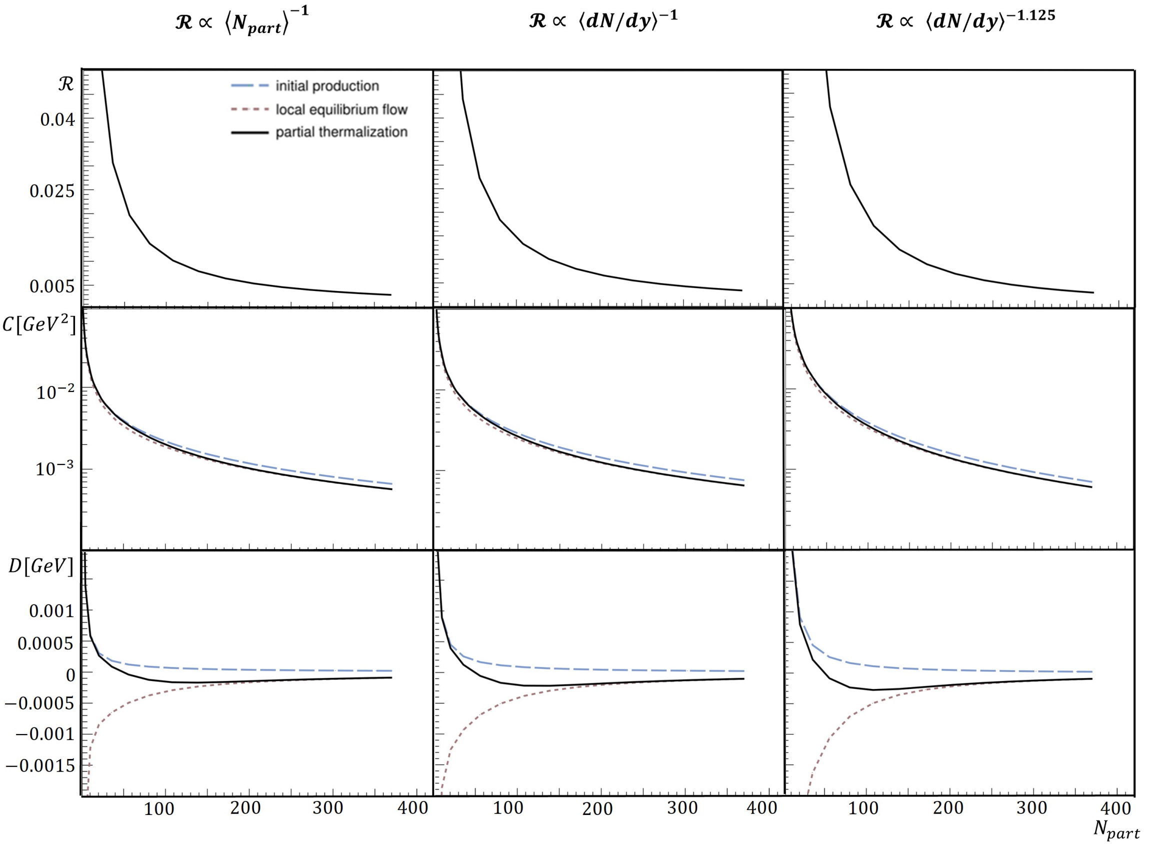

Figure 7.15: Partial thermalized observables (black solid curve) $\mathcal{R}_{PT}$, $\mathcal{C}_{PT}$ and $\mathcal{D}_{PT}$, for $Au-Au$ at $\sqrt{s} = 19.6\ GeV$ were calculated by superposition, using PYTHIA (initial production) and Blast Wave model (local equilibrium flow) for three distinct versions of $\mathcal{R}$. First column the three observables ( $\mathcal{R}$, $\mathcal{C}$ and $\mathcal{D}$) calculated when $\mathcal{R} \propto \langle N_{part} \rangle^{-1}$, second column when $\mathcal{R} \propto (dN/dy)^{-1}$, and the third column when $\mathcal{R} \propto (dN/dy)^{-1.125}$.

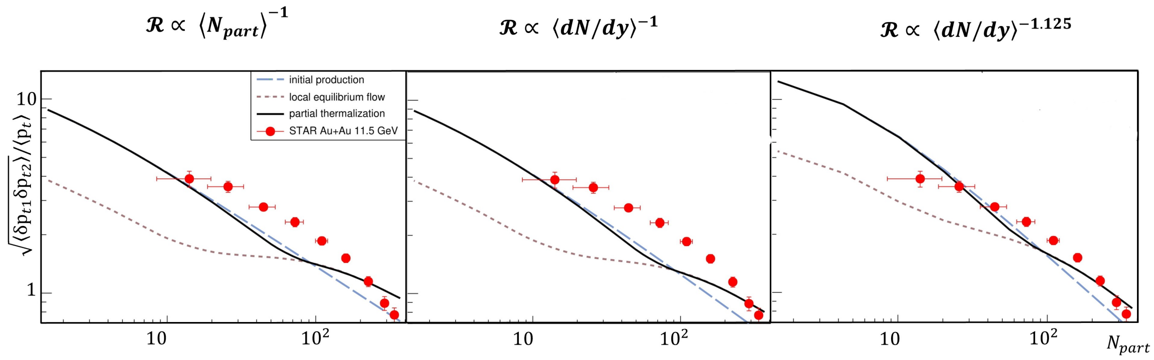

Figure 7.16: Partial thermalized observable (black solid curve) $\langle \delta p_{t1} \delta p_{t2} \rangle_{PT}$ (7.45) were calculated by superposition, using PYTHIA (initial production) and Blast Wave model (local equilibrium flow) for three distinct versions of $\mathcal{R}$ compared to data for $Au - Au$ at $\sqrt{s} = 11.5\ GeV$. The circles represent the STAR data [74].

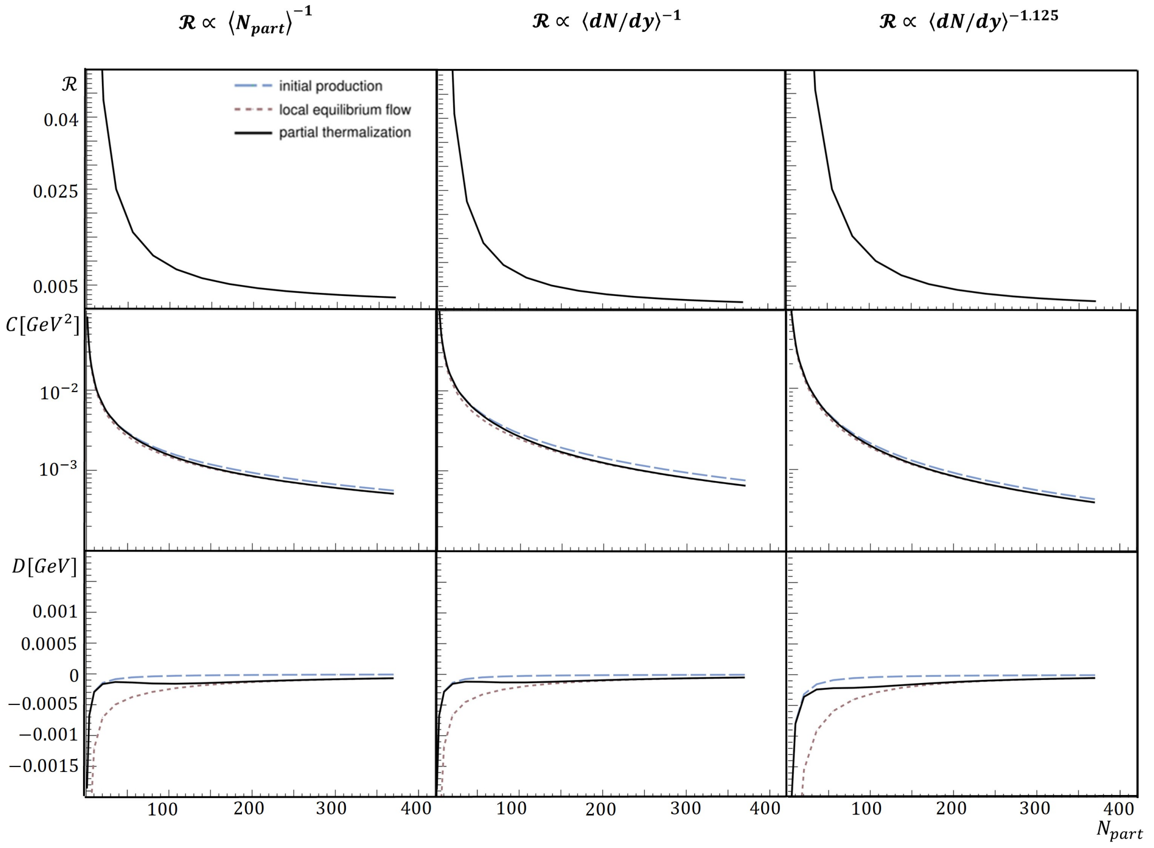

Figure 7.17: Partial thermalized observables (black solid curve) $\mathcal{R}_{PT}$, $\mathcal{C}_{PT}$ and $\mathcal{D}_{PT}$, for $Au - Au$ at $\sqrt{s} = 11.5\ GeV$ were calculated by superposition, using PYTHIA (initial production) and Blast Wave model (local equilibrium flow) for three distinct versions of $\mathcal{R}$. First column the three observables ( $\mathcal{R}$, $\mathcal{C}$ and $\mathcal{D}$) calculated when $\mathcal{R} \propto \langle N_{part} \rangle^{-1}$, second column when $\mathcal{R} \propto (dN/dy)^{-1}$, and the third column when $\mathcal{R} \propto (dN/dy)^{-1.125}$.

| Integrated values of observables using PYTHIA *pp* collision | | | | | |
|---|---|---|---|---|---|
| $\sqrt{s}$ | 11.5 GeV | 19.6 GeV | 27 GeV | 39 GeV | 62.4 GeV |
| $\mathcal{R}_{pp}$ | $-0.0547 \pm 9.97 \times 10^{-4}$ | $0.0492 \pm 1.06 \times 10^{-3}$ | $0.1028 \pm 1.39 \times 10^{-3}$ | $0.1535 \pm 1.48 \times 10^{-3}$ | $0.2027 \pm 1.68 \times 10^{-3}$ |
| $\mathcal{C}_{pp}$ | $-0.0126 \pm 3.80 \times 10^{-4}$ | $0.0175 \pm 3.95 \times 10^{-4}$ | $0.0329 \pm 4.69 \times 10^{-4}$ | $0.0475 \pm 5.36 \times 10^{-4}$ | $0.0619 \pm 5.18 \times 10^{-4}$ |
| $\mathcal{D}_{pp}$ | $-0.00187 \pm 3.25 \times 10^{-4}$ | $0.00392 \pm 2.45 \times 10^{-4}$ | $0.00700 \pm 2.40 \times 10^{-4}$ | $0.00992 \pm 2.26 \times 10^{-4}$ | $0.01264 \pm 2.78 \times 10^{-4}$ |
| $\langle \delta p_{t1} \delta p_{t2} \rangle_{pp}$ | $0.00242 \pm 1.11 \times 10^{-4}$ | $0.00209 \pm 8.22 \times 10^{-5}$ | $0.00202 \pm 9.67 \times 10^{-5}$ | $0.00199 \pm 8.25 \times 10^{-5}$ | $0.00213 \pm 6.62 \times 10^{-5}$ |
| $N_{events}$ | 2481787 | 2569268 | 2578825 | 2580011 | 2573404 |

Table 7.1: The calculations are performed using charged particles from the kinematic area and an $|\eta| < 1$ at 11.5, 19.6, 27, 39 & 62.4 $GeV$. Uncertainties are expressed as standard deviation of subgroup values. (This data from G.Moschelli, gmoschell@ltu.edu)

Finally, we have $\mathcal{R}^{eq} = \mathcal{R}^0$ which is intended to come from PYTHIA, where we already know what it is, but it does not fit as we can see from the low to the high energy levels from the graphs above. Next, we have the $\mathcal{R}^{eq} = Const/(dN/dy)$, which is the one we believe is physically correct (according to reference [14]) and that PYTHIA is incorrect. The third $\mathcal{R}^{eq} = Const/(dN/dy)^{\alpha}$, which is simply the one we want to fit the data without physical meaning. But it is important to note that, because we used a lot of approximations, we do not expect our theory to fit everything perfectly; and, in fact it does not fit everything super-perfectly; but, at the very least, we can demonstrate the concept.

Last but not least, we seek to persuade the experimentalists that they should measure $\mathcal{D}$ in addition to measuring all correlations at the same time (simultaneously). It is our intention to utilize all of these observables together to confine our estimates of the survival probability $S$, with the hope of being able to answer the question: Can observables demonstrate that there is a phenomenon known as partial thermalization?

# CHAPTER 8 CONCLUSION

The main goal of this thesis, is after finding that the momentum-multiplicity fluctuations not zero, we demonstrate that the observables $\mathcal{R}$, $\mathcal{C}$, $\mathcal{D}$, and $\langle \delta p_{t1} \delta p_{t2} \rangle$, which are all two-particle correlation observables, are mathematically connected by equation (5.12). When these observables are observed or calculated at the same time using the same method, (5.12) can be used as a validation tool for theoretical models, depending on the circumstances. On the other hand we develop differential equations for studying the evolution of correlations and other characteristics of ion collisions by inserting Langevin noise into kinetic theory for investigating the non-equilibrium properties of correlation data.

This dissertation is structured as follows:

- In Chapter 2, we begin by introducing some of the concepts that will be discussed throughout the remainder of the course. Also with the help of the Glauber model that derived in this chapter, we were able to determine two important centrality variables: the number of binary collisions ($N_{coll}$) and the number of participants ($N_{part}$), which were calculated in relation to the impact parameter ($b$) of a collision in order to find the value of observables in local equilibrium from the blast wave model and compare them to the experimental data from STAR and ALICE.
- In Chapter 3, we address features of the Boltzmann equation and relaxation time approximation, both linearized and non-linearized, that are relevant to our study. The Boltzmann equation describes how the one-body phase space distribution $f$ relaxes to $f^e$, the local equilibrium distribution. In general, $f^e$ is governed by nonlinear constraints (3.22) that enforce conservation laws on energy, momentum, and conservation numbers. When these conditions are linearized, they are reduced to the requirement that the temperature $T$, velocity $\mathbf{v}$, and chemical potential $\mu$ in $f^e$ obey effective ideal hydrodynamic equations. (3.28) and (3.43).
- In Chapter 4, in order to understand non-equilibrium correlations, we use Langevin fluctuations in combination with the Boltzmann equation. The two body equation

(4.40) is derived using stochastic differential equation methods established in the area of viscous hydrodynamics. To impose the conservation principles laws, we use projection operators generated from linearized Boltzmann equation. The equation (4.40) and its formal solution can be used to describe small changes in the flow of a nonlinear average flow (3.28).

- In Chapter 5, we showed that the same parent correlation function is used to create two-particle multiplicity fluctuations ($\mathcal{R}$), transverse momentum correlations ($\mathcal{C}$), correlations of the transverse momentum fluctuations ($\langle \delta p_{t1} \delta p_{t2} \rangle$), and multiplicity-momentum correlations ($\mathcal{D}$) and these four observabels are mathematically linked together by equation (5.12).
- In Chapter 6, we showed that multiplicity fluctuations ($\mathcal{R}$), transverse momentum correlations ($\mathcal{C}$), correlations of the transverse momentum fluctuations ($\langle \delta p_{t1} \delta p_{t2} \rangle$), and multiplicity-momentum correlations ($\mathcal{D}$) and their relationship to PYTHIA/Angantyr simulated collision events at 200 $GeV$ and 2.76 $TeV$ have been estimated energy of collision. A novel observable, multiplicity-momentum correlations, is computed for the first time in this thesis.
- In Chapter 7, the purpose of this chapter is to design a methodology for determining the degree of thermalization by combining momentum-multiplicity correlation observables in kinetic theory. The Boltzmann equation in relaxation time approximation plus Langevin noise is used to investigate the influence of thermalization on these correlations. We propose a novel non-equilibrium transport equation (4.56) for the two-body distribution function that is compatible with the conservation principles that apply to microscopic scattering phenomena. We discover that these conservation constraints restrict the correlation observables' long-range behavior to behave differently depending on their degree of thermalization. We discover that transverse momentum fluctuations in peripheral lead-lead (Pb-Pb) collisions at the LHC and gold-gold (Au-Au) collisions at the RHIC deviates significantly from equilibrium. We suggest new measurements on this chapter that we believe will deliver more accurate information.

# REFERENCES

[1] S. Beolè. “Looking for Quark Gluon Plasma in Pb-Pb collisions at 158 GeV/c”. In: (Feb. 2022).

[2] “Chiral restoration at finite density and temperature”. In: *Nuclear Physics A* 504.4 (1989), pp. 668–684. ISSN: 0375-9474.

[3] A. Barducci et al. “Chiral-symmetry breaking in QCD at finite temperature and density”. In: *Physics Letters B* 231.4 (1989), pp. 463–470. ISSN: 0370-2693.

[4] J. D. Bjorken. “Highly relativistic nucleus-nucleus collisions: The central rapidity region”. In: *Phys. Rev. D* 27 (1 Jan. 1983), pp. 140–151.

[5] R. J. Glauber. “Lectures on Theoretical Physics”. In: Vol. I. (Inter-Science, New York,1959).

[6] I. Arsene et al. “Quark–gluon plasma and color glass condensate at RHIC? The perspective from the BRAHMS experiment”. In: *Nuclear Physics A* 757.1-2 (Aug. 2005), pp. 1–27.

[7] M. M. Aggarwal et al. “Scaling of particle and transverse energy production in Pb-208 + Pb-208 collisions at 158-A-GeV”. In: *Eur. Phys. J. C* 18 (2001), pp. 651–663. arXiv: `nucl-ex/0008004`.

[8] “Particle Data Group.” In: ().

[9] Björn Schenke, Prithwish Tribedy, and Raju Venugopalan. “Event-by-event gluon multiplicity, energy density, and eccentricities in ultrarelativistic heavy-ion collisions”. In: *Physical Review C* 86.3 (Sept. 2012).

[10] Chun Shen and Ulrich Heinz. *The road to precision: Extraction of the specific shear viscosity of the quark-gluon plasma.* 2015. arXiv: `1507.01558 [nucl-th]`.

[11] Ekkard Schnedermann, Josef Sollfrank, and Ulrich Heinz. “Thermal phenomenology of hadrons from$200 AGeV S+S$ collisions”. In: *Phys. Rev. C* 48 (5 Nov. 1993), pp. 2462–2475.

[12] Fabrice Retiere and Michael Annan Lisa. “Observable implications of geometrical and dynamical aspects of freeze-out in heavy ion collisions”. In: *Phys. Rev. C* 70 (4 Oct. 2004), p. 044907.

[13] Boris Tomasik. “Blast-wave snapshots from RHIC”. In: *arXiv e-prints*, nucl-th/0304079 (Apr. 2003), nucl–th/0304079. arXiv: `nucl-th/0304079 [nucl-th]`.

[14] Sean Gavin and George Moschelli. “Fluctuation probes of early-time correlations in nuclear collisions”. In: *Physical Review C* 85.1 (Jan. 2012).

[15] Fred Cooper and Graham Frye. “Comment on the Single Particle Distribution in the Hydrodynamic and Statistical Thermodynamic Models of Multiparticle Production”. In: *Phys. Rev. D* 10 (1974), p. 186.

[16] George Stevens. Moschelli. *”Two Particle Correlations And The Ridge In Relativistic Heavy Ion Collisions”*. https://digitalcommons.wayne.edu/oa$_{d}issertations/$23, 2010.

[17] Sergei A. Voloshin, Arthur M. Poskanzer, and Raimond Snellings. *Collective phenomena in non-central nuclear collisions.* 2008. arXiv: `0809.2949 [nucl-ex]`.

[18] Jean-Yves Ollitrault. “Anisotropy as a signature of transverse collective flow”. In: *Phys. Rev. D* 46 (1 July 1992), pp. 229–245.

[19] Wojciech Florkowski, Radoslaw Ryblewski, and Michael Strickland. “Anisotropic Hydrodynamics for Rapidly Expanding Systems”. In: *Nuclear Physics A* 916 (Apr. 2013).

[20] “Formation of dense partonic matter in relativistic nucleus–nucleus collisions at RHIC: Experimental evaluation by the PHENIX Collaboration”. In: *Nuclear Physics A* 757.1 (2005). First Three Years of Operation of RHIC, pp. 184–283. ISSN: 0375-9474.

[21] “Experimental and theoretical challenges in the search for the quark–gluon plasma: The STAR Collaboration’s critical assessment of the evidence from RHIC collisions”. In: *Nuclear Physics A* 757.1 (2005). First Three Years of Operation of RHIC, pp. 102–183. ISSN: 0375-9474.

[22] K. Aamodt et al. “Elliptic Flow of Charged Particles in Pb-Pb Collisions at $sNN = 2.76TeV$”. In: *Physical Review Letters* 105.25 (Dec. 2010).

[23] “Higher Harmonic Anisotropic Flow Measurements of Charged Particles in Pb-Pb Collisions at $\sqrt{s_{NN}} = 2.76$ TeV”. In: *Phys. Rev. Lett.* 107 (3 July 2011), p. 032301.

[24] Björn Schenke. “Flow in heavy-ion collisions theory perspective”. In: *Journal of Physics G: Nuclear and Particle Physics* 38.12 (Nov. 2011), p. 124009.

[25] A.K. Chaudhuri. “Nearly perfect fluid in Au+Au collisions at RHIC”. In: *Physics Letters B* 681.5 (2009), pp. 418–422. ISSN: 0370-2693.

[26] Raimond Snellings. “Elliptic flow: a brief review”. In: *New Journal of Physics* 13.5 (May 2011), p. 055008. ISSN: 1367-2630.

[27] “Bulk properties of the medium produced in relativistic heavy-ion collisions from the beam energy scan program”. In: *Phys. Rev. C* 96 (4 Oct. 2017), p. 044904.

[28] “Bulk properties of the system formed in Au+Au collisions at sNN=14.5 GeV at the BNL STAR detector”. In: *Physical Review C* 101.2 (Feb. 2020). ISSN: 2469-9993.

[29] “Systematic measurements of identified particle spectra in pp, d+Au, and Au+Au collisions at the STAR detector”. In: *Phys. Rev. C* 79 (3 Mar. 2009), p. 034909.

[30] “Identified Particle Distributions in *pp* and Au+Au Collisions at $\sqrt{s_{NN}} = 200$ GeV”. In: *Phys. Rev. Lett.* 92 (11 Mar. 2004), p. 112301.

[31] “Higher Harmonic Anisotropic Flow Measurements of Charged Particles in Pb-Pb Collisions atsNN=2.76 TeV”. In: *Physical Review Letters* 107.3 (July 2011).

[32] “Centrality determination of Pb-Pb collisions atsNN=2.76TeV with ALICE”. In: *Physical Review C* 88.4 (Oct. 2013). ISSN: 1089-490X.

[33] “Equilibration of the quark-gluon plasma produced in relativistic heavy ion collisions”. In: *Physics Letters B* 224.1 (1989), pp. 16–20. ISSN: 0370-2693.

[34] Sean Gavin. “Partial thermalization in ultrarelativistic heavy-ion collisions”. In: *Nuclear Physics B* 351.3 (1991), pp. 561–578. ISSN: 0550-3213.

[35] H. Heiselberg and Xin-Nian Wang. “Expansion, thermalization, and entropy production in high-energy nuclear collisions”. In: *Phys. Rev. C* 53 (4 Apr. 1996), pp. 1892–1902.

[36] Gouranga C. Nayak and V. Ravishankar. “Preequilibrium evolution of quark-gluon plasma”. In: *Phys. Rev. C* 58 (1 July 1998), pp. 356–364.

[37] Gouranga C. Nayak and V. Ravishankar. “Preequilibrium evolution of quark-gluon plasma”. In: *Physical Review C* 58.1 (July 1998), pp. 356–364. ISSN: 1089-490X. DOI: `10.1103/physrevc.58.356`.

[38] Yoshitaka Hatta, Mauricio Martinez, and Bo-Wen Xiao. “Analytic solutions of the relativistic Boltzmann equation”. In: *Phys. Rev. D* 91 (8 Apr. 2015), p. 085024.

[39] F. Reif. *Fundamentals of Statistical and Thermal Physics*. Waveland Press, 2009.

[40] Christopher David. Zin. *”Dynamic Fluctuations From Hydrodynamics And Kinetic Theory In High Energy Collisions”*. https://digitalcommons.wayne.edu/ oa$_{d}issertations$/1906, 2017.

[41] S. R. De Groot. *Relativistic Kinetic Theory. Principles and Applications*. Ed. by W. A. Van Leeuwen and C. G. Van Weert. 1980.

[42] Konstantinos Lazaridis, Logan Wickham, and Nikolaos Voulgarakis. “Fluctuating hydrodynamics for ionic liquids”. In: *Physics Letters A* 381.16 (2017), pp. 1431–1438. ISSN: 0375-9601.

[43] Ronald Fox. “Contributions to the Theory of Multiplicative Stochastic Processes”. In: *Journal of Mathematical Physics* 13 (Aug. 1972).

[44] Mordechai Bixon and Robert Zwanzig. “Boltzmann-Langevin Equation and Hydrodynamic Fluctuations”. In: *Phys. Rev.* 187 (1 Nov. 1969), pp. 267–272.

[45] Sean Gavin, George Moschelli, and Christopher Zin. "Boltzmann-Langevin approach to pre-equilibrium correlations in nuclear collisions". In: *Physical Review C* 95.6 (June 2017).

[46] N.G. Van Kampen. *Stochastic Processes in Physics and Chemistry.* North-Holland Personal Library. Elsevier Science, 2011. ISBN: 9780080475363.

[47] C.W. Gardiner. *Handbook of Stochastic Methods for Physics, Chemistry, and the Natural Sciences.* Springer complexity. Springer, 2004. ISBN: 9783540208822.

[48] Sean Gavin, George Moschelli, and Christopher Zin. "Rapidity correlation structure in nuclear collisions". In: *Phys. Rev. C* 94 (2 Aug. 2016), p. 024921.

[49] James W. Dufty, Mirim Lee, and J. Javier Brey. "Kinetic model for pair correlations". In: *Phys. Rev. E* 51 (1 Jan. 1995), pp. 297–309.

[50] "Longitudinal and azimuthal evolution of two-particle transverse momentum correlations in Pb–Pb collisions at sNN=2.76TeV". In: *Physics Letters B* 804 (2020), p. 135375. ISSN: 0370-2693.

[51] "Incident energy dependence of $p_t$ correlations at relativistic energies". In: *Phys.Rev.C* 72 (4 Oct. 2005), p. 044902.

[52] S. Voloshin and Y. Zhang. "Flow study in relativistic nuclear collisions by Fourier expansion of azimuthal particle distributions". In: *Zeitschrift fr Physik C Particles and Fields* 70.4 (May 1996), pp. 665–671. ISSN: 1431-5858.

[53] Nicolas Borghini, Phuong Mai Dinh, and Jean-Yves Ollitrault. "New method for measuring azimuthal distributions in nucleus-nucleus collisions". In: *Phys. Rev. C* 63 (5 Apr. 2001), p. 054906.

[54] Phuong Mai Dinh, Nicolas Borghini, and Jean-Yves Ollitrault. "Effects of HBT correlations on flow measurements". In: *Physics Letters B* 477.1-3 (Mar. 2000), pp. 51–58. ISSN: 0370-2693.

[55] Michael Annan Lisa et al. "FEMTOSCOPY IN RELATIVISTIC HEAVY ION COLLISIONS: Two Decades of Progress". In: *Annual Review of Nuclear and Particle Science* 55.1 (Dec. 2005), pp. 357–402. ISSN: 1545-4134.

[56] P. Danielewicz et al. “Collective motion in nucleus-nucleus collisions at 800 MeV/nucleon”. In: *Phys. Rev. C* 38 (1 July 1988), pp. 120–134.

[57] Nicolas Borghini. *Multiparticle correlations and momentum conservation in nucleus-nucleus collisions.* 2007. arXiv: `0707.0436 [nucl-th]`.

[58] Nicolas Borghini, Phuong Mai Dinh, and Jean-Yves Ollitrault. “Is the analysis of flow at the CERN Super Proton Synchrotron reliable?” In: *Physical Review C* 62.3 (Aug. 2000). ISSN: 1089-490X.

[59] Sean Gavin, Larry McLerran, and George Moschelli. “Long range correlations and the soft ridge in relativistic nuclear collisions”. In: *Physical Review C* 79.5 (May 2009). ISSN: 1089-490X.

[60] “Two-particle differential transverse momentum and number density correlations in $p-$Pb collisions at 5.02 TeV and Pb-Pb collisions at 2.76 TeV at the CERN Large Hadron Collider”. In: *Phys. Rev. C* 100 (4 Oct. 2019), p. 044903.

[61] “Evolution of the differential transverse momentum correlation function with centrality in Au+Au collisions at sNN=200 GeV”. In: *Physics Letters B* 704.5 (2011), pp. 467–473. ISSN: 0370-2693.

[62] “Flow Dominance and Factorization of Transverse Momentum Correlations in Pb-Pb Collisions at the LHC”. In: *Phys. Rev. Lett.* 118 (16 Apr. 2017), p. 162302.

[63] Niseem Magdy et al. “Azimuthal dependence of two-particle transverse momentum current correlations”. In: *The European Physical Journal C* 81.8 (Aug. 2021). ISSN: 1434-6052.

[64] Sean Gavin, Larry McLerran, and George Moschelli. “Long range correlations and the soft ridge in relativistic nuclear collisions”. In: *Phys. Rev. C* 79 (5 May 2009), p. 051902.

[65] H. Appelshäuser et al. “Event-by-event fluctuations of average transverse momentum in central Pb+Pb collisions at 158 GeV per nucleon”. In: *Physics Letters B* 459.4 (July 1999), pp. 679–686. ISSN: 0370-2693.

[66] T. Anticic et al. “Transverse momentum fluctuations in nuclear collisions at158AGeV”. In: *Physical Review C* 70.3 (Sept. 2004). ISSN: 1089-490X.

[67] “Event-wise $<p_t>$ fluctuations in Au-Au collisions at $\sqrt{s_{NN}} = 130$ GeV”. In: *Phys. Rev. C* 71 (6 June 2005), p. 064906.

[68] D. Adamová et al. “Event-by-event fluctuations of the mean transverse momentum in 40, 80, and 158 PbAu collisions”. In: *Nuclear Physics A* 727.1-2 (Nov. 2003), pp. 97–119. ISSN: 0375-9474.

[69] STAR Collaboration et al. “Transverse-momentumptcorrelations on (, phi) from mean-ptfluctuations in Au–Au collisions at GeV”. In: *Journal of Physics G: Nuclear and Particle Physics* 32.6 (May 2006), pp. L37–L48. ISSN: 1361-6471.

[70] “Event-by-event fluctuations in mean $p_T$ and mean $e_T$ in $\sqrt{s_{\mathrm{NN}}} = 130$GeV Au+Au collisions”. In: *Phys. Rev. C* 66 (2 Aug. 2002), p. 024901.

[71] “Measurement of Nonrandom Event-by-Event Fluctuations of Average Transverse Momentum in $\sqrt{s_{NN}} = 200$ GeV Au + Au and $p + p$ Collisions”. In: *Phys. Rev. Lett.* 93 (9 Aug. 2004), p. 092301.

[72] B. Abelev et al. “Event-by-event mean $p_{\mathbf{T}}$ pT fluctuations in pp and Pb–Pb collisions at the LHC”. In: *The European Physical Journal C* 74.10 (Oct. 2014). ISSN: 1434-6052.

[73] Stefan Heckel. “Event-by-event meanpTfluctuations in pp and Pb–Pb collisions at the LHC”. In: *EPJ Web of Conferences* 90 (2015). Ed. by F. Fabbri and P.Editors Giacomelli, p. 08006. ISSN: 2100-014X.

[74] “Collision-energy dependence of $p_t$ correlations in Au + Au collisions at energies available at the BNL Relativistic Heavy Ion Collider”. In: *Phys. Rev. C* 99 (4 Apr. 2019), p. 044918.

[75] H. Heiselberg and A. D. Jackson. “Anomalous multiplicity fluctuations from phase transitions in heavy-ion collisions”. In: *Phys. Rev. C* 63 (6 May 2001), p. 064904.

[76] M. Rybczynski, Z. Wlodarczyk, and G. Wilk. *Possible signal for critical point in hadronization process.* 2004. arXiv: `hep-ph/0305329 [hep-ph]`.

[77] M.J. Tannenbaum. “The distribution function of the event-by-event average pT for statistically independent emission”. In: *Physics Letters B* 498.1 (2001), pp. 29–34. ISSN: 0370-2693.

[78] Zhenyu Xu et al. In: 47.12 (Oct. 2020), p. 125102.

[79] Piotr Bozek, Wojciech Broniowski, and Sandeep Chatterjee. *Transverse Momentum Fluctuations and Correlations.* 2017. arXiv: `1707.04420 [nucl-th]`.

[80] B. I. Abelev et al. “Systematic measurements of identified particle spectra inpp,d+Au, andAu+Aucollisions at the STAR detector”. In: *Physical Review C* 79.3 (Mar. 2009). ISSN: 1089-490X.

[81] B. Abelev et al. “Multiplicity dependence of the average transverse momentum in pp, p–Pb, and Pb–Pb collisions at the LHC”. In: *Physics Letters B* 727.4-5 (Dec. 2013), pp. 371–380. ISSN: 0370-2693.

[82] Torbjörn Sjöstrand and Maria van Zijl. “A multiple-interaction model for the event structure in hadron collisions”. In: *Phys. Rev. D* 36 (7 Oct. 1987), pp. 2019–2041.

[83] Torbjörn Sjöstrand. *Colour reconnection and its effects on precise measurements at the LHC.* 2013. arXiv: `1310.8073 [hep-ph]`.

[84] S. Jeon and V. Koch. “Charged Particle Ratio Fluctuation as a Signal for Quark-Gluon Plasma”. In: *Phys. Rev. Lett.* 85 (10 Sept. 2000), pp. 2076–2079.

[85] Masayuki Asakawa, Ulrich Heinz, and Berndt Müller. “Fluctuation Probes of Quark Deconfinement”. In: *Phys. Rev. Lett.* 85 (10 Sept. 2000), pp. 2072–2075.

[86] V. Koch, M. Bleicher, and S. Jeon. “Event-by-event fluctuations and the QGP”. In: *Nuclear Physics A* 702.1 (2002). International Symposium on Statistical QCD, pp. 291–298. ISSN: 0375-9474.

[87] J. Adams et al. “Net charge fluctuations inAu+Aucollisions atsNN=130GeV”. In: *Physical Review C* 68.4 (Oct. 2003). ISSN: 1089-490X.

[88] Mingliang Zhou and Jiangyong Jia. “Centrality fluctuations in heavy-ion collisions”. In: *Phys. Rev. C* 98 (4 Oct. 2018), p. 044903.

[89] "Net Charge Fluctuations in Au + Au Interactions at $\sqrt{s_{NN}} = 130$ GeV". In: *Phys. Rev. Lett.* 89 (8 Aug. 2002), p. 082301.

[90] Jacek Zaranek. "Measures of charge fluctuations in nuclear collisions". In: *Phys. Rev. C* 66 (2 Aug. 2002), p. 024905.

[91] Stanisław Mrówczyński. "Hadronic matter compressibility from event-by-event analysis of heavy-ion collisions". In: *Physics Letters B* 430.1 (1998), pp. 9–14. ISSN: 0370-2693.

[92] A. Adare et al. "Charged hadron multiplicity fluctuations inAu+AuandCu+Cucollisions fromsNN=22.5to 200 GeV". In: *Physical Review C* 78.4 (Oct. 2008). ISSN: 1089-490X.

[93] Maitreyee Mukherjee. *Event-by-event multiplicity fluctuations in Pb-Pb collisions in ALICE.* 2016. arXiv: `1603.06824 [hep-ex]`.

[94] Francesco Becattini et al. "Multiplicity fluctuations in a hadron gas with exact conservation laws". In: *Phys. Rev. C* 72 (6 Dec. 2005), p. 064904.

[95] Sean Gavin and Claude Pruneau. "Covariance of antiproton yield and source size in nuclear collisions". In: *Phys. Rev. C* 61 (4 Mar. 2000), p. 044901.

[96] Sean Gavin and Joseph I. Kapusta. "Kaon and pion fluctuations from small disoriented chiral condensates". In: *Phys. Rev. C* 65 (5 May 2002), p. 054910.

[97] Stanisław Mrówczyński. "Measuring charge fluctuations in high-energy nuclear collisions". In: *Physical Review C* 66.2 (Aug. 2002). ISSN: 1089-490X.

[98] C. Pruneau, S. Gavin, and S. Voloshin. "Methods for the study of particle production fluctuations". In: *Physical Review C* 66.4 (Oct. 2002). ISSN: 1089-490X.

[99] J. Adams et al. "Minijet deformation and charge-independent angular correlations on momentum subspace(,)in Au-Au collisions atsNN=130GeV". In: *Physical Review C* 73.6 (June 2006). ISSN: 1089-490X.

[100] Jörn Putschke and the STAR Collaboration. "Intra-jet correlations of high-pt hadrons from STAR". In: *Journal of Physics G: Nuclear and Particle Physics* 34.8 (July 2007), S679–S683. ISSN: 1361-6471.

[101] A. Adare et al. "Dihadron azimuthal correlations in Au+Au collisions atsNN=200GeV". In: *Physical Review C* 78.1 (July 2008). ISSN: 1089-490X.

[102] Edward Wenger. "HighpTtriggered , correlations over a broad range in ". In: *Journal of Physics G: Nuclear and Particle Physics* 35.10 (Sept. 2008), p. 104080. ISSN: 1361-6471.

[103] Monika Sharma and Claude A. Pruneau. "Methods for the study of transverse momentum differential correlations". In: *Physical Review C* 79.2 (Feb. 2009).

[104] Shantam Ravan et al. "Correcting correlation function measurements". In: *Physical Review C* 89.2 (Feb. 2014).

[105] K. Aamodt et al. "Harmonic decomposition of two particle angular correlations in Pb–Pb collisions at ¡mml:math altimg="si1.gif" overflow="scroll"". In: *Physics Letters B* 708.3-5 (Feb. 2012), pp. 249–264.

[106] Sean Gavin and Mohamed Abdel-Aziz. "Measuring Shear Viscosity Using Transverse Momentum Correlations in Relativistic Nuclear Collisions". In: *Phys. Rev. Lett.* 97 (16 Oct. 2006), p. 162302.

[107] P.K. Kovtun, D.T. Son, and A. O. Starinets. "Viscosity in Strongly Interacting Quantum Field Theories from Black Hole Physics". In: *Physical Review Letters* 94.11 (Mar. 2005). ISSN: 1079-7114.

[108] Vıctor González. "Characterizing the medium created in PbPb collisions at SNN=2.76TeV by means of the evolution of two-particle transverse momentum correlations". In: *Journal of Physics: Conference Series* 1602.1 (July 2020), p. 012010.

[109] Victor Gonzalez et al. "Extraction of the specific shear viscosity of quark-gluon plasma from two-particle transverse momentum correlations". In: *The European Physical Journal C* 81.5 (May 2021). ISSN: 1434-6052.

[110] Victor Gonzalez et al. “Effect of centrality bin width corrections on two-particle number and transverse momentum differential correlation functions”. In: *Phys. Rev. C* 99 (3 Mar. 2019), p. 034907.

[111] George Moschelli and Sean Gavin. “Measuring the Rate of Isotropization of Quark-Gluon Plasma Using Rapidity Correlations”. In: *Nuclear Physics A* 982 (2019). The 27th International Conference on Ultrarelativistic Nucleus-Nucleus Collisions: Quark Matter 2018, pp. 311–314. ISSN: 0375-9474.

[112] George Moschelli and Sean Gavin. “Extracting the Shear Relaxation Time of Quark–Gluon Plasma from Rapidity Correlations”. In: *Acta Phys. Polon* 50 (2019), p. 1139.

[113] Sergei A. Voloshin. “Transverse radial expansion in nuclear collisions and two particle correlations”. In: *Physics Letters B* 632.4 (Jan. 2006), pp. 490–494. ISSN: 0370-2693.

[114] Adrian Dumitru et al. “Glasma flux tubes and the near side ridge phenomenon at RHIC”. In: *Nuclear Physics A* 810.1-4 (Sept. 2008), pp. 91–108. ISSN: 0375-9474.

[115] Torbjörn Sjöstrand et al. “An introduction to PYTHIA 8.2”. In: *Computer Physics Communications* 191 (2015), pp. 159–177. ISSN: 0010-4655.

[116] Christian Bierlich et al. “The Angantyr model for heavy-ion collisions in Pythia8”. In: *Journal of High Energy Physics* 2018.10 (Oct. 2018). ISSN: 1029-8479.

[117] Xiaofeng Luo et al. “Volume fluctuation and auto-correlation effects in the moment analysis of net-proton multiplicity distributions in heavy-ion collisions”. In: *Journal of Physics G: Nuclear and Particle Physics* 40.10 (Sept. 2013), p. 105104. ISSN: 1361-6471.

[118] S. Gavin. “Traces of Thermalization from $p_t$ Fluctuations in Nuclear Collisions”. In: *Phys. Rev. Lett.* 92 (16 Apr. 2004), p. 162301.

[119] J. Novak. “Energy dependence of fluctuation and correlation observables of transverse momentum in heavy-ion collisions”. In: ((2013)).

[120] George Moschelli and Sean Gavin. “Soft contribution to the hard ridge in relativistic nuclear collisions”. In: *Nuclear Physics A* 836.1–2 (May 2010), pp. 43–58. ISSN: 0375-9474. DOI: `10.1016/j.nuclphysa.2009.12.064`.

[121] Sean Gavin and George Moschelli. “Flow fluctuations from early-time correlations in nuclear collisions”. In: *Physical Review C* 86.3 (Sept. 2012). DOI: `10.1103/physrevc.86.034902`.

# ABSTRACT

## CORRELATIONS AND DYNAMIC FLUCTUATIONS IN HIGH ENERGY COLLISIONS

by

**ZOULFEKAR MAZLOUM**

**August 2022**

**Advisor:** Prof. Sean Gavin

**Major:** Physics

**Degree:** Doctor of Philosophy

Is thermalization necessary for hydrodynamic flow in nuclear collisions? The discovery of flow-like azimuthal correlations in pA and high-multiplicity pp collisions raises profound questions about the onset of collective flow and its relation to hydrodynamics. We seek independent experimental information on the degree of thermalization in order to identify those hydrodynamic collision systems in which flow is sensitive to equilibrium QCD properties. We aim to develop a protocol for identifying the degree of thermalization using a combination of momentum and multiplicity correlation. To study the effect of thermalization on these correlations, we use Boltzmann equation in the relaxation time approximation with Langevin noise. We derive a new non-equilibrium transport equation for the two-body distribution function that is consistent with the conservation laws obeyed by microscopic scattering processes. We find that transverse momentum fluctuations in peripheral Pb-Pb collisions at LHC markedly deviate from equilibrium behavior. We propose new measurements that can provide more refined information.

# AUTOBIOGRAPHICAL STATEMENT

**Name:**

Zoulfekar Mazloum.

**Education:**

Bachelor of Science in Physics, Lebanese University.

M.S., Ph.D. in Physics, Wayne State University; 2016-2022.

**Publications:**

Mary Cody, Sean Gavin, Brendan Koch, Mark Kocherovsky, Zoulfekar Mazloum, and George Moschelli *"Complementary Two−Particle Correlation Observables for Relativistic Nuclear Collision"* arXiv:2110.04884v1

**Additional Awards:**

Recipient Green Scholarship (2016)

Recipient of James Kaskas (2019)

Recipient Thomas C. Rumble Graduate Fellowship (2019)

**Professional Experience:**

Graduate Teaching and Research Assistant, Dept. of Physics and Astronomy, Wayne State University, 2016-2022.

**Biography:**

Zoulfekar Mazloum is a Ph.D. candidate at Wayne State University department of Physics and Astronomy. He was born and raised in Lebanon and received a bachelor's degree in Physics from Lebanese University. He loved to travel and always had goals to finish his highest academic degree. In 2015, Zoulfekar was blessed with an opportunity to come to the United States and start a new journey. He received a Masters degree in Physics from Wayne State University and was blessed to continue his path with fantastic people.